ASPECTS OF BEAM STABILITY AT THE LANSCE ACCELERATOR FACILITY

Tyler T. Fronk

Submitted to the faculty of the University Graduate School

in partial fulfillment of the requirement

for the degree

Master of Science

in the Department of Physics,

Indiana University

September, 2018

Accepted by the Graduate Faculty, Indiana University, in partial fulfillment of the requirement for the degree of Master of Science.

Dr. W. Michael Snow

Masters Committee

Dr. Chen-Yu Liu

Dr. Yuri K. Batygin

Dedicated to the memory of

Thomas Spickermann

Acknowledgments

Many individuals contributed on my path to completion of this thesis. First, I would like to thank my family for their support. I could not have done any of this without them. They have and will always be my foundation. I would also like to thank the many members of the team at LANSCE that contributed including the operations personnel who covered my shifts while at school and the accelerator operations physicist who were always willing to answer my questions. Without Yuri's patience and guidance I would not have been able to complete this work. I would like to thank Mark Gulley for always supporting my efforts and Thomas Spickermann for originally pushing me to attend USPAS. I would like to thank Susan Winchester from USPAS who was always willing to help and thank you to my USPAS class partner John Kuharik who suffered many long nights of homework with me. Thank you to my friend David LaBoon for all your encouragement. Finally, I would like to thank Michael Snow and the faculty at Indiana University that make this program possible without which I would not be able to achieve my professional goals.

Tyler T. Fronk

Aspects of Beam Stability at the LANSCE Accelerator Facility

The Los Alamos Neutron Science Center (LANSCE) is a multi-beam accelerator facility that has been in continuous operation for over 45 years. The accelerator serves 5 active user halls, each with divergent beam requirements. The LANSCE facility has long established the mission goal of maintaining at least 80% of scheduled beam delivery. An important component for meeting this goal is understanding the instabilities that cause beams to drop out of production status. This study highlights some of the most recent efforts to catalogue and sometimes mitigate these instabilities. Production run cycle beam reliability and availability statistics will be shown and analyzed by association with the major systems which induced the downtime. This study includes the evaluation RF accelerating field stabilities and effects on beam losses, magnet recovery and hysteresis problems, residual magnetic field effects from one beam-line on an adjacent line, and the effects of injector systems high voltage droop on the beam. Particle-in-cell simulation results for the side coupled linear accelerator portion of LANSCE will be shown, which includes results from a study of the contributing factors to emittance growth. Also, new transverse match solutions were found for the side-coupled cavity linear accelerator and compared to historical transverse match solutions.

Contents

Acceptance i

Acknowledgments iv

Abstract v

Introduction **1**

1 LANSCE Facility Overview **3**

1.1 The LANSCE Accelerator 3

1.1.1 Source Injection and Low Energy Transport 4

1.1.2 Drift Tube Linac 6

1.1.3 Transition Region and Isotope Production Facility 8

1.1.4 Side-Coupled Cavity Linear Accelerator 9

1.1.5 High Energy Beam Transport Lines 10

1.1.6 Proton Storage Ring 11

1.1.7 Proton Radiography and Ultra-Cold Neutron Facilities 12

1.2 Beam Structures 13

1.3 Beam Losses and Loss Detection 15

1.4 Accelerator Reliability 20

2 Injectors and Low Energy Beam Transport **25**

2.1 H^+ Source and LEBT Dynamics 25

2.2 H^- Source and LEBT Dynamics 26

2.3 High Voltage Droop Effect on H^- Beam Stability 27

3 Drift Tube Linear Accelerator Section **35**

3.1 Drift Tube Linear Accelerator (DTL) Beam Dynamics 35

3.2 Drift Tube Linac RF Stability 42

4 805 MHz Side Coupled Cavity Linear Accelerator **52**

4.1 Side-Coupled Cavity Linear (SCL) Accelerator Beam Dynamics 52

4.2 Paticle-In-Cell Simulations of the LANSCE SCL 59

4.3 Emittance Growth Studies Using BEAMPATH 64

4.4 SCL Transverse Match 71

4.5 805 MHz Side Coupled Linear Accelerator RF Stability 80

5 Accelerator Magnet Interventions **84**

5.1 Magnet Standardization 84

5.2 Residual Magnetic Field Effects on Adjacent WNR Beam Stability 88

Conclusions **99**

Appendix A Parametric Resonance in the DTL **102**

List of Tables

1.1 Summary of the H^- and H^+ beams produced at LANSCE 13

1.2 Guide for assigning causes for beam unavailability [12]. 21

1.3 LANSCE 2017 major contributions to beam downtime by system for the Lujan and WNR experimental areas. 22

3.1 Evolution of DTL set-points at the end of a production run cycle. 43

4.1 Transverse emittance growth due to integration step size 61

4.2 Measured normalized RMS emittance growth in the LANSCE linear accelerator. . . 64

4.3 Transverse normalized 4 RMS emittance growth due to varying initial longitudinal bunch length simulation results. 66

4.4 Space charge induced transverse normalized 4 RMS emittance growth simulation results. 68

4.5 Space charge induced longitudinal normalized 4 RMS emittance growth simulation results. 68

4.6 Varying accelerating fields induced transverse normalized 4 RMS emittance growth simulation results. 70

4.7 Varying accelerating fields induced longitudinal normalized 4 RMS emittance growth simulation results. 70

4.8 Varying accelerating fields induced momentum spread growth simulation results. . . 71

4.9 Historical matching parameters for the LANSCE SCL entry. 74

4.10 MADx simulation results for Twiss parameters at the entrance to the LANSCE SCL. 74

4.11 MADx calculated matched beam parameters at the entrance of Module 13. 75

4.12 MADx calculated matched beam parameters at the entrance of module 23. 77

4.13 LANSCE SCL quadrupole solution currents. 79

5.1 RIBM01 residual magnetic field Hall probe measurements. 92

List of Figures

1 An overview of the Los Alamos Neutron Science Center and its experimental areas. . 2

1.1 The LANSCE Accelerator complex including experimental flight paths. 4

1.2 Top view of the H^+ and H^- low energy beam transport lines. 5

1.3 Example of the slit and collector emittance gear used in the LEBT. 5

1.4 The LANSCE drift tube linear accelerator. 6

1.5 The new LANSCE 201RF MHz Diacrode FPA for DTL Modules 2-4. 7

1.6 The LANSCE 201RF MHz triode FPA for DTL Module 1. 7

1.7 Transition region of the LANSCE accelerator facility [2]. 8

1.8 LANSCE side coupled linear accelerator. 9

1.9 LANSCE SCL Module Layout. 9

1.10 LANSCE SCL klystron. 10

1.11 The LANSCE proton storage ring used for accumulation of proton pulses prior to delivery to the spallation neutron targets. 11

1.12 LANSCE PSR tune operating point [11]. 12

1.13 LANSCE proton radiography facility layout [7]. 12

1.14 LANSCE slow-wave chopper [1]. 13

1.15 LANSCE beam structures for the Lujan and WNR experimental areas [1]. 14

1.16 pRAD experimental area beam structure. 15

1.17 UCN experimental area beam structure. 15

1.18 LANSCE high energy beam losses. 16

1.19 Average vacuum throughout the LANSCE accelerator facility recorded from ion gauge readings at the end of the 2017 production run cycle. 16

1.20 LANSCE activation protection (AP) and loss monitor (LM) scintillation detectors. . 17

1.21 LANSCE ion chamber (IR) and gamma detector (GD) beam loss devices. 18
1.22 Calibration response of 05AP01 and its corresponding logarithmic line fit. 19
1.23 LANSCE beam reliability by experimental area for the past 10 years. 22
1.24 Average beam downtime by system for the 2017 Lujan Experimental Area production run cycle. 23
1.25 LANSCE beam downtime contributions by system for the past 10 years for the Lujan experimental area. 24

2.1 Example of horizontal measured at the output of the H^+ Injector prior to H_2^+ beam removal. 25
2.2 LANSCE H^+ LEBT beam profiles. 26
2.3 Example of horizontal emittance measured at the output of the H^- Injector. 27
2.4 LANSCE H^- LEBT beam profiles. 27
2.5 Correlation of H^- high voltage droop and linac sum beam losses. 28
2.6 80-kV Droop measured across the H^- macro pulse. 29
2.7 80-kV Droop measured across the H^- macro pulse with H^- Repeller set to 3.14 V. . . 29
2.8 Location of the horizontal Harp used for the high voltage droop study. 30
2.9 TRACE simulated envelopes and beam displacement with $\frac{dp}{p} = 0.1\%$. 31
2.10 Results from the H^- high voltage droop study. 31
2.11 Measurement of the horizontal displacement across the H^- macro pulse with 1800V of droop. 32
2.12 Droop across the beam pulse from the 670-kV Cockcroft-Walton Generator where 100 mV is equal to 50 V of droop. 32
2.13 Horizontal displacement measured across the H^+ beam pulse. 33

3.1 Transit time factors of the LANSCE DTL. 36
3.2 Accelerating Fields of the LANSCE DTL. 36
3.3 Half-maximum of separatrix in momentum of LANSCE DTL. 37
3.4 Phase advance of longitudinal oscillations per focusing period of LANSCE DTL. . . 38
3.5 Normalized longitudinal acceptance of LANSCE DTL. 38
3.6 LANSCE DTL FODO structure. 39
3.7 Phase advance of transverse oscillations in the LANSCE DTL focusing structure. . . 40

3.8 Phase advance of transverse oscillations of synchronous particle at the focusing period of the LANSCE DTL. 40
3.9 Transverse normalized acceptance of the LANSCE DTL. 41
3.10 Normalized maximum and minimum beta functions of the the LANSCE DTL. . . . 42
3.11 DTL phase scan theory and measurement example [24]. 43
3.12 Measured beam spill in the LANSCE switchyard as a function of DTL cavity field error [17]. 44
3.13 Example of instabilities in Module 2 amplitude cavity field during production beam operations. 45
3.14 Example of switchyard sum beam losses due to instabilities in the DTL RF cavity fields. 45
3.15 Instantaneous change in DTL module 3 cavity field amplitude and phase. 46
3.16 Coupling between DTL module 3's LLRF system and Module 4's cavity field phase. 46
3.17 Shift of IPF rastered beam due to instantaneous change in module 3's cavity field. . 47
3.18 Module 3 RF step-change event and digital LLRF system response [18]. 48
3.19 DTL digital LLRF system set-up and possible location of signal disturbances [18]. . 49
3.20 Module 3 cavity field maintained with the slow drift of the RF reference phase [18]. . 49
3.21 RF reference phase behavior during module 3 step-change event [18]. 50
3.22 Module 4 cavity field change during a sudden change in the reference phase drift [18]. 50
3.23 DTL cavity fields after repairs to the RF reference source. 51

4.1 Profile of energy gained in the LANSCE SCL. 53
4.2 The LANSCE side-coupled cavity linac FDO focusing structure [16]. 54
4.3 Transverse phase advance calculation comparison. 56
4.4 LANSCE SCL phase advances per focusing period. 56
4.5 Comparison of the effective phase advance in an RF field calculations. 57
4.6 LANSCE SCL normalized Twiss beta functions. 58
4.7 LANSCE SCL normalized transverse acceptance. 58
4.8 LANSCE SCL longitudinal acceptance 59
4.9 SCL BEAMPATH simulation set-up for Module 5. 60
4.10 Accelerating Fields of the LANSCE SCL used in BEAMPATH simulations. 60
4.11 LANSCE SCL LBEG beam envelopes from BEAMPATH simulations. 61
4.12 Example of LANSCE SCL beam envelopes from TRACE code. 62

4.13 Initial transverse space charge field for MPEG and LBEG beams. 62
4.14 Initial longitudinal space charge field for MPEG and LBEG beams. 63
4.15 Effective phase advance in an RF field for different beam currents. 63
4.16 LBEG Longitudinal phase width measured at the entrance to the LANSCE SCL. . . 65
4.17 Transverse normalized 4 RMS emittance growth with different initial longitudinal bunch lengths. 65
4.18 Transverse and longitudinal normalized 4 RMS emittance growth due to space charge force. 67
4.19 Transverse and longitudinal normalized 4 RMS emittance growth due to varying accelerating fields. 69
4.20 Energy spread due to varying accelerating fields. 71
4.21 Reduction in beam losses due to the SCL quadrupole magnet settings. 72
4.22 SCL Quadrupole magnet settings before and after the reduction in beam losses. . . . 72
4.23 Simulation set-up for entry into the LANSCE SCL. 73
4.24 Example of MADx matching of the beam at the point of slit position of TREM02, providing periodic beam envelopes. 73
4.25 TRACE 2D Module 5-7 match results with the MADx calculated Twiss parameters for G=2.0717(kG/cm) and constant ramp. 74
4.26 SCL Module 13 matching simulation set-up. 75
4.27 TRACE 2D simulation results from module 13 until module 48 with MADx calculated Twiss parameters at the entrance of module 13. 76
4.28 SCL Module 23 matching simulation set-up. 76
4.29 TRACE 2D simulation results from module 23 until module 48 with MADx calculated Twiss parameters at the entrance of module 23. 77
4.30 Beam envelopes for different quadrupole solutions in the LANSCE SCL. 78
4.31 Comparison of the empirical SCL quadrupole tune with the theoretical ramping match. 80
4.32 Drift of the SCL Module 11 phase set-point over several days of operation. 81
4.33 Example of effects of momentum spread at the output of the LANSCE accelerator from improper tuning. 81
4.34 Beam spill normalized by 1% variation in RF amplitude [23]. 82
4.35 Beam spill normalized by 1°variation in RF phase [23]. 83

5.1 Example of magnetic hysteresis loop in Ring Injection bending magnet. 84
5.2 Magnet standardization by cycling the magnet current around a set-point [19]. . . . 85
5.3 RIBM03 magnetic field stabilization measurement. 86
5.4 Magnet standardization procedure consisting of cycling the magnet current around the set-point. 86
5.5 BPM measurement results from developing a magnet standardization procedure. . . 87
5.6 Beam losses during the hysteresis recovery of LDMP02. a) Losses prior to turning LDMP02 off. b) Losses with no hysteresis recovery c) Losses after the hysteresis recovery of LDMP02. d) Losses after raising LDMP02 set-point 0.1 %. 88
5.7 Location of residual magnetic field effect on adjacent beam lines study. 89
5.8 Beam spill in the WNR beam line due to RIBM01 residual magnetic field. 90
5.9 BPM data in the WNR beam line due to RIBM01 residual magnetic field. 91
5.10 Measurement locations for the RIBM01 residual magnetic field 91
5.11 Beam losses after correcting for RIBM01 residual magnetic field with LDHM/VM09 steering magnets. 93
5.12 CST module of RIBM01 with adjacent WNR beam pipe [20]. 94
5.13 RIBM01 magnetic field along the beam line axis [20]. 94
5.14 RIBM01 residual magnetic field strengths at the WNR beam line axis [20]. 95
5.15 Magnetic field lines from the RIBM01 residual magnetic field near the WNR beam line Mu-metal shielding [20]. 95
5.16 RIBM01 CST model with Mu metal shielding extended on the WNR beam line [20]. 96
5.17 Magnetic field strength along the WNR beam line axis with full Mu-metal shiedling [20]. 96
5.18 Mu-metal shielding installed along the entire length of WNR beam pipe effecting by the RIBM01 residual magnetic field. 97
5.19 BPM results after Mu-metal shielding installed on the WNR beam line. 97

A.1 Parametric resonance in an RF field study of the LANSCE DTL. 103
A.2 Parametric resonance study of the LANSCE DTL tank 1 near the second region of instability. 103

Introduction

The Los Alamos Neutron Science Center (LANSCE) provided its first 800 MeV protons in 1975. Since that time, it has gone through many changes to its mission. It was originally commissioned as one of the first high power proton accelerators with a designed beam power of 1 MW. When particle physics moved beyond this energy regime the accelerator shifted its focus to the neutron sciences. The proton storage ring (PSR) was added in 1985. With its addition and the already existing weapons neutron research (WNR) target, the LANSCE facility became unique in its ability to provide a neutron flux over a large energy spectrum. In more recent years an ultra-cold neutron target (UCN) was added to expanded that energy regime to neutrons with kinetic energy less than 340 neV. Along with its neutron producing capabilities, LANSCE also has an isotope production target (IPF) that provides the vital medical isotopes and a proton radiography (pRAD) facility that has the ability to image dynamic processes using a tailored proton beam pulse. In all LANSCE provides five unique beams. In its current set-up four beams can be delivered simultaneously.

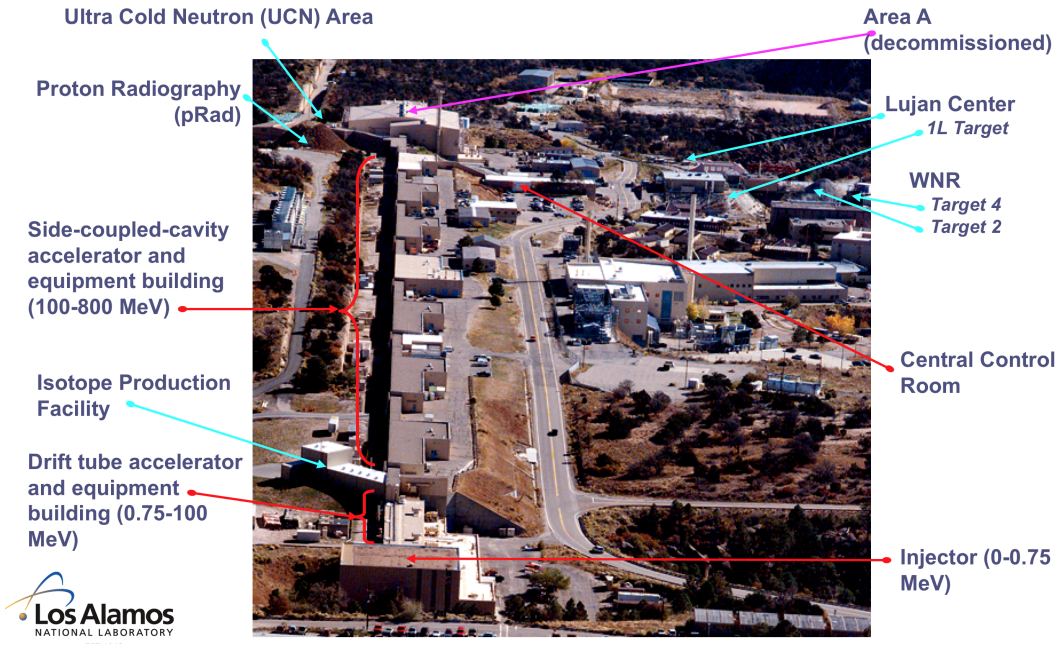

Figure 1: An overview of the Los Alamos Neutron Science Center and its experimental areas.

In a normal calendar year, the accelerator facility will be in a production mode for 6-8 months and in maintenance the rest of the year. A normal machine start-up to production and initial physics tune takes approximately 30 days. The facility has a goal of delivering beam at 80% reliability. Production downtime is logged for each experimental area and the causes of downtime are categorized by systems (High Power RF, Magnet Power Supply, Injectors, etc.).

The calendar year 2017 production time brought significant challenges to the LANSCE facility. Problems with source stability and failing linac tuning tools drastically extended the usual time required for the accelerator tune. In response, an effort was made to understand the contributing factors of tune stability and recovery. Also, due to the age of the facility, an effort was made to verify each of the facilities beam transport and tuning procedures. Beam development time was scheduled between production periods to examine beam stability by components and allocated with this priority in mind. Additional effort was made to discover original design reports for each relevant system so it would be possible to calculate and compare the beam dynamic parameters independently. These parameters were used to verify against new beam simulations used to study accelerator stability issues. This work supported by US DOE under contract DE-AC52-06NA25396 (LA-UR-18-27052).

Chapter 1

LANSCE Facility Overview

1.1 The LANSCE Accelerator

The LANSCE accelerator is a pulsed normal conducting machine that operates at 120 Hz repetition rate. It has both H^- and H^+ sources The H^- source provides beams for the PSR, WNR, UCN, and pRAD experimental areas, while the H^+ source provides the beam for the IPF target. IPF beam is accelerated to 100 MeV while all the H^- beams are accelerated to full designed 800 MeV. The facility still has the capability of accelerating H^+ beam to the machines full designed energy if a mission need for that capability should come. Figure 1.1 illustrates the layout of the LANSCE accelerator, including experimental flight paths.

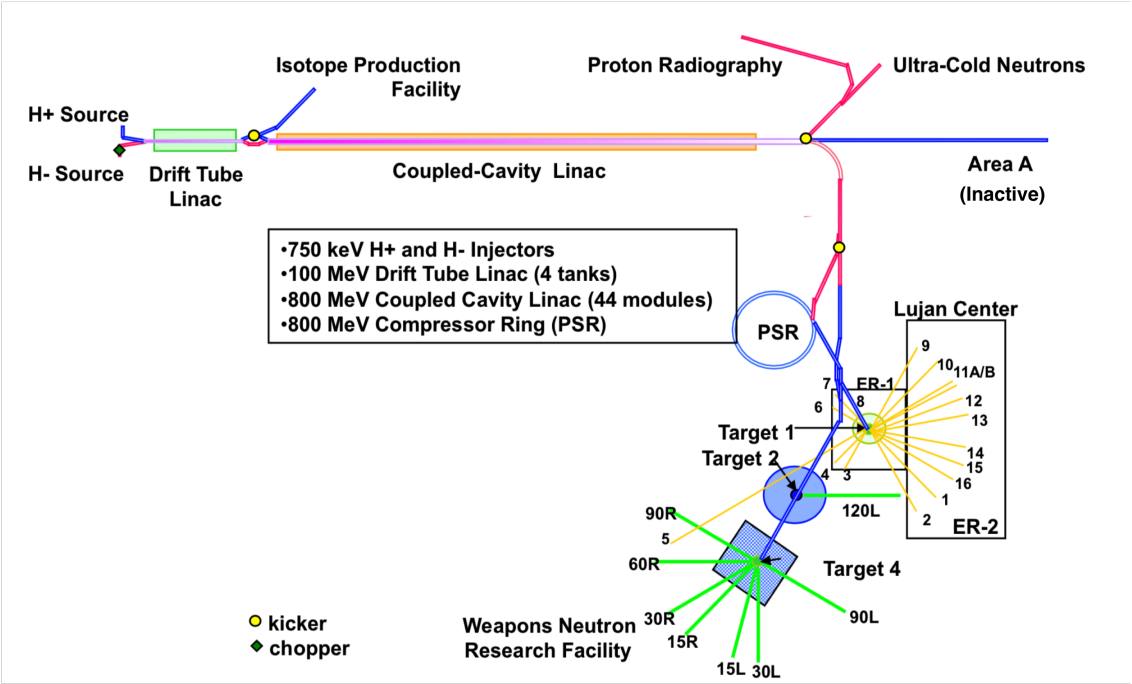

Figure 1.1: The LANSCE Accelerator complex including experimental flight paths.

1.1.1 Source Injection and Low Energy Transport

H^- and H^+ beams are produced by their respective ion source systems and then accelerated to 750 keV by Cockcroft-Walton generators. Figure 1.2 shows the LANSCE low-energy transport (LEBT) region after beam injection of both beam species. The H^- LEBT is designed to establish the multiple H^- beam structures used at LANSCE. It consists of an electrostatic chopper followed by a series of RF bunching systems. The low frequency buncher, which operates at 16.77 MHz, is used exclusively for the WNR beam while the H^- prebuncher which operates at 201.25 MHz is used for all H^- beams. The H^- LEBT consists of 18 quadrupoles, one 81° bending magnet, and 14 steering magnets.

The H^+ LEBT consists of 18 quadrupoles, one 81° bending magnet, and 10 steering magnets. The low energy beam transport line for H^+ also includes a beam prebuncher. The H^+ prebuncher operates at the same 201.25 MHz of the drift tube linac accelerating structure.

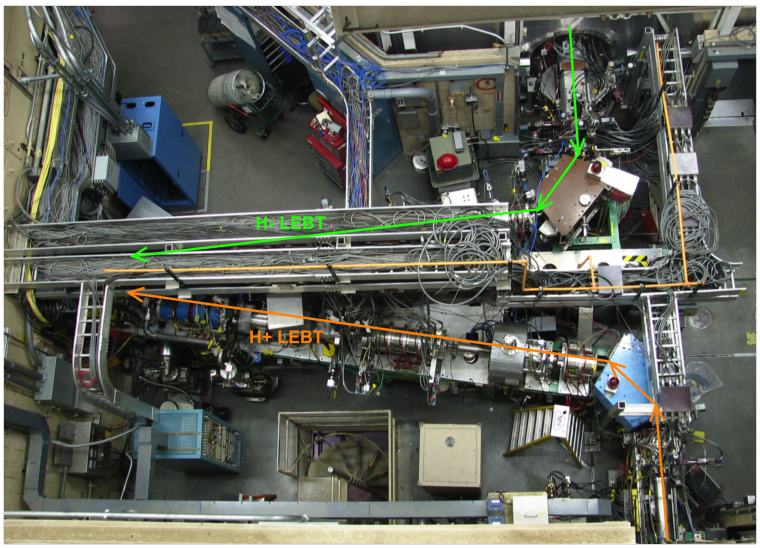

Figure 1.2: Top view of the H^+ and H^- low energy beam transport lines.

Both the H^+ and H^- low energy beam transport lines contain several diagnostic devices for measuring and setting beam parameters. LANSCE uses slit and collector type emittance gear (seen in fig. 1.3) for establishing matched conditions and setting Twiss parameters at critical points in the LEBT. Both LEBT's contain ground level deflectors, which are used in coordination with the machine fast protect system to interrupt beam if a downstream condition is out of specification.

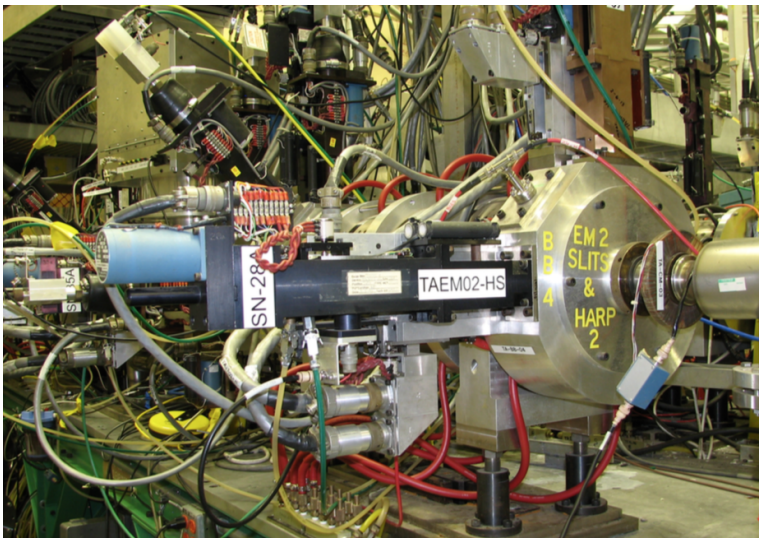

Figure 1.3: Example of the slit and collector emittance gear used in the LEBT.

1.1.2 Drift Tube Linac

At the end of the H^- and H^+ LEBT's, the beam lines are joined at the 9° bending magnet. All beams pass through the main buncher, where the final bunching before acceleration is provided. Also, the combined line consists of a final set of quadrupoles for establishing matched H^+ and H^- beams at the entrance to the Drift Tube Linac (DTL).

The Drift Tube Linear Accelerator portion of LANSCE raises beam energy from 0.75 to 100 MeV. The Alvarez style DTL consists of 4 tanks, which operate at 201.25 MHz and has inter-tank spacing to allow for beam diagnostics.

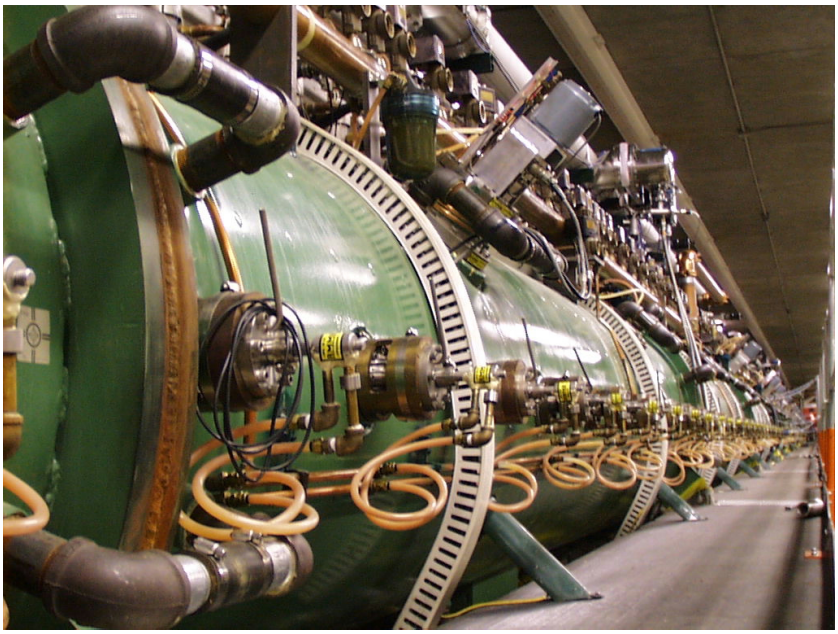

Figure 1.4: The LANSCE drift tube linear accelerator.

Tank 1's final power amplifier uses a Burle 7835V4 triode and has an analog low-level RF system. Tanks 2 through 4 have upgraded final power amplifiers that use Thales TH628 Diacrodes and a digital LLRF system [3] [4] (shown in fig. 1.5 and 1.6).

Figure 1.5: The new LANSCE 201RF MHz Diacrode FPA for DTL Modules 2-4.

Figure 1.6: The LANSCE 201RF MHz triode FPA for DTL Module 1.

1.1.3 Transition Region and Isotope Production Facility

After the DTL sections, 100-MeV beam enters into the transition region (TR), as seen in fig. 1.7. The two beam species are separated into the double chicanes of the transition region. The H^+ beam is kicked out of the TR region and enters the Isotope Production beam line, while the H^- beams will continue into the side-coupled cavity linear (SCL) accelerator. The eight TR bending magnets are powered by two different power supplies. The first magnet power supply provides current to all the bending magnets while the second power supply adds or subtracts from four of the bending magnets in the H^- beam path. In fig. 1.7, BM-05 and BM-08 have current subtracted from them while BM-06 and BM-07 have current added to them [2]. This scheme allows for the H^- beam to travel a longer path length ensuring that the H^- beam is at the correct synchronous phase for acceleration by the 805 MHz side-coupled cavity linear accelerator.

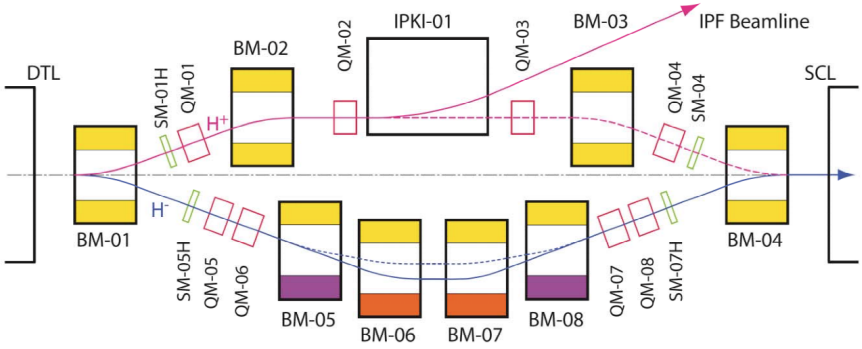

Figure 1.7: Transition region of the LANSCE accelerator facility [2].

The Isotope Production Facility was added to LANSCE in the early 2000's as a facility that can provide radioisotopes to scientist in the medical, nuclear physics, national security, and industrial applications [5]. The IPF beam line is a medium energy transport line from the DTL accelerator to the main isotope production target stack. The IPF line has specialize raster functions for a variety of possible dispersion patterns on the sensitive target. These raster designs spread the heat load on the target stack, allowing for higher beam current and more even irradiation of the targets. The IPF raster system has the ability to provide a 1,3, or 5 ring raster pattern depending on the irradiation requirements. This ability was added to the IPF beam line for the 2017 IPF accelerator improvement project [6].

1.1.4 Side-Coupled Cavity Linear Accelerator

The LANSCE side-coupled cavity linear accelerator consists of 44 accelerating modules (labelled Modules 5-48). A 100-MeV beam is injected into the SCL and accelerated to a final energy of 800 MeV.

Figure 1.8: LANSCE side coupled linear accelerator.

As shown in fig. 1.9, modules 5-12 consist of 4 accelerating tanks per module, each separated by a FDO lattice. Modules 13-48 consist of two accelerating tanks per module and are also separated by a FDO lattice, but have a different period from the other four-tank modules. There are a total of 104 accelerating tanks in the SCL. Each tank of the modules accelerates at a constant beta.

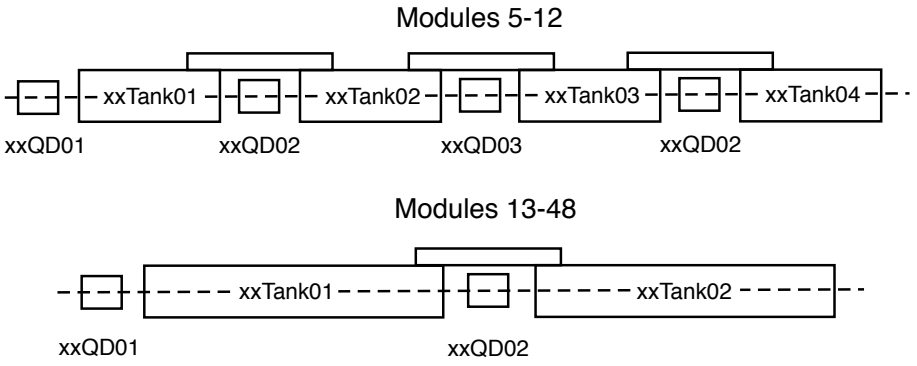

Figure 1.9: LANSCE SCL Module Layout.

Each SCL module is provided RF power from a klystron, having a maximum design output power of 1.25 MW. The klystrons operate at 120 Hz with a pulse width of 1000 μs. The phase and amplitude of the SCL tanks are controlled by an analog LLRF system. Current testing is being done to convert the SCL analog LLRF system to digital LLRF controls.

Figure 1.10: LANSCE SCL klystron.

1.1.5 High Energy Beam Transport Lines

After the SCL, the high energy beam pulses are split and transported into their respective experimental areas. This region is called the switchyard. A single bending magnet is used to separate H^+ and H^- from their common beamline used during acceleration. The H^+ beam is transported straight forward from the accelerator to the now decommissioned Area A. The H^- beam species is shared to the north and south of the center line. The dipole configuration in the switchyard gradually steers the beam to the south of the accelerator exit. This large 89° bend was designed to minimize Lorentz stripping of the H^- beam. After the bend, the beam is delivered to the proton storage ring, which accumulates proton pulses to be delivered to the moderated spallation neutron source at the Lujan

Center. Beam can either be delivered directly to the weapons neutron research facility's tungsten spallation neutron source or be accumulated first in the PSR. The switchyard kicker magnet system is used to divert a portion of the H^- beam to the Proton Radiography and Ultra-Cold Neutron experimental areas north of the central line.

1.1.6 Proton Storage Ring

The LANSCE proton storage ring (PSR) was completed in 1986. The ring accumulates proton pulses at a repetition rate of 20 Hz, which can then be extracted to the spallation neutron targets. Normally the PSR is aligned to deliver the accumulated proton pulse to the moderated spallation neutron target at the Lujan facility, but the capability exists to send the accumulated proton pulses to the unmoderated WNR target. The PSR is 90.2 meters in circumference that operates at a revolution frequency of 2.8 MHz. The bunch length of the beam is 290 $nsec$. With the accumulation time of 625 μsec, the beam circulates the ring approximately 1750 turns before extraction [10]. The average beam current in the PSR is 100 μA.

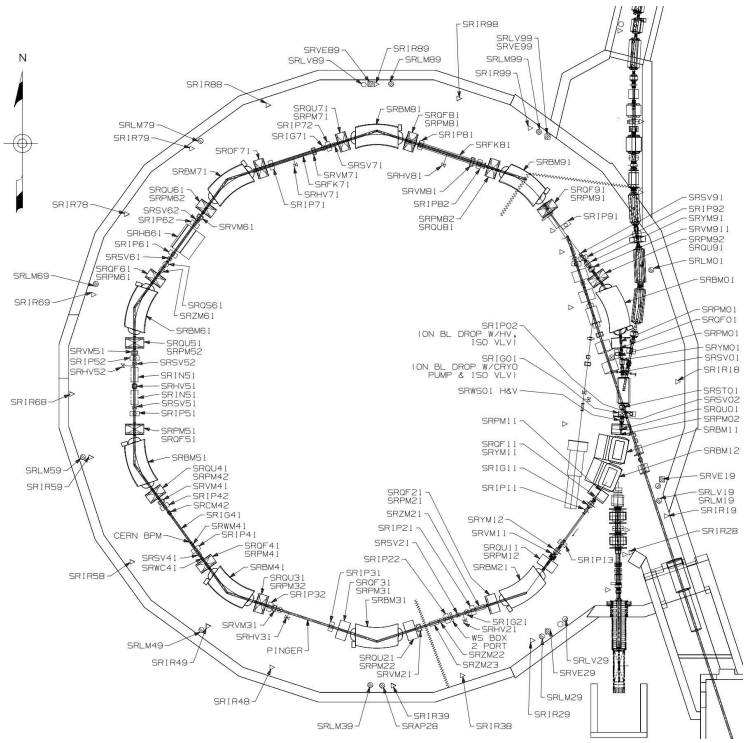

Figure 1.11: The LANSCE proton storage ring used for accumulation of proton pulses prior to delivery to the spallation neutron targets.

The PSR diagnostics consist of beam position monitors (BPM) located inside the quadrupoles

of the FODO lattice. The BPM's are used to determine the closed orbit and the fractional tune of the PSR. The PSR operating point for the tune is show in Figure 1.12 [11]. The PSR tune values are $Q_x = 3.19$ and $Q_y = 2.19$.

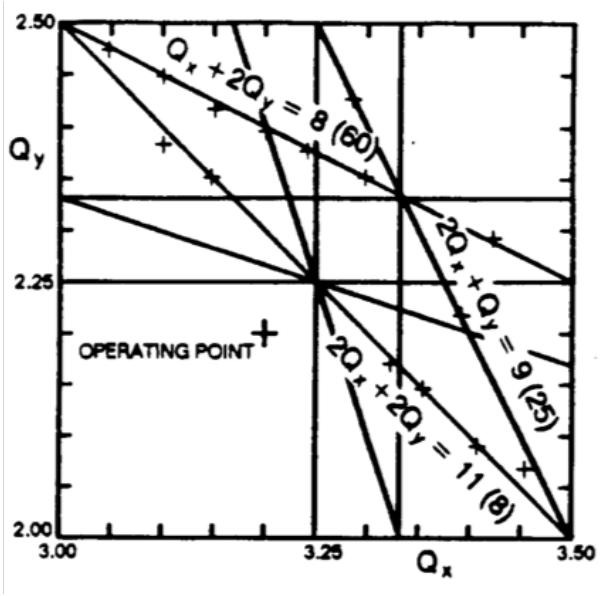

Figure 1.12: LANSCE PSR tune operating point [11].

1.1.7 Proton Radiography and Ultra-Cold Neutron Facilities

The Proton Radiography (fig. 1.13) and Ultra-Cold Neutron experimental areas share a common beam line from the LANSCE switchyard. H^- beam is kicked using two pulsed kicker magnets into the common line. Due to sharing this common line, experiments cannot be run simultaneously in the pRAD and UCN experimental areas.

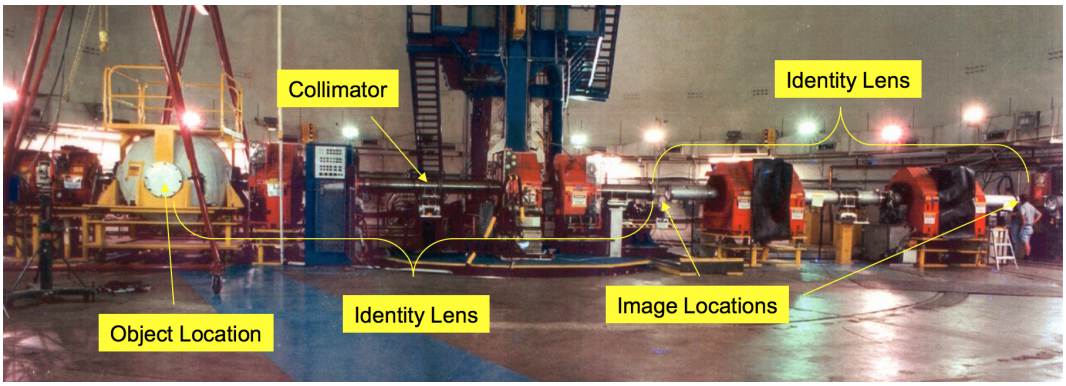

Figure 1.13: LANSCE proton radiography facility layout [7].

1.2 Beam Structures

LANSCE is unique in that it can produce and accelerate 4 distinctly structured H^- beams, 3 of which it can produce and accelerate simultaneously. It also produces a single H^+ beam that is used for the Isotope Production Facility. A summary of all 5 beams produced at LANSCE is shown in Table 1.1.

Table 1.1: Summary of the H^- and H^+ beams produced at LANSCE

Experimental Area	Repetition Rate (Hz)	Pulse Length (μs)	Current per Bunch (mA)	Average Current (μA)	Average Power (kW)
Lujan Center	20	625	10	100	80
IPF	100	625	4	230	23
WNR	100	625	25	4.0-5.0	3.2-4.0
UCN	20	625	10	10	8
pRAD	1	625	10	<1	<1

The four H^- beams structures are produced in the H^- low energy beam transport by a combination of a slow-wave chopper and RF bunching systems. The H^- chopper is 1 m long and has a rise time of approximately 7 ns. Chopper plate voltage is $\pm$ 650 V.

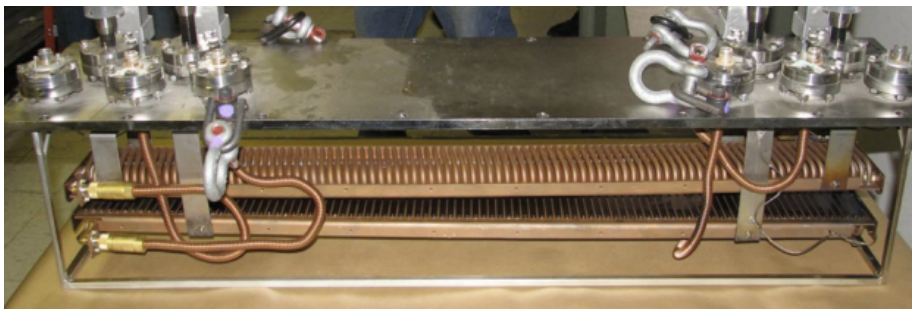

Figure 1.14: LANSCE slow-wave chopper [1].

The long pulse beam (see fig. 1.15) is produced for injection into the proton storage ring, which is extracted to the moderated spallation neutron source at the Lujan Center for Neutron Science. The PSR beam pulse is 290 ns wide, with a gap of 70 ns. This accounts for the entire 360-ns revolution time of the proton storage ring. The 70-ns gap allows for extraction and injection of the beam.

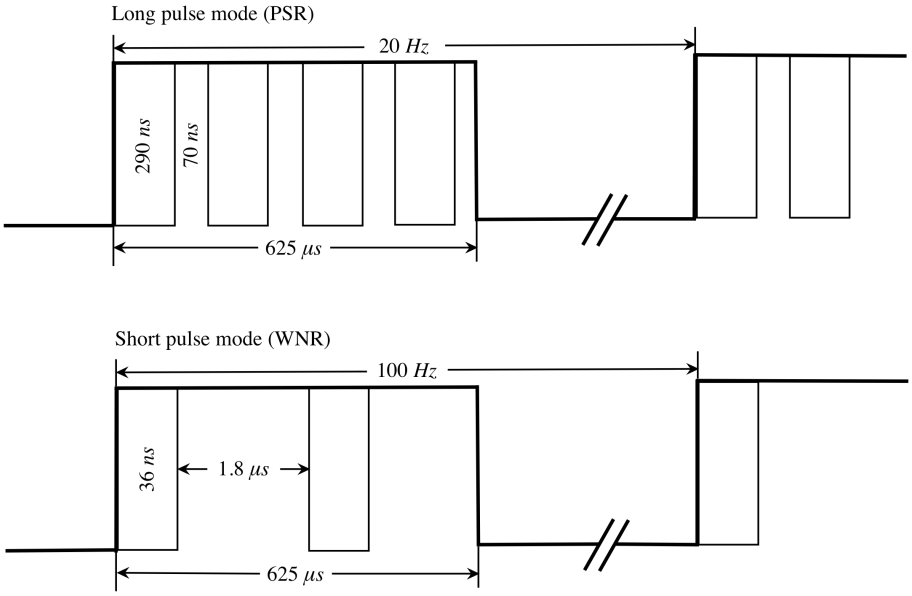

Figure 1.15: LANSCE beam structures for the Lujan and WNR experimental areas [1].

.

The short pulse beam (see fig. 1.15) is structured for delivery to the weapons neutron research facility's unmoderated spallation neutron source. WNR beam is a sequence of short single bunches separated by long time distances. The WNR beam alone utilizes the low-frequency buncher in the H^- LEBT. The purpose of the low-frequency buncher is to collect a single charge pulse equivalent to two to three times a regular 5-ns beam bunches accelerated in the 201.25 MHz linac. While the average current delivered to the WNR target is smaller (3.5 μA compared to 100 μA) than that of the PSR beam, it is more susceptible to space-charge effects, due to the higher charge per pulse.

The H^- beam for the pRAD and UCN experimental areas is uniquely structured to meet their experimental needs. Both utilize the H^- chopper to structure the beams accordingly. A typical pRAD structure will consist of a triggering pulse followed closely by several pulses for radiographing. UCN beam is structured so that they receive several seconds of pulse bursts, followed by a many second wait period to allow for the ultra-cold neutrons to traverse their experimental set-up. The structure of the pRAD wave form generated by the H^- chopper pattern generator is shown in fig. 1.16 and the structure of the UCN beam is shown in fig. 1.17.

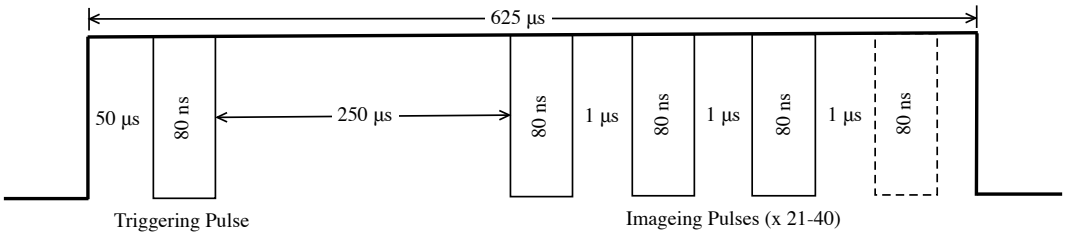

Figure 1.16: pRAD experimental area beam structure.

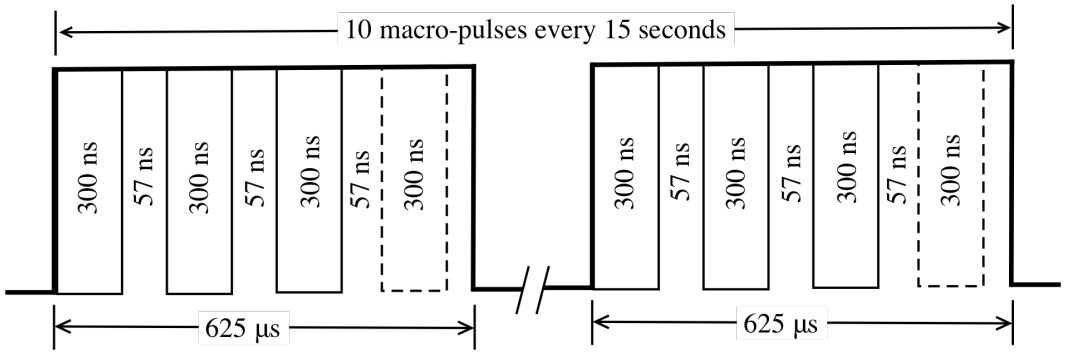

Figure 1.17: UCN experimental area beam structure.

1.3 Beam Losses and Loss Detection

Beam loss is created when particles within a bunch fall outside of either the transverse or longitudinal acceptance of the accelerator. The LANSCE facility utilizes beam losses as a primary metric for tuning the accelerator. Nominal high energy beam losses during a production run cycle are shown in fig. 1.18. The goal of accelerator operations is to safely deliver production level beam currents to the user facilities with minimal beam losses.

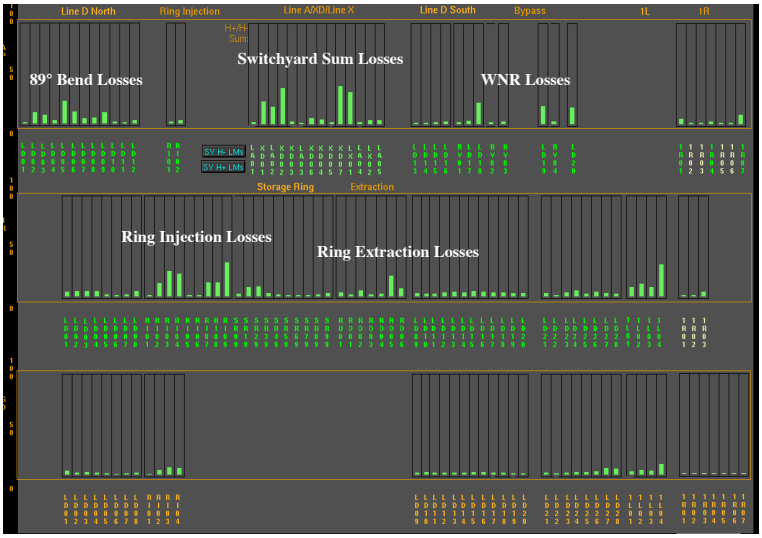

Figure 1.18: LANSCE high energy beam losses.

There are three mechanisms for beam loss in the H^- beam that does not exist with the H^+ beam at LANSCE: intrabeam stripping, residual gas stripping, and Lorentz stripping. Intrabeam stripping is the process of a single electron stripping within the bunch due to binary collisions between H^- ions. Lorentz stripping is the process of stripping the weakly bound electron from the H^- atom by a strong magnetic field. Residual gas stripping is the process of H^- beam particles scattering from gas atoms within the vacuum chamber. Figure 1.19 shows the average vacuum ion gauge readings throughout the LANSCE accelerator facility.

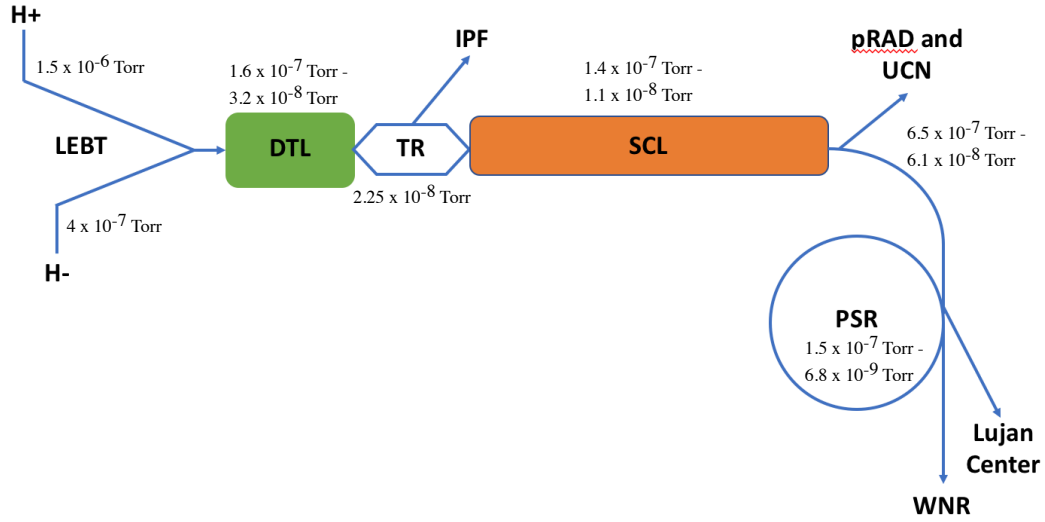

Figure 1.19: Average vacuum throughout the LANSCE accelerator facility recorded from ion gauge readings at the end of the 2017 production run cycle.

Beam losses are measured by three different devices at LANSCE. The activation protection (AP) system consists of scintillation detectors that are calibrated so that 80% integrated signal output is equivalent to 100 nA of beam loss. The AP cans can also act as a loss monitor where the signal is not integrated and beam loss changes across the beam pulse can be monitored (see fig. 1.20). Ion chamber (IR) detectors are used in the high energy beam transport lines. IR detectors are located in parallel with gamma detection (GD) detectors, which provide a signal into the Radiation Safety System (see fig. 1.21). The IR and GD chambers are used in place of AP because they will not saturate at low duty factors. The final way to measure beam loss is with hardware transmission monitors (HWTM). The HWTM system measures the beam current differences between current monitors and reports that difference as beam loss.

Figure 1.20: LANSCE activation protection (AP) and loss monitor (LM) scintillation detectors.

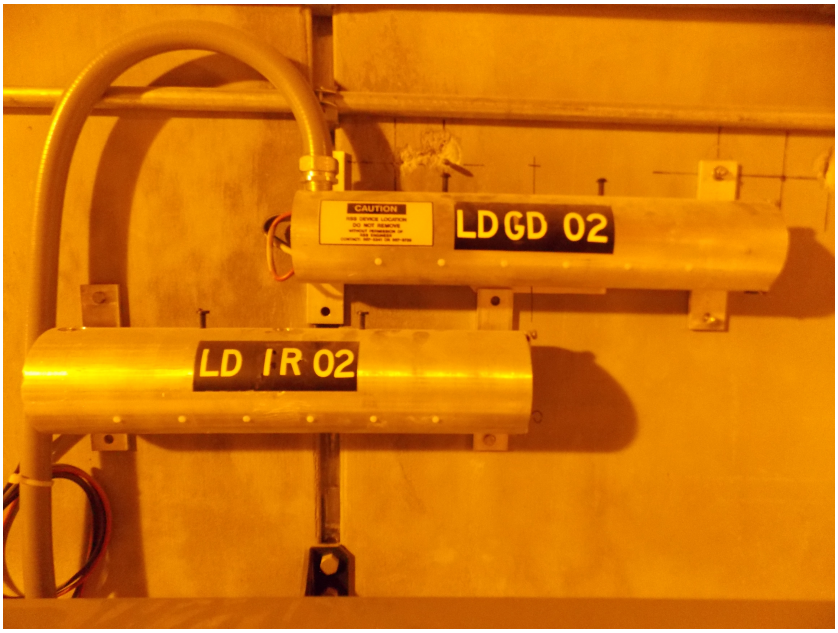

Figure 1.21: LANSCE ion chamber (IR) and gamma detector (GD) beam loss devices.

AP loss detectors report beam losses in percentages to the control system. Also, the response from the AP detectors follow a log-log relationship between the voltage applied to the can and the signal output current. Therefore, if the AP detector high voltage is reduced during tuning operations, the displayed beam loss does not scale linearly with the voltage reduction.

To determine a method of obtaining actual beam loss from an AP signal (even if the AP has a high voltage reduction), several AP responses were plotted and fit within the normal operating voltage of the detector (50 to 700 V) with a logarithmic line. The responses of AP's 02AP01, 04AP01, TRAP01, IPAP01, and 05AP01were fit with a log-log function, as can be seen in fig. 1.22.

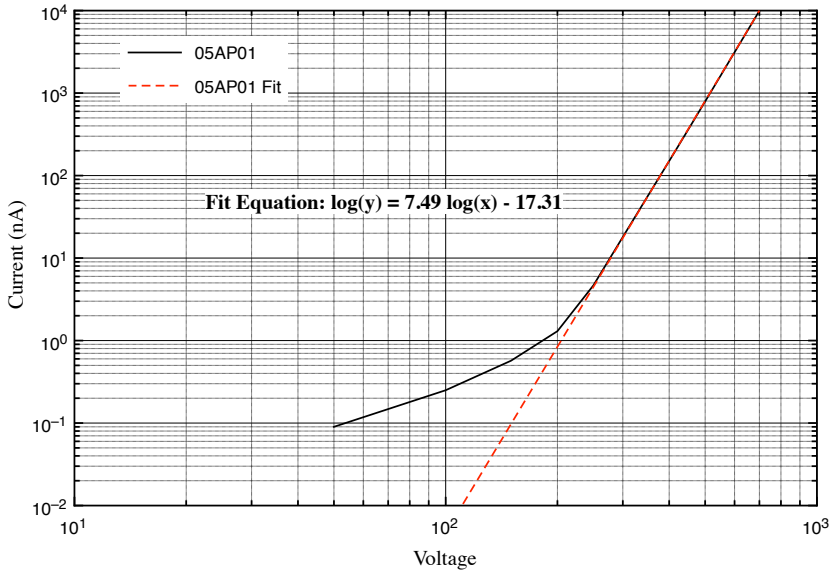

Figure 1.22: Calibration response of 05AP01 and its corresponding logarithmic line fit.

From these fits one can define the parameters of the standard equation for the line within the operating range of the AP high voltage:

$$I_{spill}\,(nA) = F_{voltage} \times AP\,Reading\,(\%) \times \left(\frac{100\,nA}{80\%}\right)\,, \tag{1.1}$$

where $F_{voltage}$ is the voltage factor that will account for any reductions in AP voltage from its calibrated value. The $F_{voltage}$ will equal 1 if there is no high voltage reduction on the AP detector. The voltage factor can be found by:

$$F_{voltage} = \left(\frac{10^{7.6\log V_0 - 17.75}}{10^{7.6\log V_f - 17.75}}\right)\,, \tag{1.2}$$

where V_0 is the calibrated AP high voltage and V_f is the actual voltage of the AP during production operations. For example, it is known that a 10% reduction in AP high voltage corresponds to an approximate reduction in AP detector sensitivity by 55%. If we assume that V_0 is 500 V and given a 10% reduction on the high voltage, we come to a voltage factor, $F_{voltage}$, equal to 2.22 which equates exactly to a 55% reduction in sensitivity.

1.4 Accelerator Reliability

The goal for beam reliability at LANSCE is greater than 80% of the scheduled beam time. Reliability is defined as the amount of beam time delivered divided by the amount of scheduled beam time. Reliability is measured automatically by the accelerator control system. A beam experimental area will be scheduled in production and a current monitor assigned to record beam performance. If that current monitor drops below 50% of the scheduled average current, the system automatically generates a out-of-production condition and allows the operators to document an associated system to that out-of-production. This system allows LANSCE to not only track the amount of beam downtime, but to understand what systems (high power RF, low level RF, magnet power supplies, vacuum, etc.) are contributing to that downtime. Figure 1.2 describes the areas that can be ascribed by the operations personnel as a root cause for the beam downtime.

Table 1.2: Guide for assigning causes for beam unavailability [12].

201	201 RF: pad power supplies, Cap. rooms, amplifier systems, failed interlocks (OL, temp, etc.), low cooling flow, resonance controllers and valves.
805	805 RF: pad power supplies, Cap. rooms, amplifier systems, Klystron systems, interlocks (OL, temp, etc.), low cooling flow, resonance controllers and valves.
CTRL-HW	Computer, control system and network hardware. Includes hardware on VAX's, Suns, remotes, CAMAC, VME, RICE, ADS, networks, console equipment, printers, knobs, etc. Excludes Master Timer.
CTRL-SW	Computer, control system and network software. Includes software on VAX's, Suns and remotes.
DIAG	Problems with harps, wire scanners, current monitors, Delta T hardware, strippers, scrapers, emittance systems, and BPMs.
DC-MAG	DC magnets, DC cabling, temperature switches, low flow, vacuum and water leaks, magnet water strainers. Does not include power supplies.
DC-MAG-PS	DC power supplies, trips, interlocks (OL, low cooling flow, ripple, etc.)
EXPT	Flight paths, shutters and secondary beam lines, experimenter requested beam-off, any experimenter systems (target, vacuum, etc.)
FACILITY	Facility problems not elsewhere on the list (water main leaks, compressed air, natural gas, etc.)
HVAC	Heating, ventilation and Air Conditioning system failures that cause downtime.
INJ	Ion sources, ion source support equipment and LEBT Choppers and Chopper power supplies. Includes ion source power supplies, 80KV/670KV/750KV columns and power supplies. (Deflectors are in PULS-PWR. LEBT bunchers are LL-RF. Diagnostics are DIAG.)
INTLKS	Fast Protect, Run Permit, HWTM, LM and AP problems. Weekly RSS checks. Interlock checks during scheduled production that are not required by an RSS trip. Failures of interlock hardware. If an RSS trip report is required, see RSS-TRIP.
LL-RF	All bunchers including LFB, Pre Bunchers, Main Buncher, and PSR Buncher. RF Sources.
OTHER	Cause is known but does not fit in above categories. Use comments to identify.
POWER	Site power, the AC electrical distribution system for 110V and above. Includes outlets, breaker failures, power line surges, etc.
PULS-PWR	Kickers, deflectors and their related power supplies, local controls and modulators.
RSS-TRIP	RSS/PSS trips. E.g. SCRAM switch actuation, doors rattled, high spill on GD, XL sees too high current, etc. Anything requiring an RSS trip report.
TARGETS	All production targets, target boxes, beam stops, proton inserts, degraders, isotope stringers and foils. Includes low cooling flow, temperature interlocks and water and vacuum leaks. Does not include targets that belong to the experimenters (PRAD, Target 2 irradiation, etc.) - Problems with these are assigned to EXPT
TIMING	Problems with Master Timer and timing signal distribution.
TUNE-RECOVERY	Tuning other than TUNE-UP. **Spill**. High losses. Off-energy beam, micro-pulse contamination, off-center beam at 1L target, etc.
TUNE-UP	Tuning to bring beam to production status after scheduled down-time periods such as inter-cycle breaks and maintenance days. Tuning to recover after down-time caused by equipment failure is attributed to the failed system.
UNKNOWN	Cause of down-time cannot be identified.
VACUUM	Vacuum system: Vacuum pumps, pump power supplies, roughing packages, valves, instrumentation, controls, pipes, flanges. Does not include leaks in individual components or loads such as magnets, targets, etc.
WATER	**Programmatic Cooling Water Systems**: pumps, pump controls, failed flow switches, makeup water, valves, pipes, heat exchangers, loss of cooling capacity. • **Includes**: Water systems from the programmatic distribution point (water cabinet, distribution manifold, etc.) to the load/load distribution manifold/cabinet. • **Does not include**: leaks and flow problems in individual cooled components such as magnets, amplifiers, cavities, etc. unless problem is caused by variations or limits in the programmatic water system.
WATER-FAC	**Facility Cooling Water Systems**: pumps, pump controls, failed flow switches, makeup water, valves, pipes, heat exchangers, loss of cooling capacity. • **Includes**: Facility Water Systems up to their programmatic distribution points (water cabinets, distribution manifolds, etc.) • **Does not include**: leaks and flow problems in individual cooled components such as magnets, amplifiers, cavities, etc. unless problem is caused by variations or limits in the facility water system.

With the reliability data we can now analysis the LANSCE accelerator complex for trends in reliability by year and by primer systems. Figure 1.23 shows the reliability numbers for the past 10 years of LANSCE operations [12].

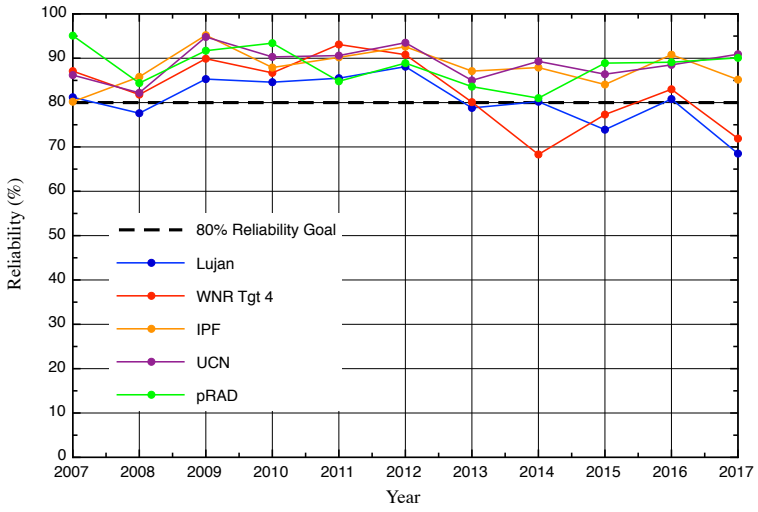

Figure 1.23: LANSCE beam reliability by experimental area for the past 10 years.

Table 1.3 shows the major contributions by system to the beam downtime for the Lujan Center and WNR experimental areas in the 2017 production run cycle [12]. Figure 1.24 shows the average downtime per out-of-production condition by accelerator system for the 2017 Lujan Experimental Area production run cycle [12].

Table 1.3: LANSCE 2017 major contributions to beam downtime by system for the Lujan and WNR experimental areas.

System	Lujan Center	WNR
Tune Recovery	7.76%	7.48%
Vacuum	6.18%	4.27%
Injector	3.2%	3.13%
201RF	2.84%	2.72%
805RF	1.49%	1.37%
Water	1.43%	1.38%

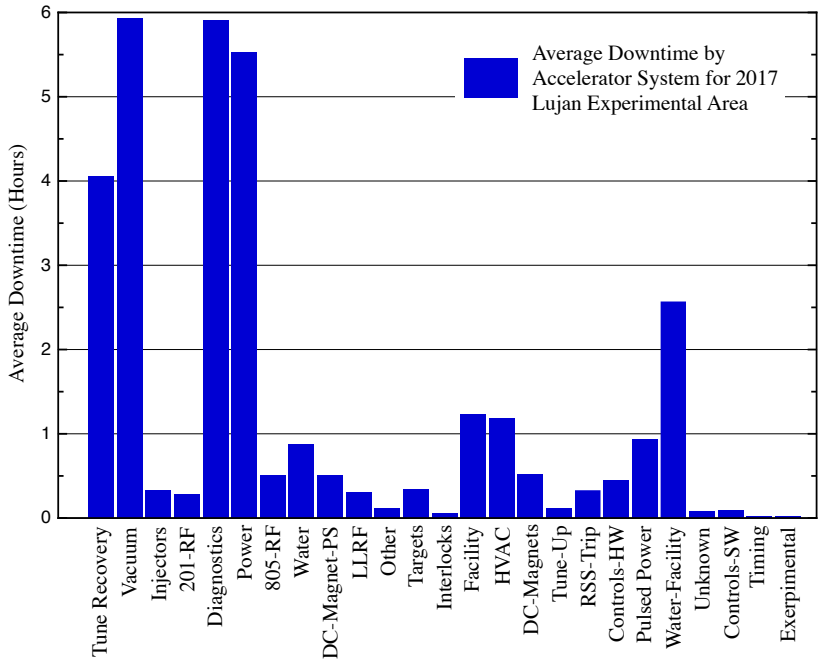

Figure 1.24: Average beam downtime by system for the 2017 Lujan Experimental Area production run cycle.

If we look at both fig 1.23 and table1.3, approximately 44% of beam downtime at the Lujan Center and approximately 42% of beam downtime at the WNR experimental area were caused by tune recovery and vacuum problems. If we look closer at the vacuum downtime, 79.7% of that downtime occurred during the machine turn-on periods and is directly related to an improper tune in the side-coupled linac causing vacuum leaks in the beam switchyard.

To further understand the trend and prime drivers for lost beam time, we can analyze the availability data for LANSCE for the past ten years. Figure 1.25 shows the past ten years of downtime contributions by systems for the Lujan experimental area following the guide provided in fig. 1.2. The Lujan experimental area was chosen because it is the highest power beam delivered at LANSCE and is historically the more difficult beam to maintain in a production status. The percentages in fig. 1.2 reflect the total contribution of that particular system to the total downtime for the experimental area.

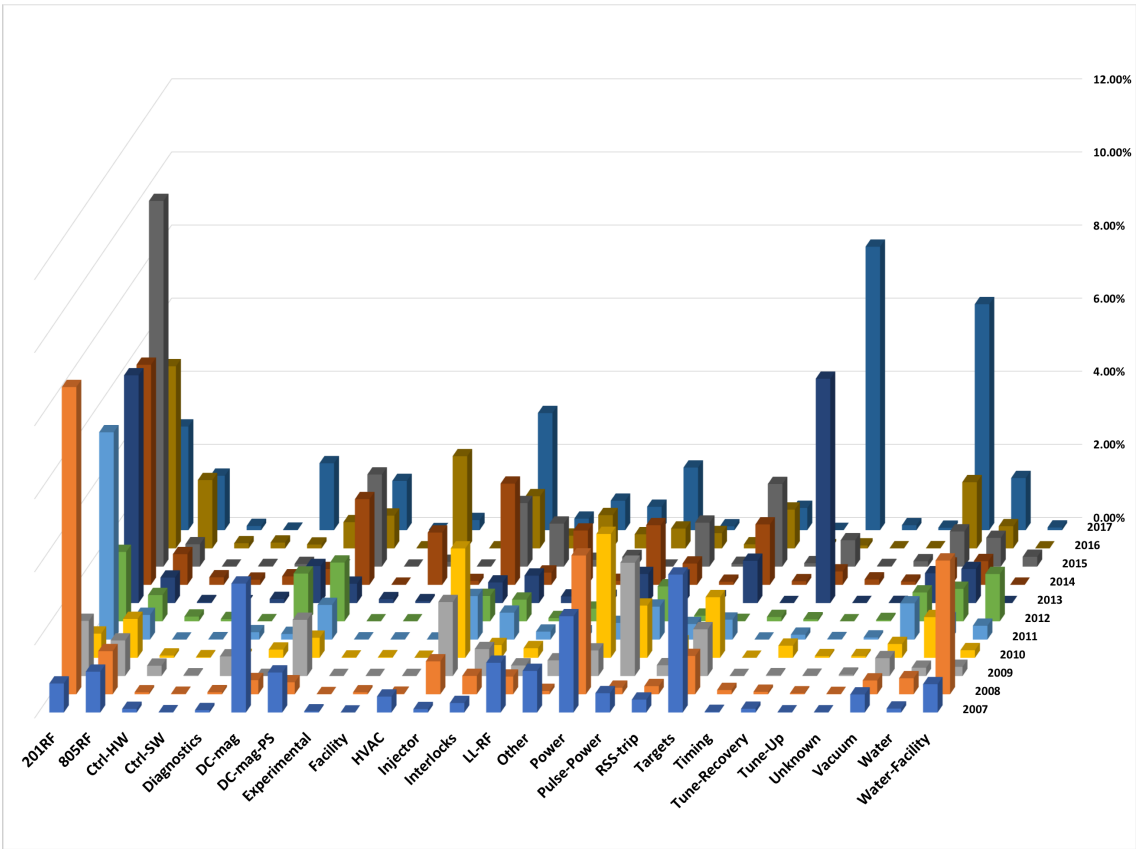

Figure 1.25: LANSCE beam downtime contributions by system for the past 10 years for the Lujan experimental area.

Figure 1.25 shows that the significant drivers of beam downtime historically are the 201RF, Injector, Power, and Magnets. In recent years, there has been a trend in a loss of availability due to Tune Recovery and Vacuum. Also, we see from fig. 1.24 that the average recovery time for out-of-production conditions related to tune recovery is large. Therefore, any stability and tune recovery studies should focus on the systems which are historically major contributors to the beam downtime and address the systems which have increase their contribution trend.

Chapter 2

Injectors and Low Energy Beam Transport

2.1 H^+ Source and LEBT Dynamics

The H^+ source is a Duoplasmatron Source that provides approximately 12 mA of H^+ beam to ground at 100 Hz during normal operations. The H^+ beam pulse length is 625 μsec. After the H^+ source, the beam is accelerated to 750 KeV by a Cockcroft-Walton generator. Excess H_2^+ beam is removed in an 81° bend that directs the beam towards the point in the LEBT where H^+ and H^- beams are combined.

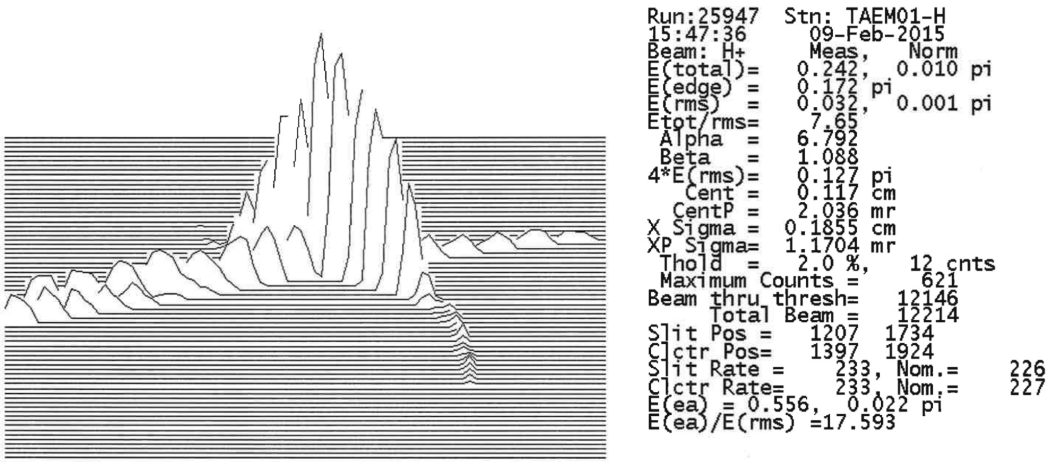

Figure 2.1: Example of horizontal measured at the output of the H^+ Injector prior to H_2^+ beam removal.

The beam dynamics are set in the H^+ LEBT with the use of several slit and collector style emittance measurement devices and the TRACE 2D envelope code. Figure 2.2 shows an example of the H^+ LEBT beam profiles with the location of several critical devices in the beam line.

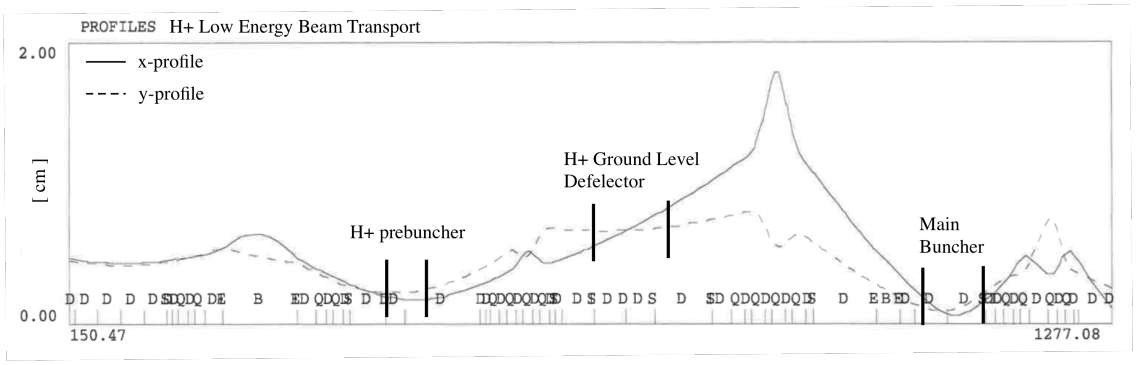

Figure 2.2: LANSCE H^+ LEBT beam profiles.

2.2 H^- Source and LEBT Dynamics

The H^- Source is a multicusp, surface production source with a large converter electrode. Cesium is added to lower the plasma temperature and enhance the electron attachment to the H^+ ion. Approximately 1-2% of the H^+ converts into H^- and are repelled towards the source extraction by the converter. The dipole cusped field at the extraction region suppresses the secondary electrons from the converter, and the repeller electrode suppresses the plasma electrons.

The H^- Source at production levels provides 13.5 mA of peak H^- beam to ground at 120 Hz and has a lifetime of approximately 28 days. Typical value of normalized rms beam emittance extracted from the H^- source is 0.2 $\pi\, mm\, mrad$ [1]. After the beam leaves the source it is accelerated to 80 KeV and then propagated through a 4.5° bend that removes any electrons that escaped the source. Once all excess electrons are removed, the beam proceeds into a Cockcroft-Walton generator and accelerated to 670 KeV. The final beam energy at ground thus matches that of H^+ at 750 KeV.

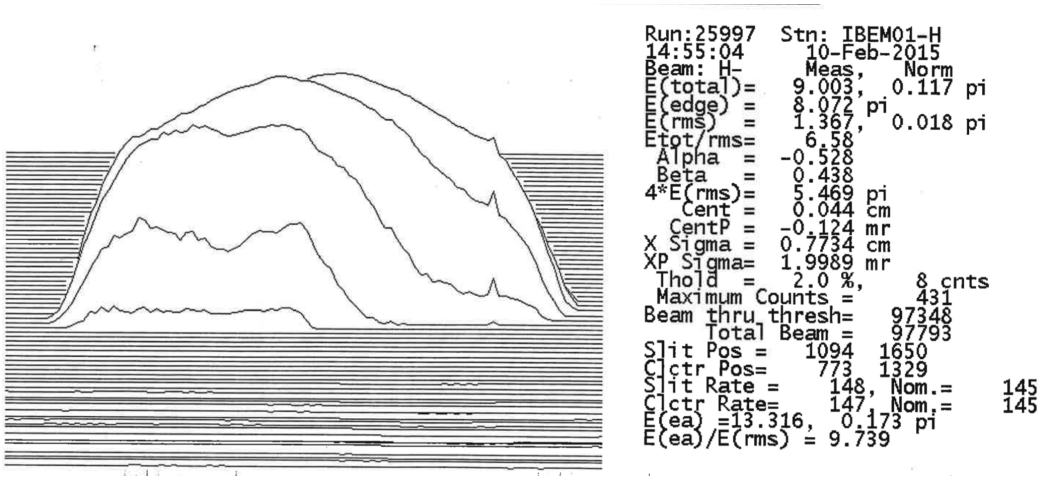

Figure 2.3: Example of horizontal emittance measured at the output of the H- Injector.

The H- LEBT tune is set by utilizing several slit and collector emittance stations with the TRACE 2D envelope code to set the Twiss parameters at critical points of the transport. Figure 2.4 shows an example of the beam profiles in the H- LEBT. Several beam waists are established at the H- chopper, the different RF bunchers, and the ground level deflector. The H- chopper has a Krausse Modulation system that modulates the beginning of the H- beam pulse to minimize beam loading and turn on transients for the downstream RF systems.

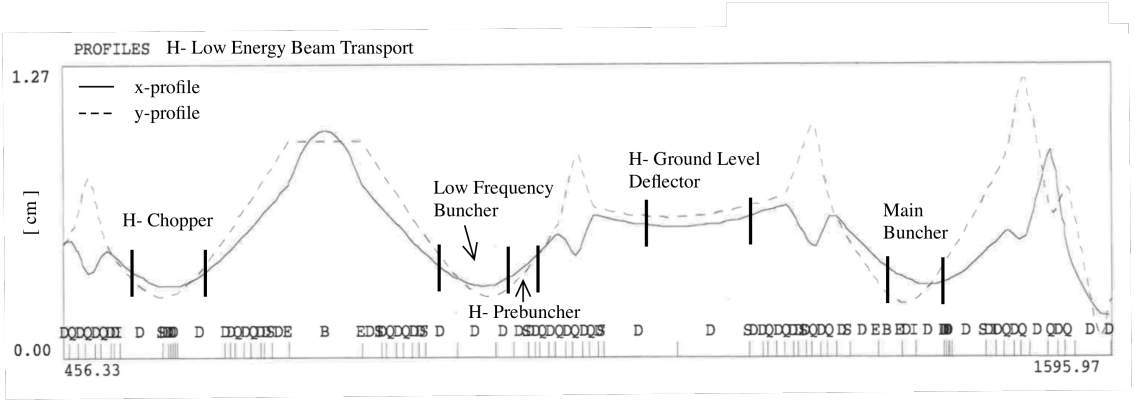

Figure 2.4: LANSCE H- LEBT beam profiles.

2.3 High Voltage Droop Effect on H- Beam Stability

A H- 80 kV droop across the beam pulse has been identified as a possible source of poor H- beam performance in recent years. High voltage droop in the H- has been correlated with an increase in

beam losses.

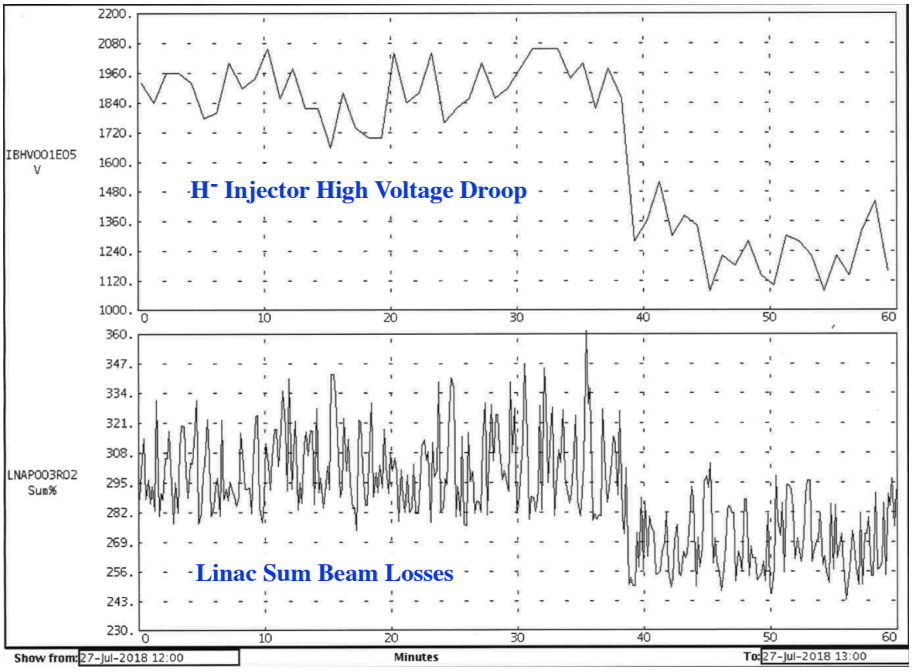

Figure 2.5: Correlation of H^- high voltage droop and linac sum beam losses.

Also, during the machine turn-on period, a procedure named delta-t, or ΔT, is used to find the phase and amplitude set-points of the 805-Mhz side-coupled cavity linac. It is named so because of its relative time-of-flight measurements that are required. The success of the ΔT procedure depends on the energy structure of the beam being reproducible on a pulse-to-pulse basis. This is because the measurement takes data on two separate beam pulses [21], and variation can create differing ΔT response with the measured sampling time. Therefore, an understanding of the sources of energy variations across the beam macro pulse is imperative to successful beam tuning and overall beam stability.

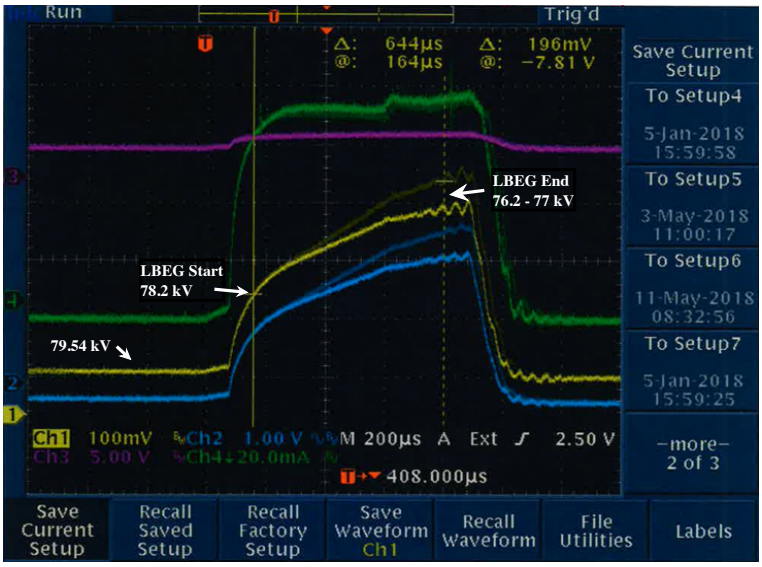

Figure 2.6: 80-kV Droop measured across the H^- macro pulse.

It was noted during the H^- source testing in April-May 2018 that the 80 kV droop could be reduced by increasing the H^- Repeller Voltage (see fig. 2.7). By doing this we are removing thermal electrons from ion source output beam and the 80 kV power supply can more effectively regulate the droop. However, increasing the repeller voltage will reduce the H^- current coming out of the source to ground. LBEG current to ground at TBCM01 drops by approximately 1 mA when raising repeller voltage from 0.55 V to 5.0 V.

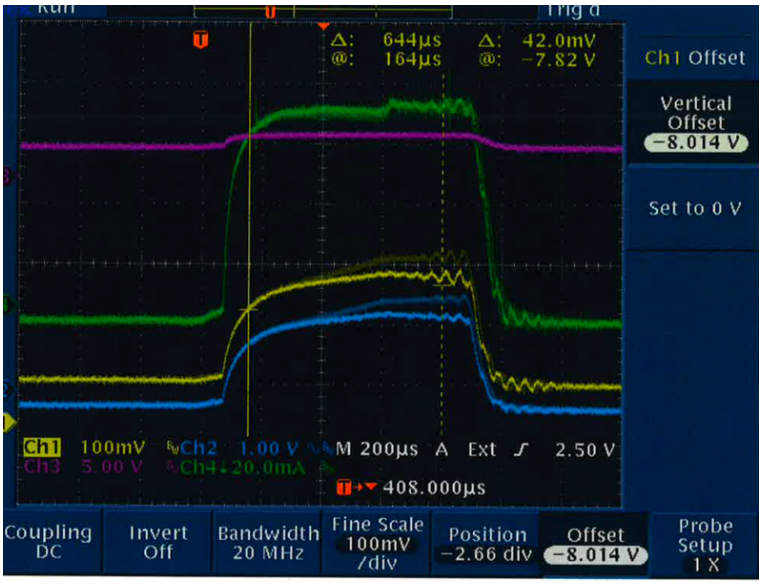

Figure 2.7: 80-kV Droop measured across the H^- macro pulse with H^- Repeller set to 3.14 V.

Horizontal displacement across the LBEG pulse has been noted in the side coupled linac and switchyard BPMs. The studied used the horizontal Harp (TDHP01-H) to measure the beam at different times in the H^- macro pulse.

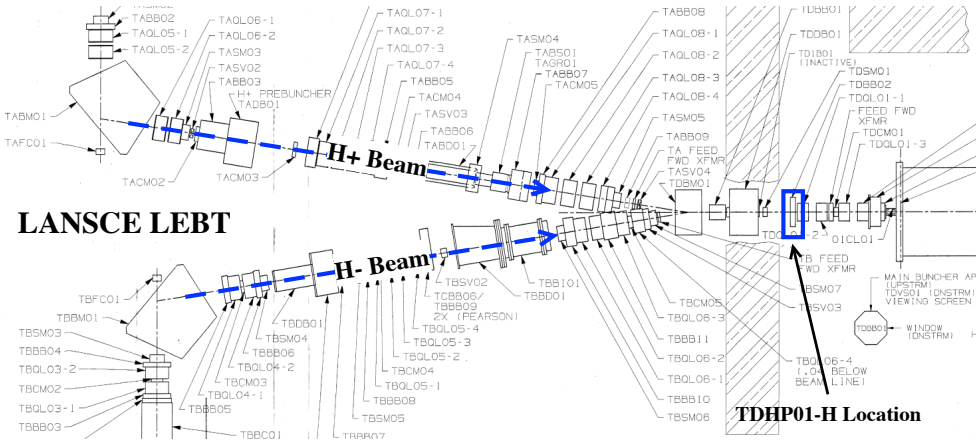

Figure 2.8: Location of the horizontal Harp used for the high voltage droop study.

From this data we can extract the effective horizontal displacement across the LBEG macro pulse, which can then be correlated to energy changes across the H^- macro pulse. This measurement was then performed with different repeller voltages to see the effect of the droop on horizontal displacement across the beam pulse. TDHP01-H measurements were taken with LBEG length at 50 μsec and delays at 400, 510, 700, and 950 μsec. The H^- macro pulse begins at 375 μsec and ends at 1000 μsec. The H^- Chopper was on for these measurements, with the Krausse Modulation disabled at the H^- ground level deflector.

To calibrate the effect of 80 kV droop on the relative momentum spread of the beam we note that:

$$\frac{dW}{W} = \left(1 + \frac{1}{\gamma}\right)\frac{dP}{P} \tag{2.1}$$

Therefore, a 1-keV droop in the 750-keV LEBT beam results in a $\frac{dp}{p} = 0.066\%$. We utilized TRACE by inputting the TBEM01 data from the turn-on and tracing forward to TDHP01. The magnet settings were those found in the last Transport B tune. By adjusting the $\frac{dp}{p}$ in TRACE, we could simulate the horizontal displacement of the beam at the TDHP01 location and correlate that to the measurements. Figure 2.9 shows an example of TRACE envelopes and beam displacement with $\frac{dp}{p} = 0.1\%$ from TBEM01 to TDHP01.

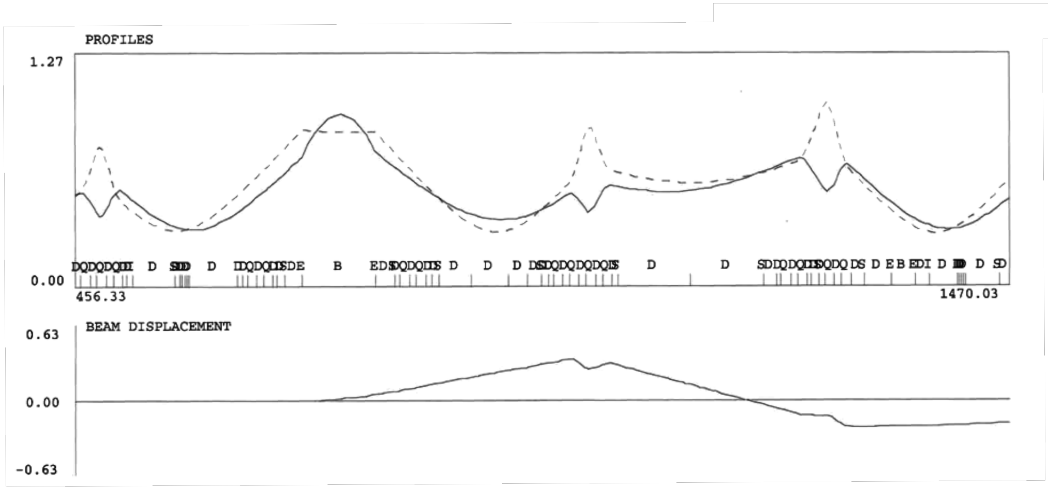

Figure 2.9: TRACE simulated envelopes and beam displacement with $\frac{dp}{p} = 0.1\%$.

The results from the beam measurements are shown in fig. 2.10 and include the 80-kV droop valued measured using an installed scope inside the H^- Injector. Figure 2.11 shows the horizontal displacement as a function of the H^- beam macro-pulse with maximum 80-kV droop.

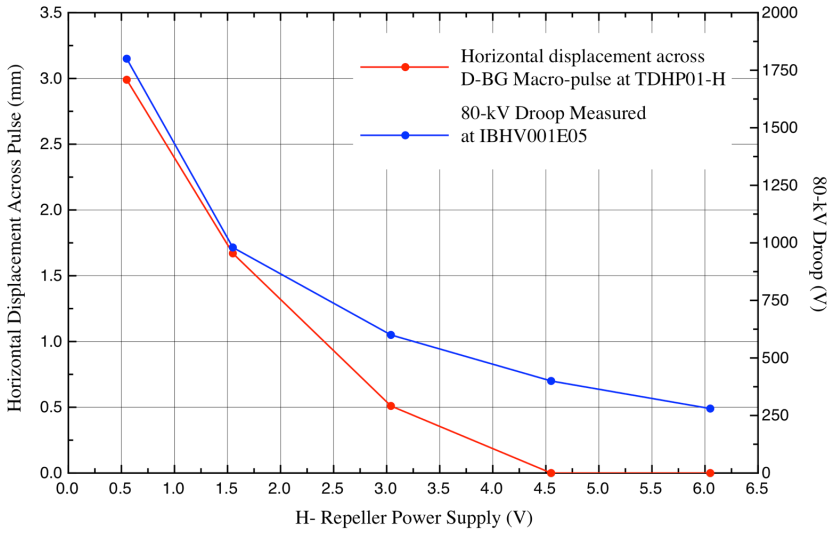

Figure 2.10: Results from the H^- high voltage droop study.

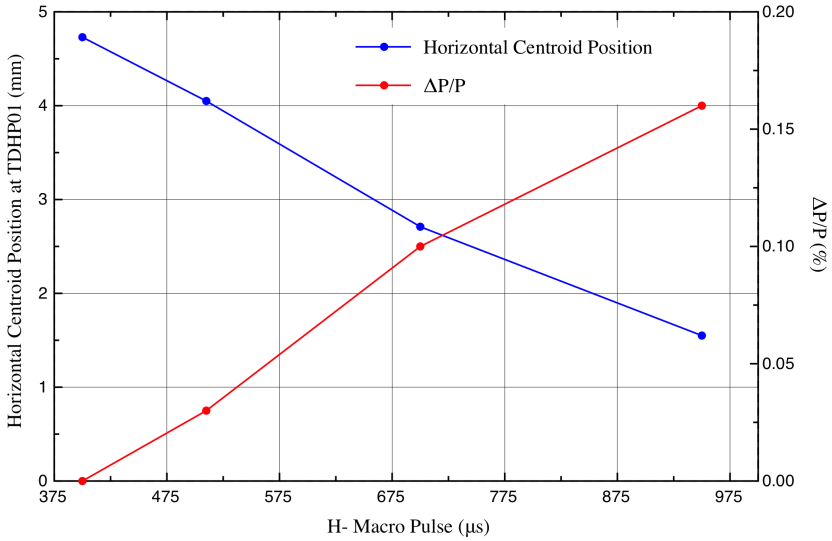

Figure 2.11: Measurement of the horizontal displacement across the H^- macro pulse with 1800V of droop.

The TRACE simulations include both the droop from the 80-kV regulator and the 670-kV Cockcroft-Walton. The 670-kV Cockcroft-Walton droop was measured with the scope in the injector control room as shown in fig. 2.12.

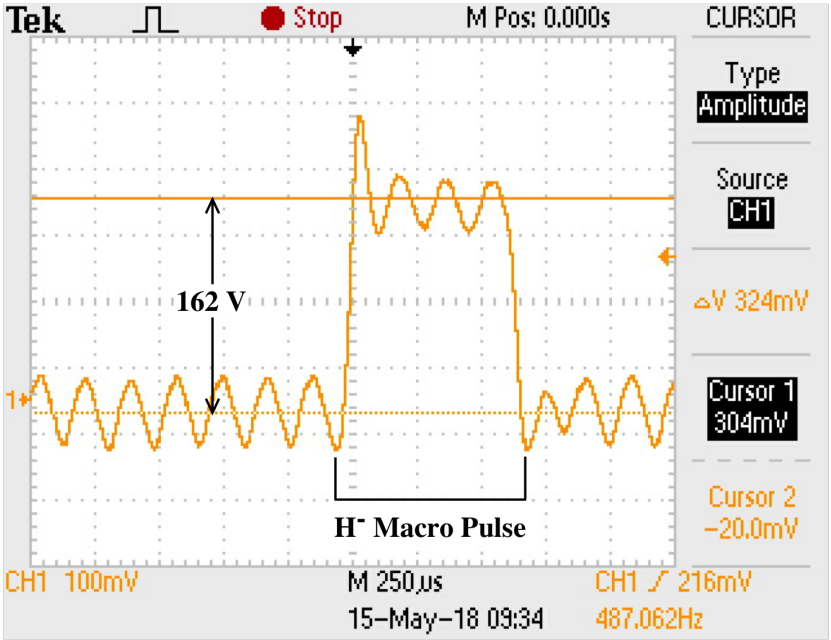

Figure 2.12: Droop across the beam pulse from the 670-kV Cockcroft-Walton Generator where 100 mV is equal to 50 V of droop.

This measurement shows that the 670-kV droop is 162 V, which can then be added to the 1800-V

droop measured at the 80-kV regulator. Utilizing Equation 2.1, the total measured droop of 1.962 kV equates to a $\frac{dp}{p} = 0.13\%$. utilizing the TRACE simulations and the Harp horizontal displacement measurement found a maximum $\frac{dp}{p} = 0.16\%$ across the H^- macro pulse.

The Transport D line where the measurements were performed is the intersecting point of the H^+ and H^- beams at LANSCE. It is therefore possible to perform the measurement across the H^+ beam pulse to compare with those of the H^- beam pulse. The H^+ high voltage accelerating system consists of only a 750-kV Cockcroft-Walton generator. The H^+ beam was measured at three points across the pulse and showed no horizontal displacement. The same measurement was also performed on the H^- beam but measuring the vertical displacement with TDHP01-V. This measurement also showed no change in the vertical position across the beam pulse.

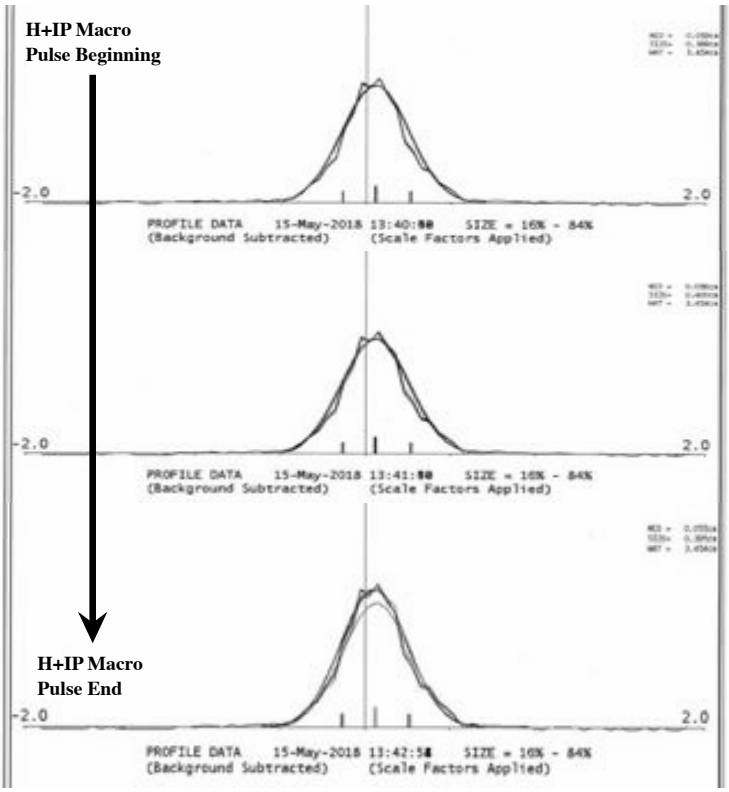

Figure 2.13: Horizontal displacement measured across the H^+ beam pulse.

The amount of horizontal displacement and corresponding momentum spread is not acceptable for stable operations. It was proposed that driving the filaments harder in the 80-kV power supply that the regulator would enable it to handle the beam loading. A Variac autotransformer was installed on the power supply to the 80-kV power supply. The Variac was then adjusted to several

positions and the droop measured at each point. With a combination of the Variac set-point and increasing H^- repeller voltage, we were able to minimize the high voltage droop enough to allow for production operations.

With this study, we were able to measure and quantify the effects of droop from the high voltage accelerating systems on the H^- beam. It was shown that the droop introduced unacceptable amounts of momentum spread into the beam. The study also showed that the H^+ beam did not suffer from the same energy variations across the macro pulse. A temporary solution was found using the H- repeller and a Variac autotransformer while a more permanent solution could be developed.

Chapter 3

Drift Tube Linear Accelerator Section

3.1 Drift Tube Linear Accelerator (DTL) Beam Dynamics

In preparation for further simulation development, the general beam dynamic parameters were calculated for the DTL. Equations used were found in references [8], [9], and [15].

The longitudinal beam dynamics were found by first solving for the transit time factor. The transit time factor describes how effective the transformation is for the RF field into particle energy gain. It is mostly dependent on RF gap geometry. In accelerators where the aperture of the channel is substantially smaller than the wavelength, the transit time factor is defined by eq. 3.1, where g is the gap, β is the velocity, λ is the RF wavelength, and a is the aperture radius of the channel.

$$T = \frac{1}{I_0\left(\frac{2\pi a}{\beta\gamma\lambda}\right)} \frac{\sin\left(\frac{\pi g}{\beta\lambda}\right)}{\frac{\pi g}{\beta\lambda}} \tag{3.1}$$

The calculated transit time factors are shown in Figure 3.1.

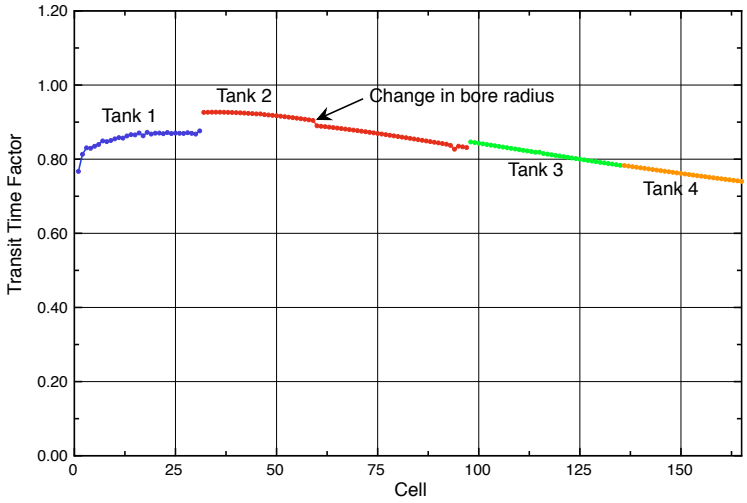

Figure 3.1: Transit time factors of the LANSCE DTL.

The calculated transit time factors can be used to determine the accelerating field for each DTL cell. The DTL cells are defined as the distance from the center of one drift tube to the center of the next drift tube. The accelerating field is found by:

$$E = E_0 T \tag{3.2}$$

The average field values, E_0, were found in original design documentation. The calculated accelerating fields through the four DTL tanks are shown in fig. 3.2.

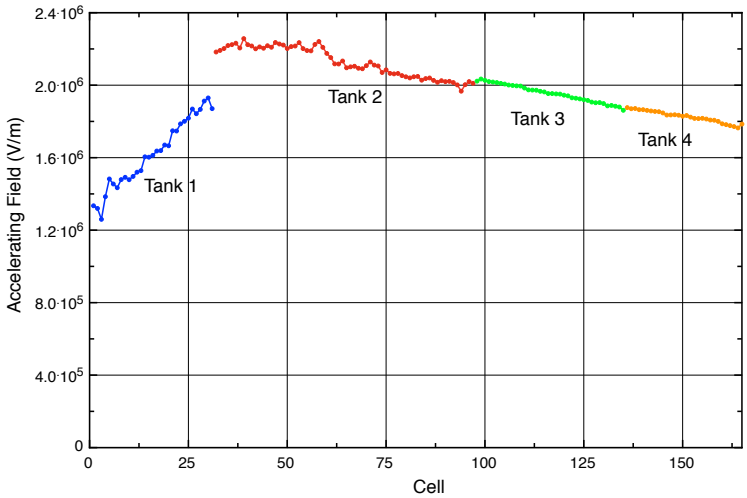

Figure 3.2: Accelerating Fields of the LANSCE DTL.

From the accelerating field and by noting that the designed $\varphi_s = -26°$ for all the DTL tanks, we can now find the dimensionless frequency of small amplitude linear oscillations by:

$$\frac{\Omega}{\omega} = \sqrt{\frac{qE\lambda\,|\sin\varphi_s|}{mc^2 2\pi\beta\gamma^3}} \tag{3.3}$$

The small amplitude linear oscillations will be used to determine the half-maximum of the separatrix in momentum $\left(\frac{\Delta p}{mc}\right)$, the phase advance of longitudinal oscillations per focusing period ($\mu_{0\ell}$), and to find the normalized longitudinal acceptance (ε_{acc}) through the following equations:

$$\frac{\Delta p}{mc} = 2\beta\gamma^3 \left(\frac{\Omega}{\omega}\right) \sqrt{1 - \frac{\varphi_s}{\tan\varphi_s}} \tag{3.4}$$

$$\mu_{0\ell} = \sqrt{2\pi \left(\frac{qe\lambda}{mc^2}\right) \frac{|\sin\varphi_s|}{\beta\gamma^3}} \left(\frac{S}{\beta\lambda}\right) \tag{3.5}$$

$$\varepsilon_{acc} = \frac{2}{\pi}\lambda\beta^2\gamma^3 \left(\frac{\Omega}{\omega}\right) \left(1 - \frac{\varphi_s}{\tan\varphi_s}\right) \tag{3.6}$$

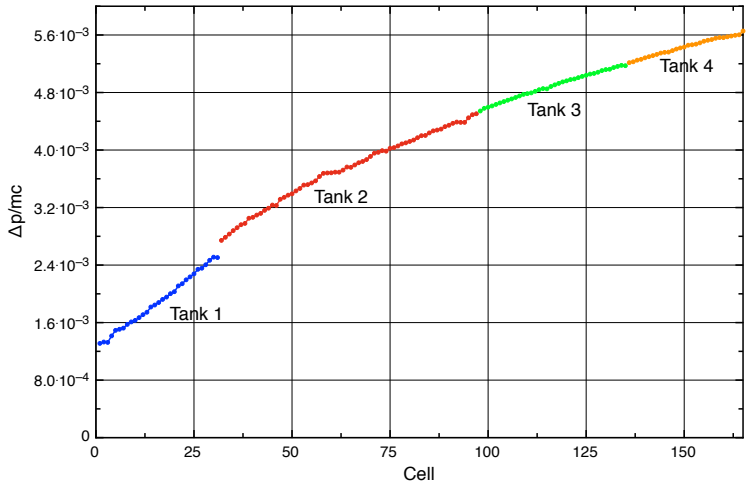

Figure 3.3: Half-maximum of separatrix in momentum of LANSCE DTL.

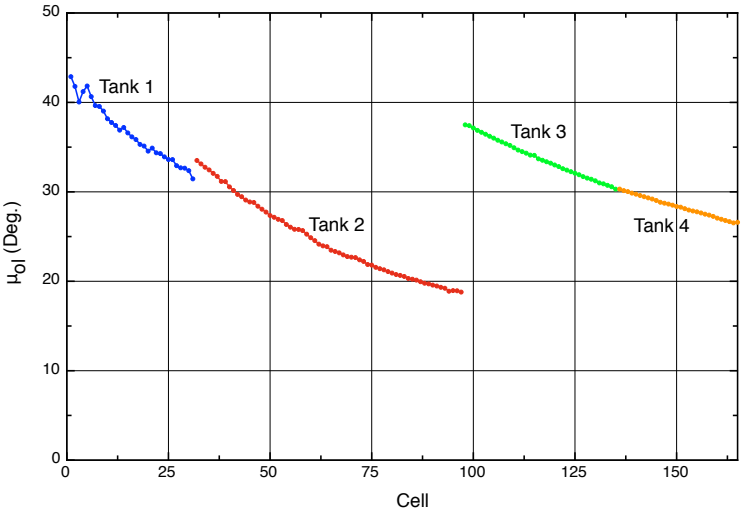

Figure 3.4: Phase advance of longitudinal oscillations per focusing period of LANSCE DTL.

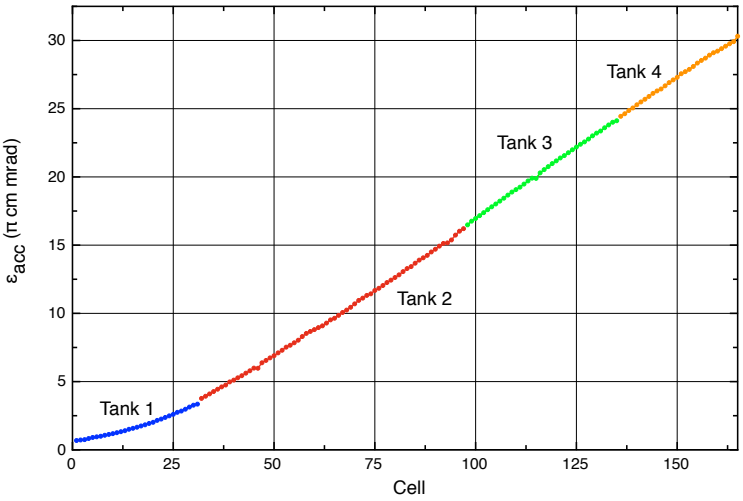

Figure 3.5: Normalized longitudinal acceptance of LANSCE DTL.

For the transverse calculations, the operational values of the quadrupole magnets were used instead of the original design values. This was done in order to get a representative idea of the basic operational transverse beam dynamics. The setup for the transverse calculations are shown in fig. 3.6.

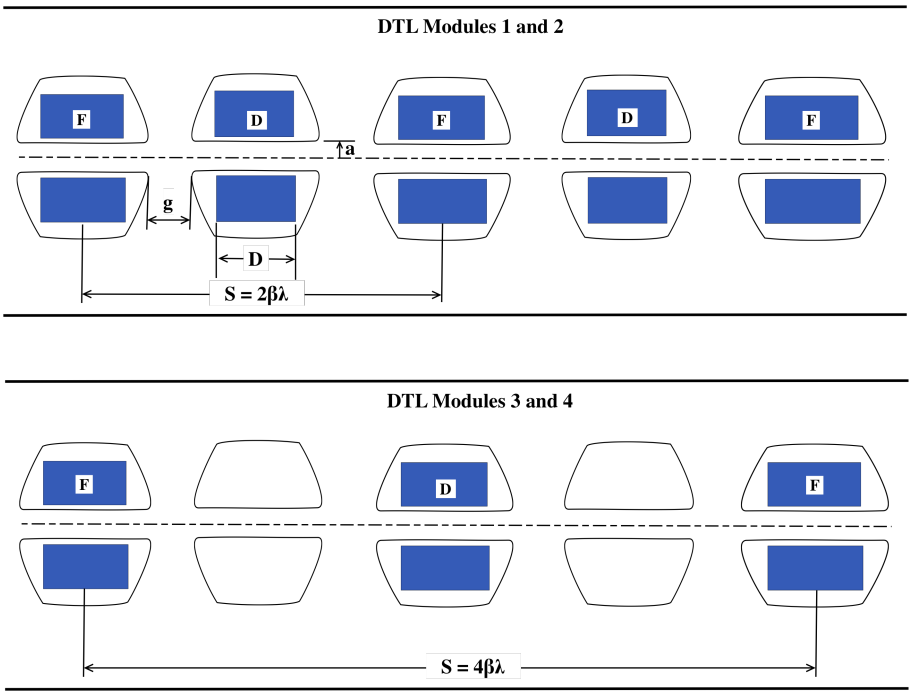

Figure 3.6: LANSCE DTL FODO structure.

The focusing period, S, changes depending on the DTL tank being calculated. Tanks 1 and 2 have a period of $S = 2\beta\lambda$, while Tanks 3 and 4 have a period of $S = 4\beta\lambda$. This is because the quadrupoles in tanks 3 and 4 are located in every other drift tube. The equation for the phase advance of transverse oscillations in the FODO focusing structure is:

$$\mu_0 = \frac{S}{2D}\sqrt{1 - \frac{4D}{3S}}\frac{qGD^2}{mc\beta\gamma} \tag{3.7}$$

The values calculated for transverse phase advance are shown in fig. 3.7.

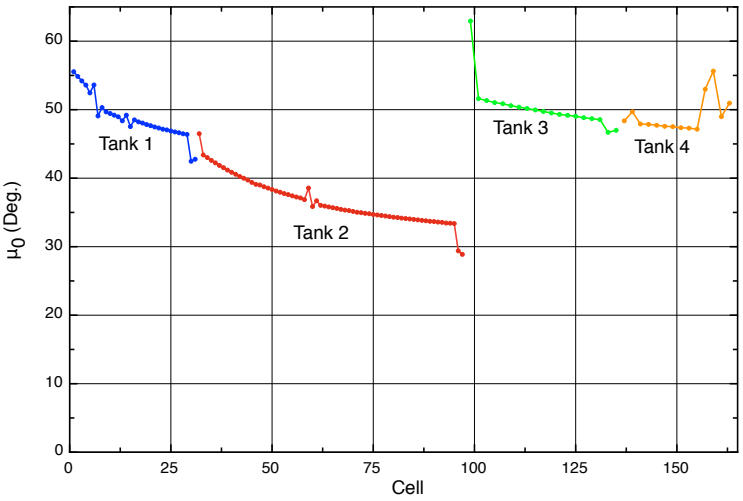

Figure 3.7: Phase advance of transverse oscillations in the LANSCE DTL focusing structure.

After the longitudinal and transverse phase advances are calculated, the phase advance of the synchronous particle at the period of the focusing structure and in the RF field can be determined using the equation:

$$\mu_s = \mu_0 \sqrt{1 - \frac{\mu_{0\ell}^2}{2\mu_0^2}} \tag{3.8}$$

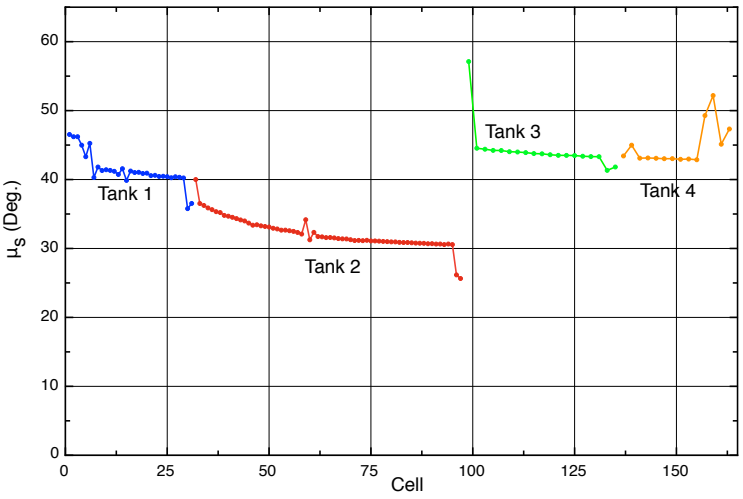

Figure 3.8: Phase advance of transverse oscillations of synchronous particle at the focusing period of the LANSCE DTL.

With the phase advance of the synchronous particle calculated and knowledge of the bore radius

in the DTL, the normalized acceptance of the channel can be found by:

$$\varepsilon_{ch} = \beta\gamma \frac{a^2}{S} \frac{\sin \mu_s}{\left(1 + \sin \frac{\mu_s}{2}\right)} \tag{3.9}$$

The values calculated for normalized channel acceptance are shown in Figure 3.9

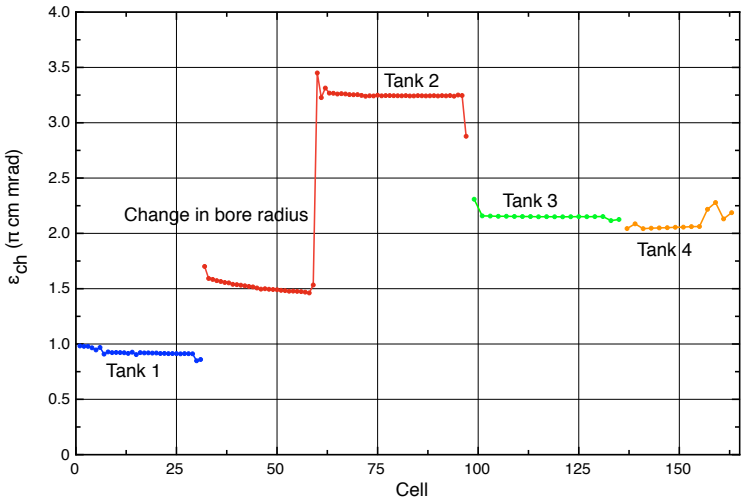

Figure 3.9: Transverse normalized acceptance of the LANSCE DTL.

To find the maximum and minimum of the beta function the following equations were used:

$$\beta_{max} = \frac{S\left(1 + \sin \frac{\mu_s}{2}\right)}{\sin \mu_s} \tag{3.10}$$

$$\beta_{max} = \frac{S\left(1 - \sin \frac{\mu_s}{2}\right)}{\sin \mu_s} \tag{3.11}$$

The beta function values were then normalized by equation 3.12 and plotted in fig. 3.10:

$$\beta_{norm} = \frac{\beta_{max/min}}{\beta_z \gamma_z} \tag{3.12}$$

The normalized beta function values along with the emittance measurements can be used to determine the horizontal and vertical beam profiles by:

$$\begin{aligned} R &= \sqrt{\beta\, \ni} = \sqrt{\beta \frac{\varepsilon}{\beta_z \gamma_z}} \\ &= \sqrt{\beta_{norm} \varepsilon} \end{aligned} \tag{3.13}$$

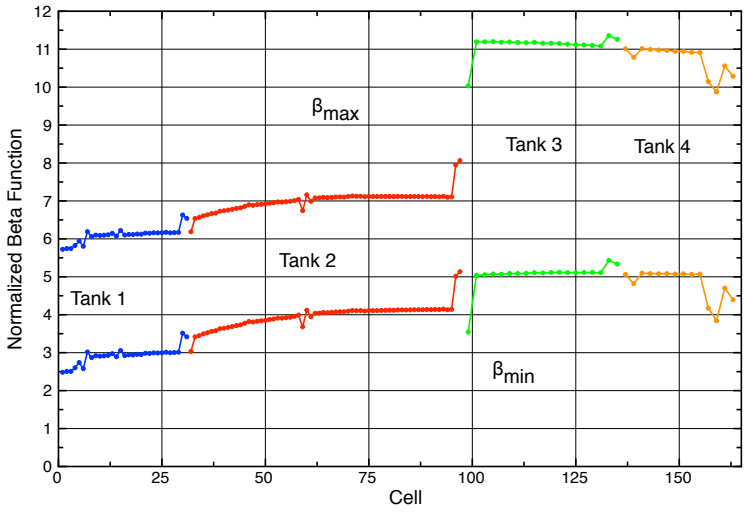

Figure 3.10: Normalized maximum and minimum beta functions of the the LANSCE DTL.

Once all the phase advances have been calculated for the DTL, an area of instability that can be explored is parametric resonance. The regions of parametric resonance calculations and results are shown in the Appendix.

3.2 Drift Tube Linac RF Stability

The Drift Tube Linac longitudinal tune is established by taking the phase scans of each tank and matching the beam bunch to the designed separatrix (see fig. 3.11). The full width half maximum (FWHM) measures the length of the longitudinal separatrix. The distance left of center (DCLE) parameter measures the relative center of the RF separatrix with relationship to another RF separatrix in a different DTL module. For DCLE, DTL module 1 phase is held constant and all other tanks adjusted from that reference point. Empirical tuning has found the correct operating points for each tank so that beam is accelerated properly, with minimal losses. The tank phase and amplitude set-point are determined from the phase scan data. The slope of the intensity for each phase setting indicates the quality of the beam bunching. A shallow slope is caused by gradual capture of a wide beam by the ideal separatrix curve (line B in fig. 3.11). Once the set-point for phase and amplitude are established, the recently installed digital low-level RF system maintains those set-points during operation.

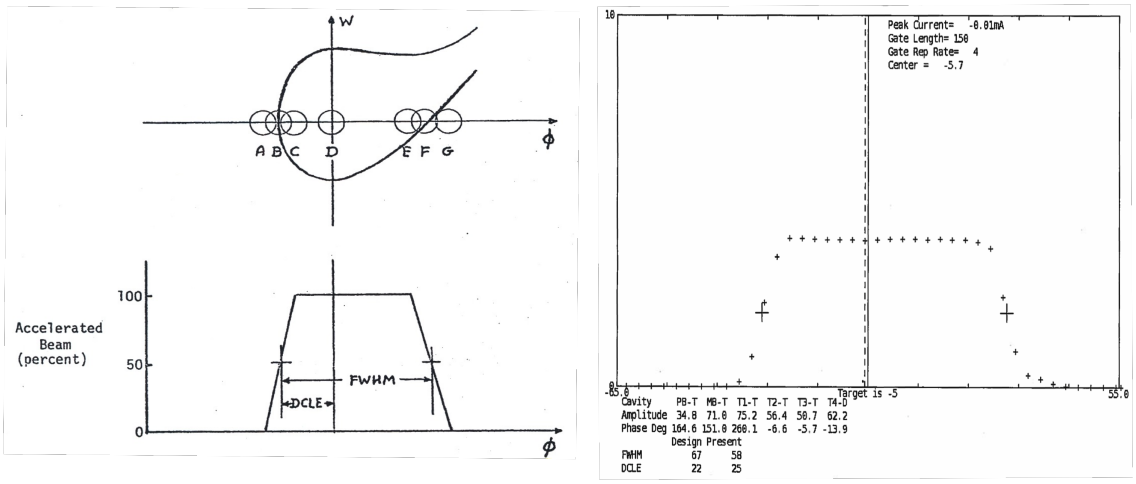

Figure 3.11: DTL phase scan theory and measurement example [24].

After the initial tune of the DTL, operators adjust the DTL modules' phase and amplitudes to minimize losses while in production beam delivery. Because of this optimization the DTL modules set-ups differ from their designed values. Table 3.1 shows the results from phase scan measurements performed at the end of a production run cycle. The year-to-year changes demonstrate the evolution of the DTL tune from beam loss minimization.

Table 3.1: Evolution of DTL set-points at the end of a production run cycle.

	Tank 1		Tank 2		Tank 3		Tank 4	
	FWHM	DCLE	FWHM	DCLE	FWHM	DCLE	FWHM	DCLE
Design	96	34	69	26	67	22	98	46
2016	-	-	-	-	58	25	-	-
2015	97	50	-	-	58	25	108	46
2014	-	-	-	-	-	-	100	36
2013	104	49	79	28	66	19	98	45

The LANSCE accelerator facility has designated a Fast Protect machine protection system, which operates with a response time of approximately 10 μsec [14]. The DTL tank fields provide an input into the fast protect system to turn the beam off if the amplitude cavity field error exceeds $\pm$ 1 % or if the phase cavity field error exceeds $\pm$ 1 °. There is no automatic machine protection if the cavity field drifts away from its optimal set-point or from instantaneous step-changes in the cavity field.

Various amplitude and phase instabilities of the electric field lead to perturbations of the longi-

tudinal oscillations that cause the oscillation amplitude of the phase and momentum of the particles to increase [15]. This can lead to non-trivial effects in the beam, which result in a large energy spread of the beam and higher beam losses. Studies have shown that beam spill in the LANSCE switchyard region is extremely sensitive to the DTL cavity field [17]. AP readings are used as an input to the Fast Protect machine protection system. If the AP reading exceeds 80%, beam delivery will be terminated at the ground level deflector located in the LEBT.

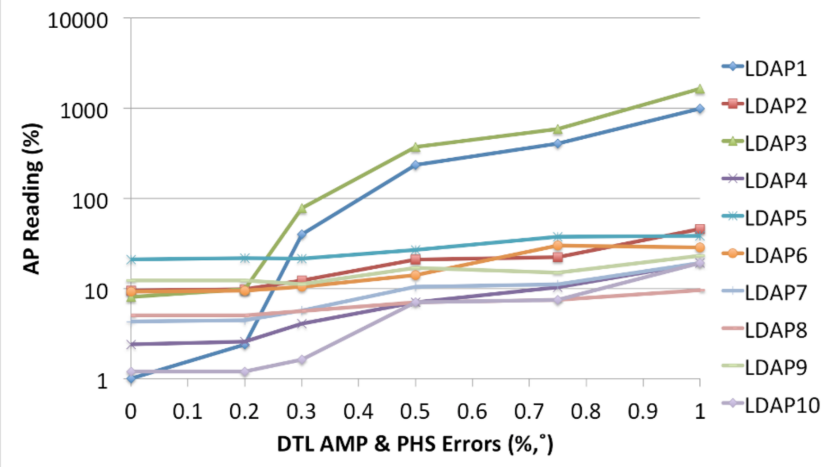

Figure 3.12: Measured beam spill in the LANSCE switchyard as a function of DTL cavity field error [17].

The goal of the DTL RF stability studies was to identify the problems associated with the DTL systems that causes significant problems with tune recovery and beam losses. The first data collected was in steady state normal operations, where the cavity field for all the DTL tanks were monitored in correlation with beam loss monitors in the switchyard. Figure's 3.13 and 3.14 show examples of beam losses and DTL cavity field instabilities during production beam delivery.

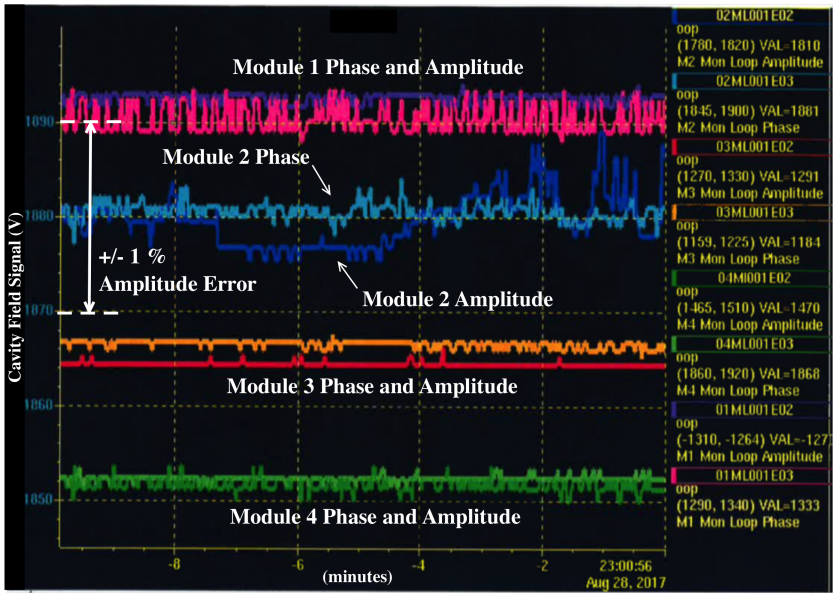

Figure 3.13: Example of instabilities in Module 2 amplitude cavity field during production beam operations.

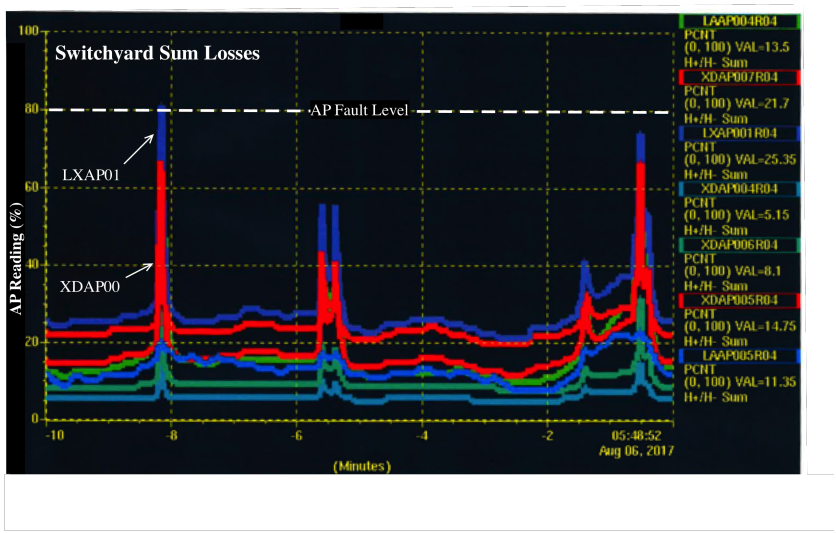

Figure 3.14: Example of switchyard sum beam losses due to instabilities in the DTL RF cavity fields.

Instantaneous changes in DTL cavity field and amplitude were also observed. Figure 3.15 shows a step-change in module 3's cavity field amplitude and phase. Also note that module 4's cavity field phase also performs a step-change at the same time as module 3. The module 4 phenomenon was due to coupling between the module 3 and module 4 LLRF systems. We can see this coupling again in fig. 3.16 where module 3 was cycled on and off for the tune recovery while monitoring module 4's

cavity fields.

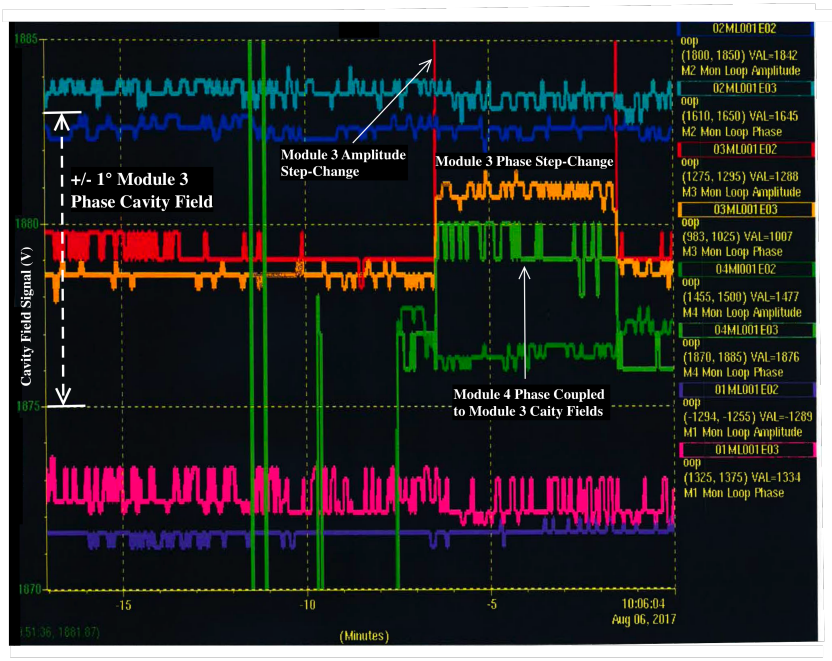

Figure 3.15: Instantaneous change in DTL module 3 cavity field amplitude and phase.

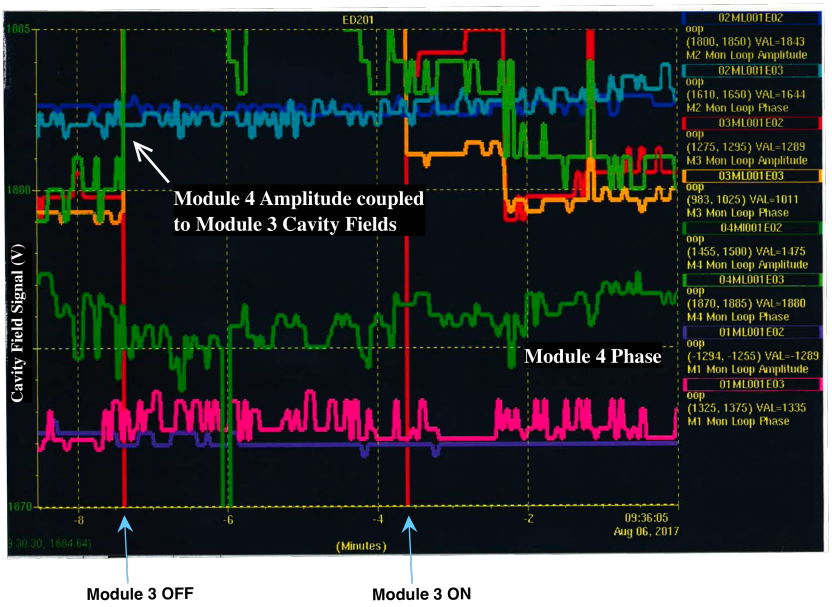

Figure 3.16: Coupling between DTL module 3's LLRF system and Module 4's cavity field phase.

The instantaneous change in the cavity fields of DTL module's 3 and 4 resulted in beam losses that prevented production beam delivery. Figure 3.17 shows the effect of a DTL module step-change

on the rastered IPF beam. Shifts in the IPF rastered beam could cause damage to the target stack or beam window separating the target stack from the IPF beam line. These beam effects showed that the cavity field changes were erroneous data collection or read-back systems faults, but that the cavity fields of the DTL modules were changing.

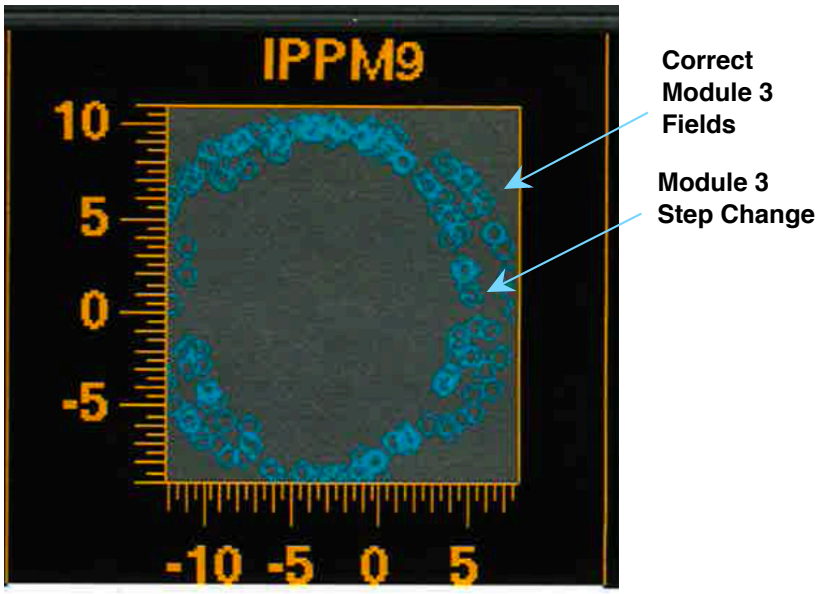

Figure 3.17: Shift of IPF rastered beam due to instantaneous change in module 3's cavity field.

The source of the instantaneous cavity field changes and the coupling between DTL modules was suspected to be an artifact of the new digital LLRF system. The LLRF team was able capture several step-change events and analyze for possible causes [18]. Figure 3.18 shows a captured cavity field step-change event for module 3. From this we also see that the FPGA digital low level RF controller believes that it is maintaining the desired set-points. Step-change events were recorded in both DTL module 3 and module 4 independently.

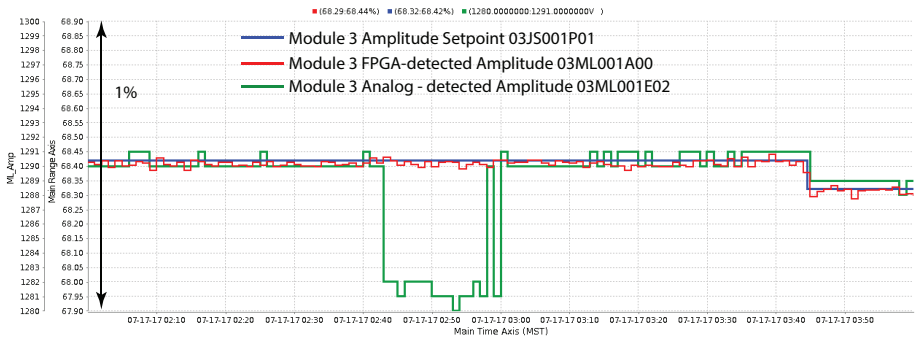

(a) Module 3 amplitude cavity field step-change

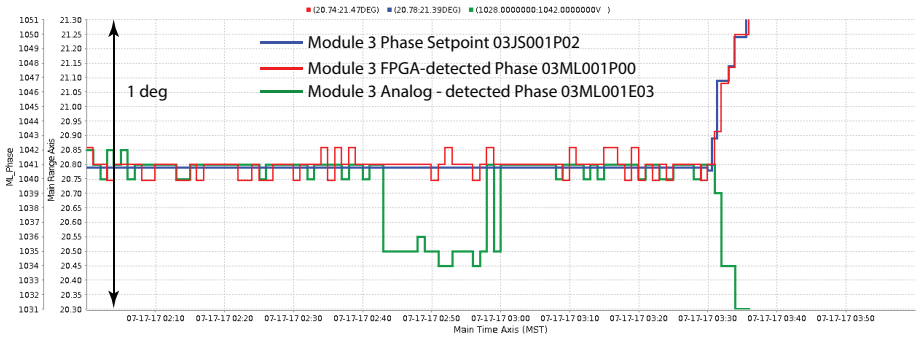

(b) Module 3 phase cavity field step-change

Figure 3.18: Module 3 RF step-change event and digital LLRF system response [18].

The module cavity field set-points being maintained while the measured fields changed means that the associated tune lurches are caused by a signal disturbance [18]. The possible location of the signal disturbance in the digital LLRF system is shown in the highlighted region of fig. 3.19.

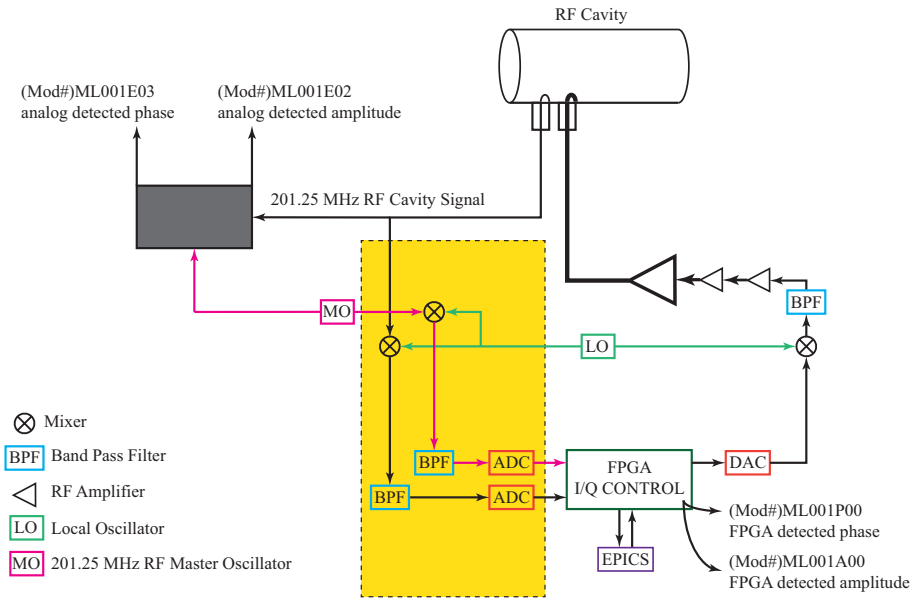

Figure 3.19: DTL digital LLRF system set-up and possible location of signal disturbances [18].

While monitoring one of the step-change events in module 3, it was noted that the RF reference had a slow drifting phase. Figure 3.20 shows that the digital LLRF system can maintain the cavity field consistent with the slow drift of the RF reference source.

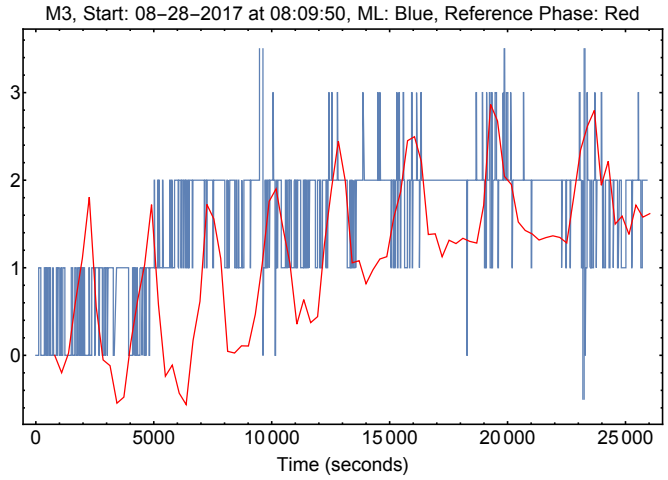

Figure 3.20: Module 3 cavity field maintained with the slow drift of the RF reference phase [18].

During the step-change event, the RF reference experience a jump in slope of the slow drift of approximately 0.13 $\frac{mdeg}{sec}$ as shown in fig. 3.21.

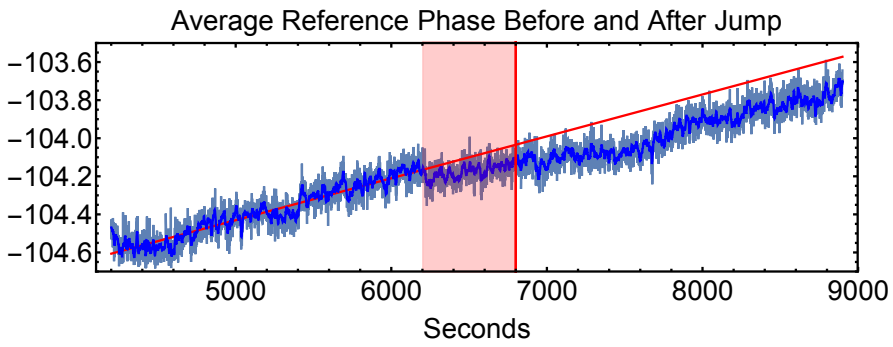

(a) RF reference phase during module 3 step-change. Highlighted area is approximately when the event occurred and the red line is when the lurch was detected by the analog pickups.

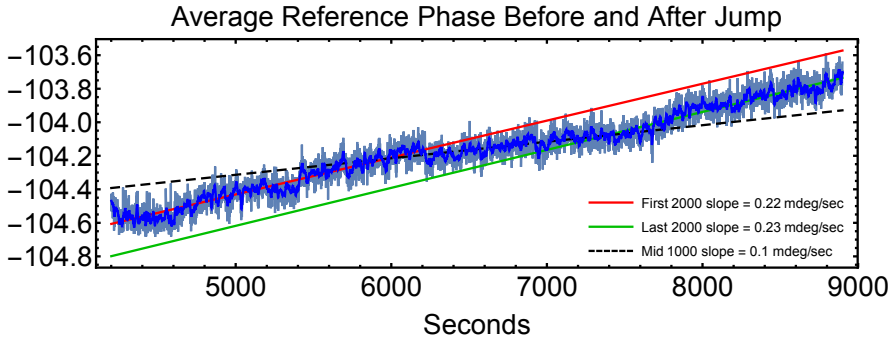

(b) Slope changes of the reference phase before, during, and after a module 3 step-change event.

Figure 3.21: RF reference phase behavior during module 3 step-change event [18].

If we zoom in on the reference phase during the event and overlay it with the cavity field channels, we see a lurch in module 4 that occurred with no changing of the phase or amplitude set-points (see fig. 3.22). This lurch occurred when there was a sudden change in the RF reference phase.

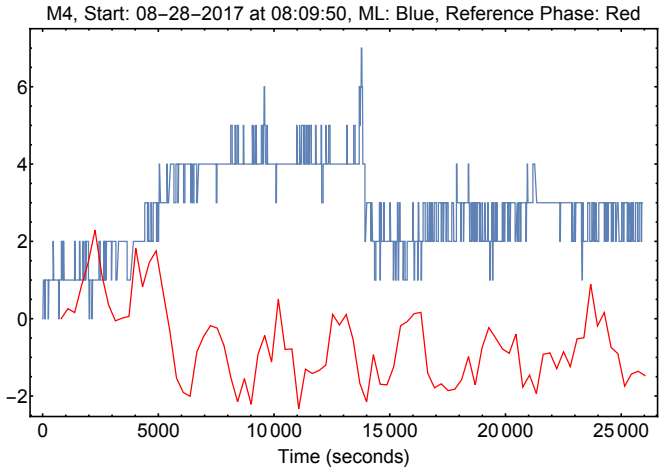

Figure 3.22: Module 4 cavity field change during a sudden change in the reference phase drift [18].

The initial study concludes that the cavity field step-change and drifting events are caused by changes of the sudden changes in the reference signal. Changes in the reference phase would change the perceived I and Q values of the cavity fields and also the amplitudes due to the documented phase-to-amplitude dependence in the digital LLRF system [18]. Coupling between modules was removed by shielding the signal cables associated with each module from each other. Maintenance was performed on the RF reference system to mitigate the sudden changes in the RF reference signal. Observations during the 2018 production cycle have shown better stability in the DTL RF system. Results from DTL cavity field monitoring from 2018 are shown in Figure 3.23.

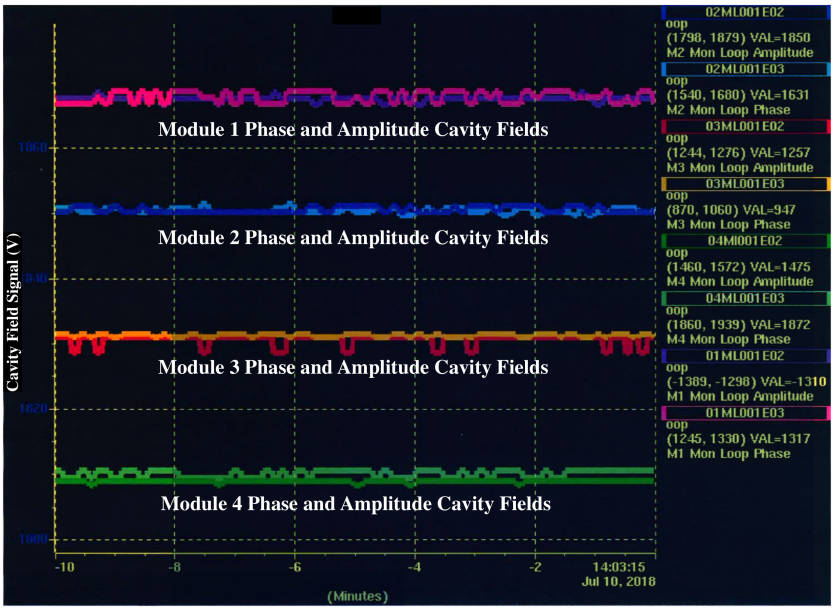

Figure 3.23: DTL cavity fields after repairs to the RF reference source.

Chapter 4

805 MHz Side Coupled Cavity Linear Accelerator

4.1 Side-Coupled Cavity Linear (SCL) Accelerator Beam Dynamics

The side-coupled cavity linear accelerator at LANSCE accelerates beam from 100 MeV to 800 MeV. It consists of 44 RF modules with two different module layouts and a FDO focusing structure (see fig. 1.9). For the development of future accelerator simulations to study beam stability and beam tunes, the basic beam dynamics of the LANSCE side-coupled cavity linear accelerator were calculated. The historical magnet settings and cavity fields were used to calculate the transverse and longitudinal parameters of the SCL.

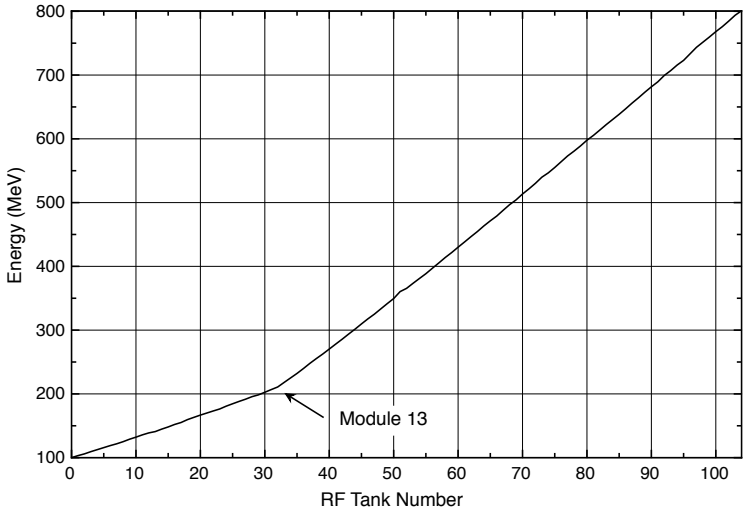

Figure 4.1: Profile of energy gained in the LANSCE SCL.

Effective phase advance of transverse oscillations of the beam in an RF field μ_s is determined by the focusing structure and by the phase advance of longitudinal oscillations. We first derive an expression for the longitudinal phase advance in an RF tank and a drift space. We start with the transfer matrix for longitudinal motion within an RF tank:

$$\begin{bmatrix} \cos\mu_{0\ell} & \frac{\sin\mu_{0\ell}}{m\gamma^3\Omega} \\ -m\Omega\gamma^3\sin\mu_{0\ell} & \cos\mu_{0\ell} \end{bmatrix} \tag{4.1}$$

The transfer matrix of longitudinal motion in a drift space is:

$$\begin{bmatrix} 1 & \frac{\ell}{m\gamma^3\beta c} \\ 0 & 1 \end{bmatrix} \tag{4.2}$$

Combining the two equations to find the transfer matrix in a RF tank and a drift space, we find:

$$\begin{bmatrix} \cos\mu_{0\ell} & \cos\mu_{0\ell}\left(\frac{\ell}{m\gamma^3\beta c}\right) + \frac{\sin\mu_{0\ell}}{m\gamma^3\Omega} \\ -m\Omega\gamma^3\sin\mu_{0\ell} & -m\Omega\gamma^3\sin\mu_{0\ell}\left(\frac{\ell}{m\gamma^3\beta c}\right) + \cos\mu_{0\ell} \end{bmatrix} \tag{4.3}$$

Utilizing the relationship from equation 4.4,

$$\cos\mu_0 = \frac{M_{11} + M_{22}}{2} \tag{4.4}$$

we can rewrite the expression in terms of the dimensionless frequency $\frac{\Omega}{\omega}$ and come to the expression:

$$\cos\left(\mu_{0\ell}\right)_f = \cos\left(\mu_{0\ell}\right)_0 - \frac{\Omega\ell\pi}{\omega\beta\lambda}\sin\left(\mu_{0\ell}\right)_0 \tag{4.5}$$

The term ℓ is the difference between the period S and the RF tank length L. The initial $\mu_{0\ell}$ without the drift space taken into consideration is found by:

$$\mu_{0\ell} = 2\pi\frac{L}{\beta\gamma}\frac{\Omega}{\omega} \tag{4.6}$$

where L is the length of the RF tank and $\frac{\Omega}{\omega}$ is the dimensionless frequency for longitudinal oscillations. The analytical solution derived gives a value for longitudinal phase advance for Tank 1 in Module 5 equal to 69.6°. When the value for longitudinal phase advance is solved directly from the transfer matrix, we arrived at a value equal to 70.0°.

The FDO set-up used in the derivation and calculation of transverse beam parameters is shown in fig. 4.2.

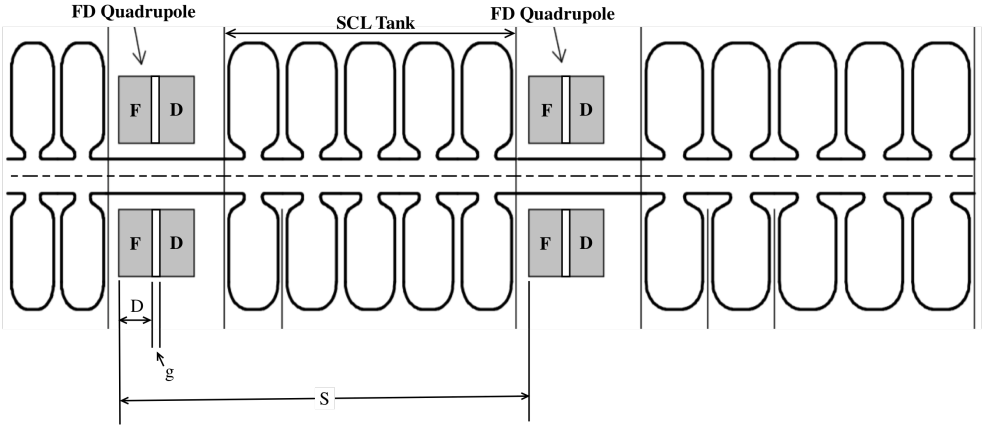

Figure 4.2: The LANSCE side-coupled cavity linac FDO focusing structure [16].

For the transverse phase advance per FDO period, we derived an equation for the FDO lattice that is used in the SCL. We start by finding the transfer matrix of the FDO lattice by:

$$M = M_F M_g M_D M_O \tag{4.7}$$

where:

$$
\begin{aligned}
M_F &= \begin{bmatrix} \cos D\sqrt{k} & \frac{1}{\sqrt{k}} \sin D\sqrt{k} \\ -\sqrt{k} \sin D\sqrt{k} & \cos D\sqrt{k} \end{bmatrix} \\
M_D &= \begin{bmatrix} \cosh D\sqrt{k} & \frac{1}{\sqrt{k}} \sinh D\sqrt{k} \\ -\sqrt{k} \sinh D\sqrt{k} & \cosh D\sqrt{k} \end{bmatrix} \\
M_O &= \begin{bmatrix} 1 & \ell \\ 0 & 1 \end{bmatrix} \\
M_g &= \begin{bmatrix} 1 & g \\ 0 & 1 \end{bmatrix}
\end{aligned}
\tag{4.8}
$$

The drift length is defined by ℓ while the length between the focusing and defocusing quadrupoles is defined by g. We let $\chi = D\sqrt{k} = D\sqrt{\frac{qG}{mc\beta\gamma}}$ and use the smooth approximations of $\cosh\chi = 1 + \frac{\chi^2}{2} + \frac{\chi^4}{24}$, $\sinh\chi = \chi + \frac{\chi^3}{6} + \frac{\chi^5}{120}$, $\cos\chi = 1 - \frac{\chi^2}{2} + \frac{\chi^4}{24}$, and $\sin\chi = \chi - \frac{\chi^3}{6} + \frac{\chi^5}{120}$. To solve for transverse phase advance after the transfer matrix is solved for, we utilize the relationship in equation 4.4. Finally, the equation derived for transverse phase advance per FDO period is:

$$
\mu_0 = \frac{qG_0}{mc\beta\gamma} \sqrt{\frac{2}{3} D^3 S \left(1 - \frac{2D}{S} - \frac{g}{S}\right)\left(1 + \frac{3g}{2D}\right)}
\tag{4.9}
$$

The smooth approximation solution was compared with calculations found directly from the transfer matrix (see Figure 4.3). The smooth approximation is valid for $\mu_0 \leq 60°$.

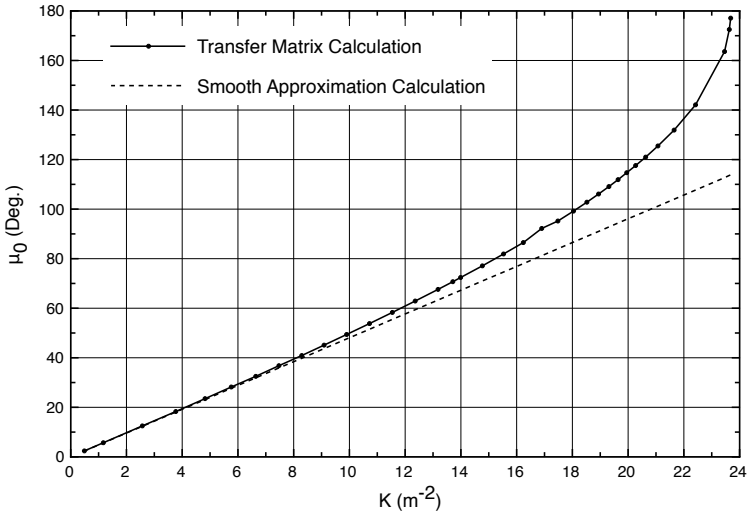

Figure 4.3: Transverse phase advance calculation comparison.

Utilizing equation 3.8, we can find the effective phase advance of the beam in an RF field.

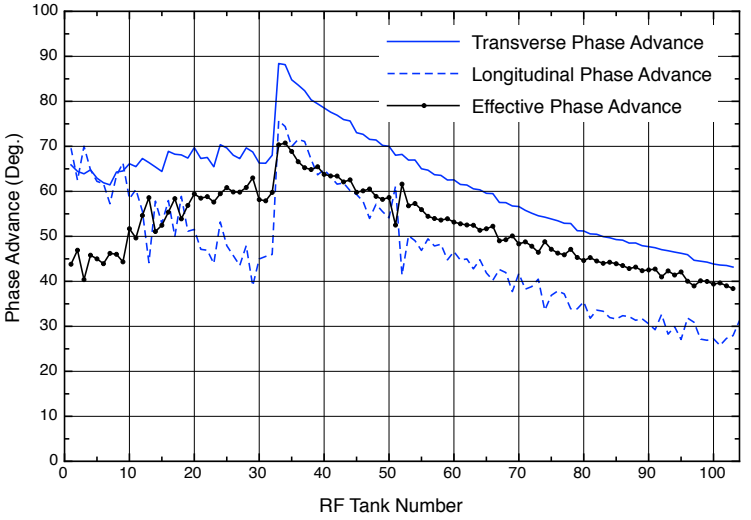

Figure 4.4: LANSCE SCL phase advances per focusing period.

As noted above in fig. 4.3, the smooth approximation is not valid for phase advances $\geq 60°$. The results are shown in fig. 4.5 that compare the results for the effective phase advance in an RF field for the smooth approximation and from that determined directly from the transfer matrices.

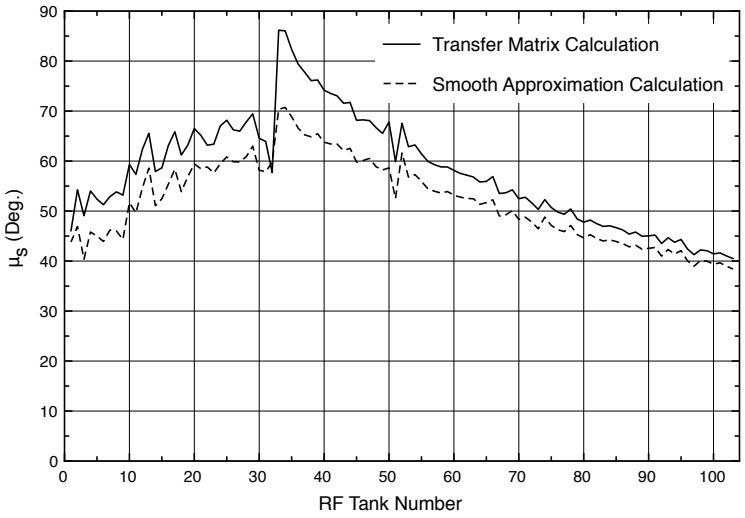

Figure 4.5: Comparison of the effective phase advance in an RF field calculations.

The maximum and minimum Twiss beta functions were determined from the following equations:

$$\begin{aligned} \beta_{max} &= \frac{S\,(1+f_1) - (2D+g)\,f_1}{\sin\mu_0} \\ \beta_{max} &= \frac{S\,(1-f_2) + (2D+g)\,f_2}{\sin\mu_0} \end{aligned} \tag{4.10}$$

where:

$$\begin{aligned} f_1 &= kD^2 + gkD - \frac{1}{3}gk^2D^3 \\ f_2 &= kD^2 + gkD + \frac{1}{3}gk^2D^3 \end{aligned} \tag{4.11}$$

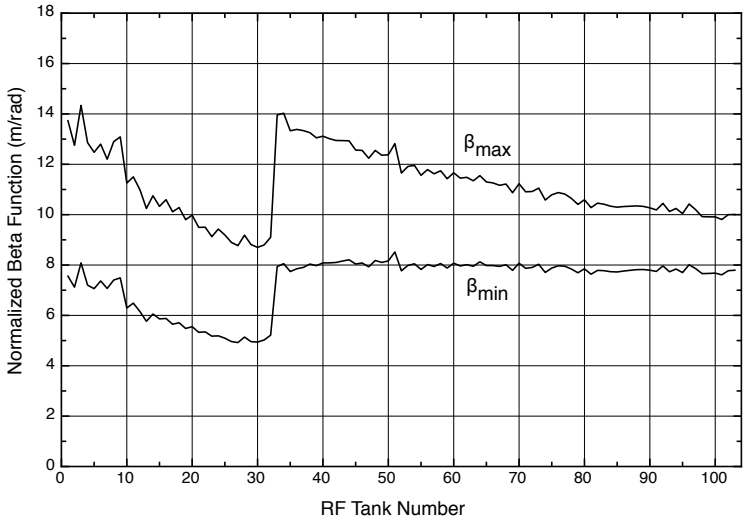

Figure 4.6: LANSCE SCL normalized Twiss beta functions.

Normalized transverse and longitudinal acceptance were determined by using equations 3.9 and 3.6.

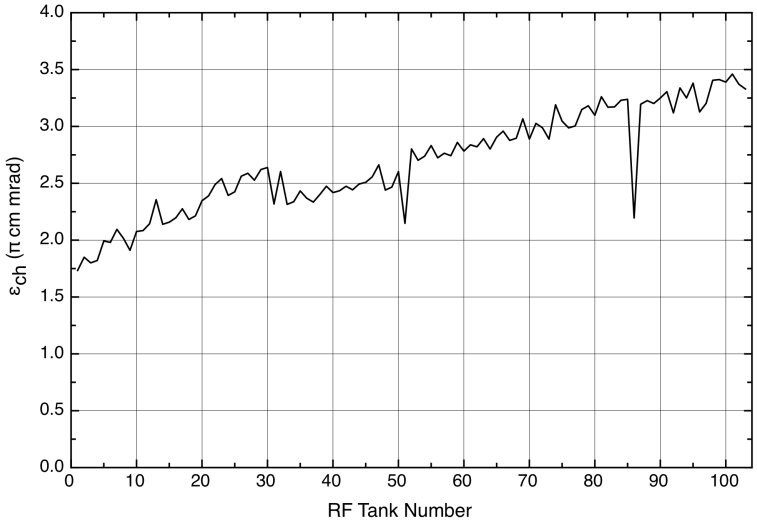

Figure 4.7: LANSCE SCL normalized transverse acceptance.

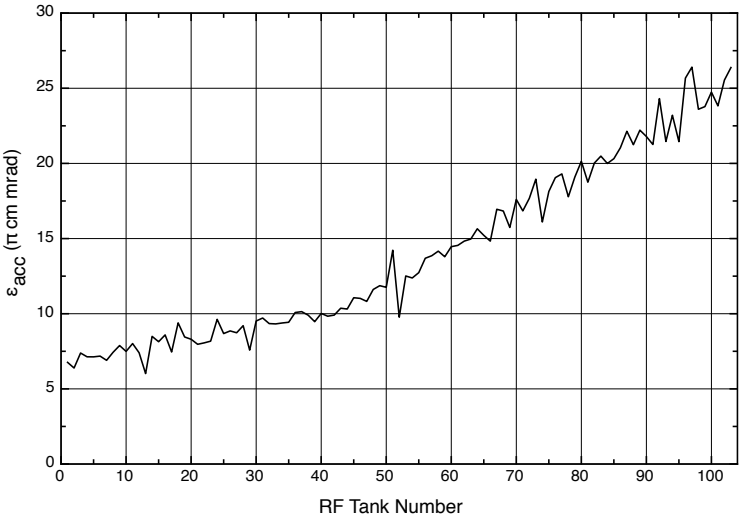

Figure 4.8: LANSCE SCL longitudinal acceptance

4.2 Paticle-In-Cell Simulations of the LANSCE SCL

A recent effort has been made to improve the simulation capabilities of the LANSCE accelerator facility. The 805-MHz side-coupled cavity linac (SCL) section of the facility was simulated with the BEAMPATH code. BEAMPATH is a particle-in-cell code that was developed as a tool for studying beam dynamics with space charge in linear accelerators [22].

The architecture of the SCL was built from the past TRACE 2D set-up files (ST805). Manual measurement of the beamline component locations was completed to ensure the TRACE file accuracy. Each RF tank was simulated as one long RF cavity. Figure 4.9 shows the SCL architecture as built in BEAMPATH.

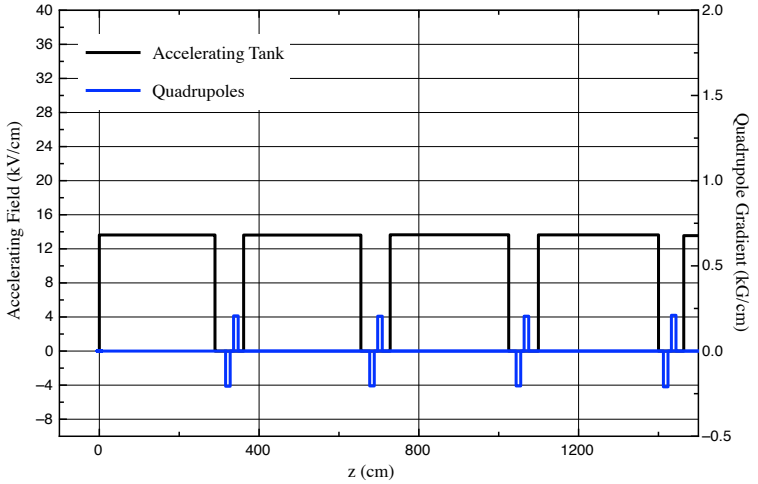

Figure 4.9: SCL BEAMPATH simulation set-up for Module 5.

The accelerating fields for the RF tanks was determined from two different sources. The original design fields were acquired from the original design documentation from 1967 [**?**]. The second source of accelerating field data was taken from the TRACE ST805 file. The TRACE ST805 field values were determined from a bead pull measurement performed in 1979 [25]. Figure 4.10 shows a comparison of the original design field and that of the TRACE fields.

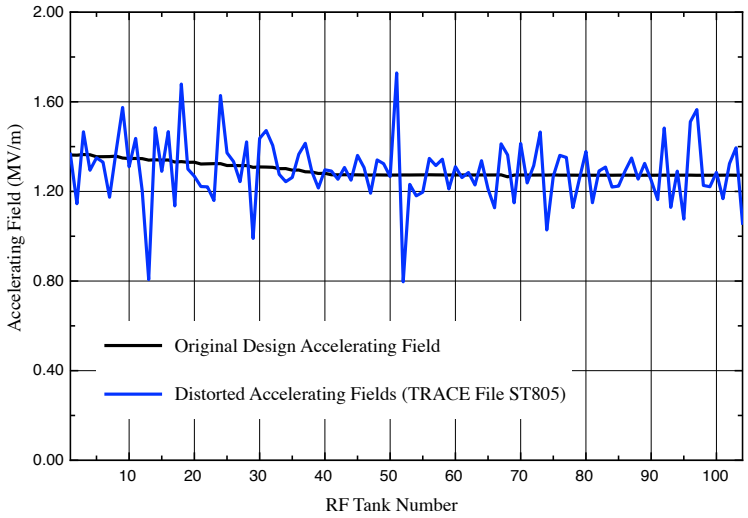

Figure 4.10: Accelerating Fields of the LANSCE SCL used in BEAMPATH simulations.

Prior to starting simulations, the correct number of integration steps had to be determined. The numerical solution found by the integrator depends on the arbitrary value of the integration step and is not equivalent to the exact solution of the differential equations of motion [22]. Therefore if

we want the simulation to maintain the properties as close to the real system as possible, several tests were necessary, with the different integration steps shown in Table 1. These tests allowed us to determine the integration step value to be 360 for the simulations.

Table 4.1: Transverse emittance growth due to integration step size

Integration Steps per RF Period	Initial ε_x ($\pi\, cm\, mrad$)	Final ε_x ($\pi\, cm\, mrad$)	Emittance Growth Factor
72	0.18	0.85	4.72
180	0.18	0.25	1.39
360	0.18	0.20	1.11
720	0.18	0.20	1.11

LBEG simulations were performed with a beam current of $I_{beam} = 10\, mA$. MPEG has approximately 2.5 times the space charge as LBEG therefore the average beam current for MPEG simulations was $I_{beam} = 25\, mA$. Both beams were simulated using the ideal accelerating fields and the TRACE accelerating fields. Figure 4.11 shows the beam envelopes of the SCL using LBEG, beam and the ideal accelerating fields. Figure 4.12 shows an example of the beam envelopes from the TRACE code.

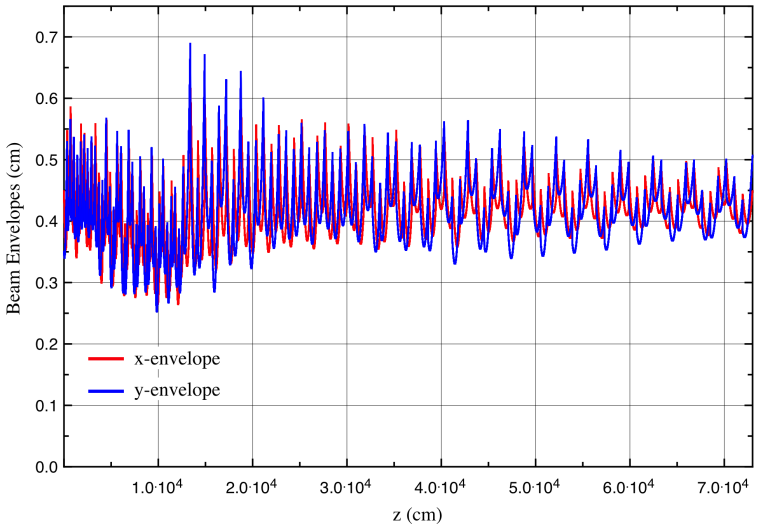

Figure 4.11: LANSCE SCL LBEG beam envelopes from BEAMPATH simulations.

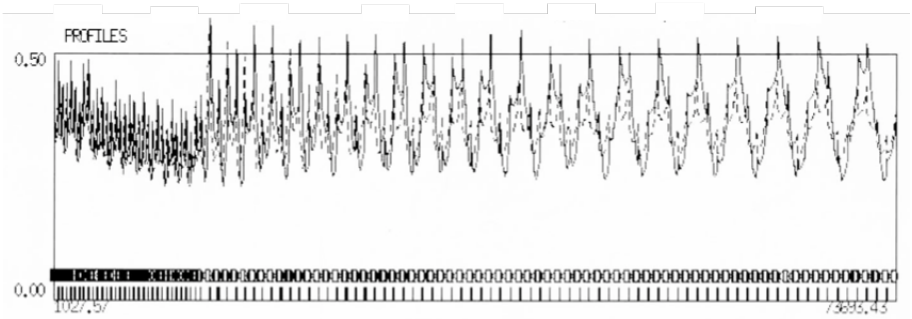

Figure 4.12: Example of LANSCE SCL beam envelopes from TRACE code.

One advantage of BEAMPATH is its ability to simulate the different space charge conditions that arise at a multi-beam facility. In BEAMPATH, the space charge field is renewed at every elementary integration step using Poisson's equation in the moving frame [22]. Figure 4.4 and 4.5 show the initial space charge fields on MPEG and LBEG simulations in the transverse and longitudinal planes.

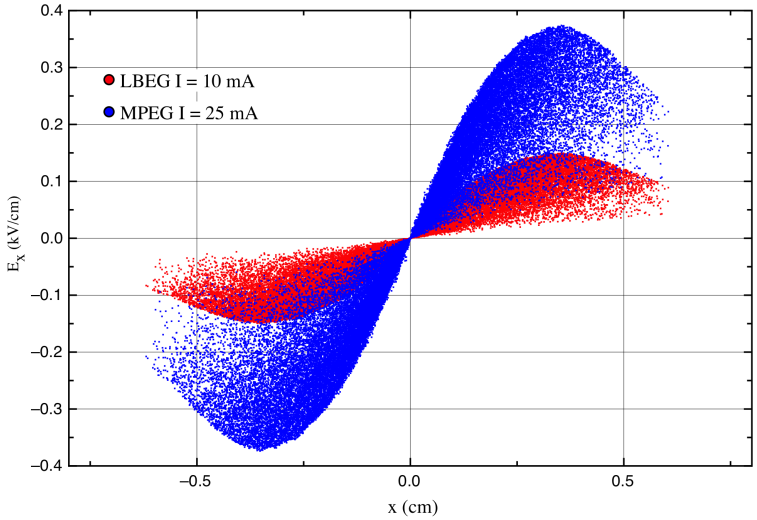

Figure 4.13: Initial transverse space charge field for MPEG and LBEG beams.

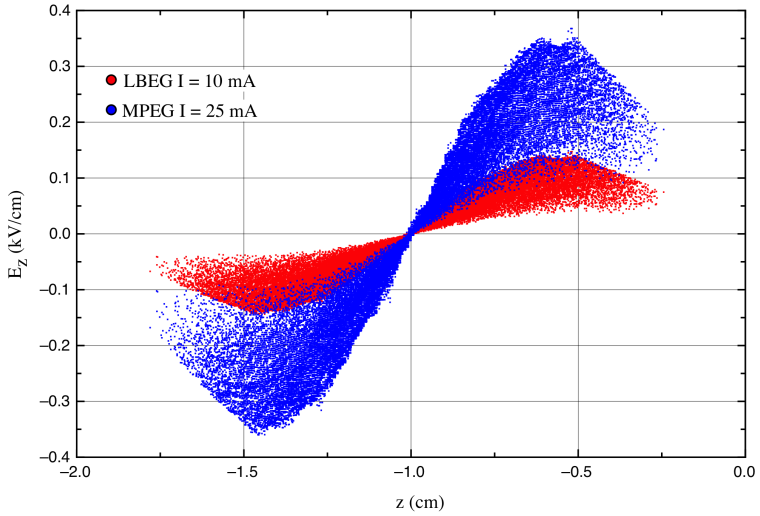

Figure 4.14: Initial longitudinal space charge field for MPEG and LBEG beams.

BEAMPATH also allows for the tracking of single particles within the simulation. Utilizing this feature, we can see the effective phase advance per period in the RF field and compare the different beams. Figure 4.15 shows the results of a single particle trajectory at three different beam currents. For the case where $I_{beam} = 0\,mA$, we can manually calculate what the phase advance is and compare that to the phase advance values obtained from the TRACE 2D matrices. At RF tank 7, the effective phase advance in an RF field was given by TRACE 2D to be $\mu_s = 52.89°$ and in BEAMPATH as $\mu_s = 51.43°$. When space charge forces are not negligible, transverse oscillation frequency decreases (see fig. 4.15).

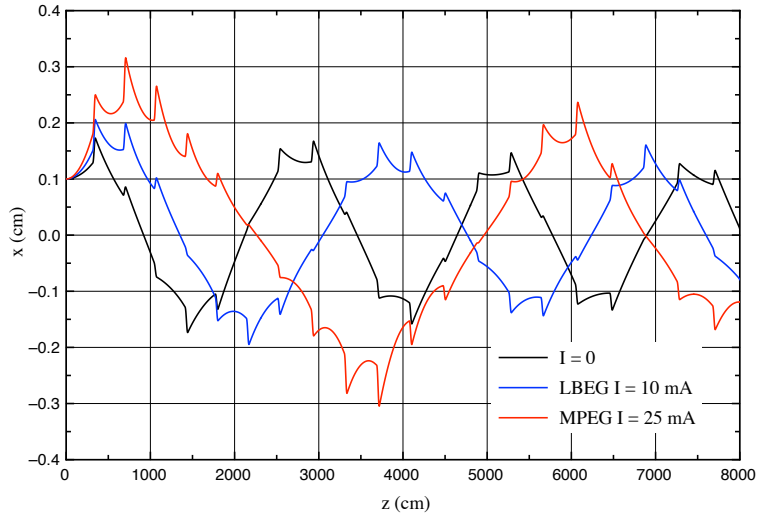

Figure 4.15: Effective phase advance in an RF field for different beam currents.

4.3 Emittance Growth Studies Using BEAMPATH

The LANSCE accelerator facility suffers from considerable emittance growth and beam tail formation. Measured LBEG horizontal and vertical emittance growth through the LANSCE accelerator section are shown in Table 4.2. The BEAMPATH particle-in-cell code was chosen to perform studies on different known mechanisms for emittance growth.

Table 4.2: Measured normalized RMS emittance growth in the LANSCE linear accelerator.

Production Year	Entrance to DTL ($\pi\, cm\, mrad$)		Entrance to SCL ($\pi\, cm\, mrad$)		End of SCL ($\pi\, cm\, mrad$)		Emittance Growth Factor	
	ε_x	ε_y	ε_x	ε_y	ε_x	ε_y	ε_x	ε_y
2017	0.017	0.026	0.037	0.036	0.071	0.059	4.17	2.27
2016	0.018	0.022	0.050	0.026	0.0899	0.0713	4.99	3.24
2015	0.020	0.026	0.030	0.024	0.070	0.059	3.50	2.27
2014	0.021	0.027	0.040	0.039	0.093	0.10	4.42	3.70

Emittance growth studies were performed by starting at the ideal accelerating structure and changing various parameters to understand its contribution to the total emittance growth. Longitudinal bunch length, space charge forces, and accelerating fields were varied to study effect of beam emittance growth.

The average value for longitudinal bunch length measure at the beginning of the SCL is 25° (see Figure 4.16). The results show that there is minimal effect on the transverse emittance growth due to initial longitudinal bunch length. To study bunch length and the transverse-longitudinal coupling effect on emittance growth, simulations were performed with initial longitudinal bunch lengths of 0° and 25°.

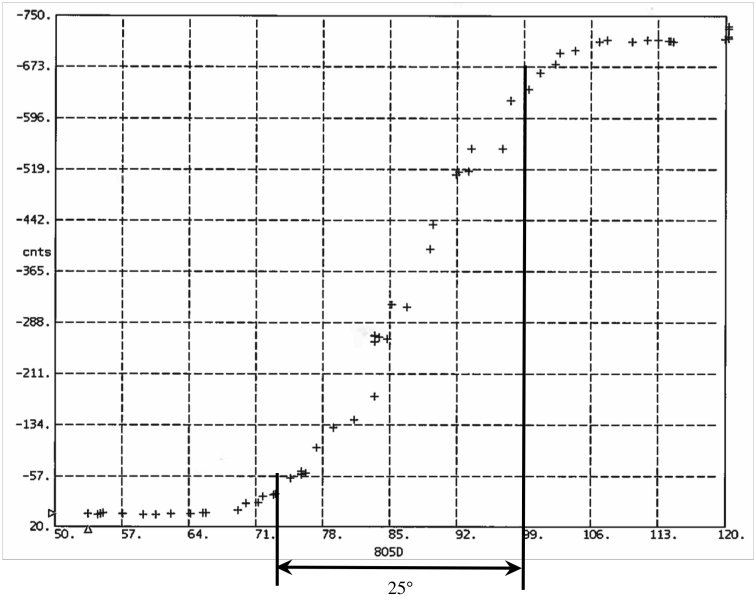

Figure 4.16: LBEG Longitudinal phase width measured at the entrance to the LANSCE SCL.

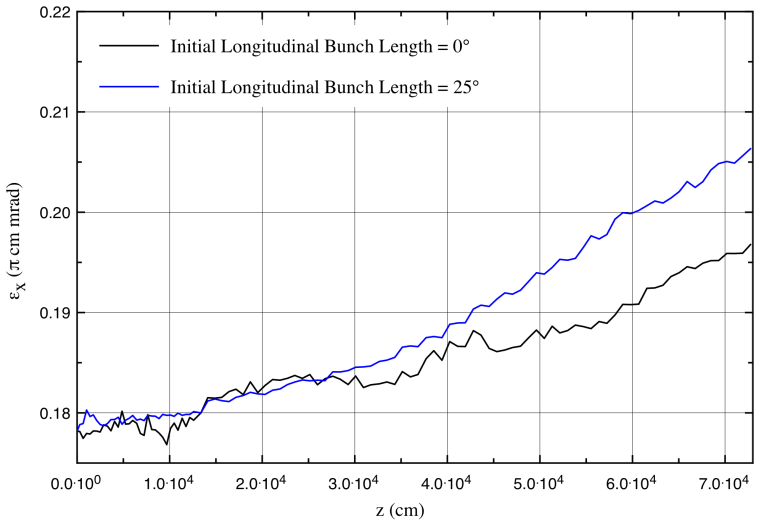

Figure 4.17: Transverse normalized 4 RMS emittance growth with different initial longitudinal bunch lengths.

Table 4.3: Transverse normalized 4 RMS emittance growth due to varying initial longitudinal bunch length simulation results.

Beam Current (mA)	Accelerating Fields	Initial Longitudinal Bunch Length ($Deg.$)	Initial Transverse Emittance ($\pi\, cm\, mrad$)	Final Transverse Emittance ($\pi\, cm\, mrad$)	Emittance Growth Factor
0	Design	0	0.1766	0.197	1.12
0	Design	25	0.1766	0.206	1.17

LANSCE accelerates two H^- beams with significantly different space charge properties. The SCL is usually tuned for LBEG, since it is the higher power beam. However, the MPEG beam has 2.5x as much space charge. For these simulations, all initial conditions were the same. The accelerating fields were the ideal designed fields. Figure 4.18 shows the results of transverse and longitudinal emittance growth due to space charge forces. The results shown in Tables 4.4 and 4.5 show that the space charge force has a large effect on transverse emittance growth while the longitudinal emittance growth is unaffected.

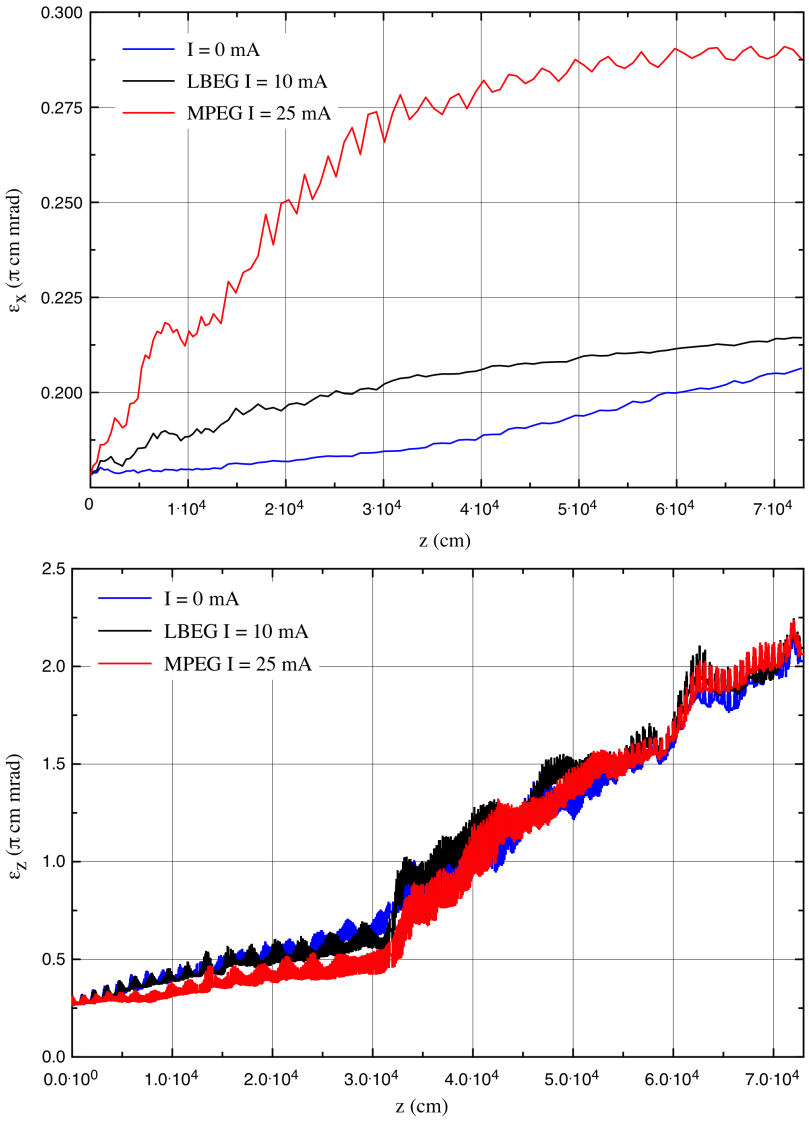

Figure 4.18: Transverse and longitudinal normalized 4 RMS emittance growth due to space charge force.

Table 4.4: Space charge induced transverse normalized 4 RMS emittance growth simulation results.

Beam Current (mA)	Accelerating Fields	Initial Transverse Emittance ($\pi\, cm\, mrad$)	Final Transverse Emittance ($\pi\, cm\, mrad$)	Emittance Growth Factor
0	Design	0.18	0.206	1.14
10	Design	0.18	0.214	1.19
25	Design	0.18	0.290	1.61

Table 4.5: Space charge induced longitudinal normalized 4 RMS emittance growth simulation results.

Beam Current (mA)	Accelerating Fields	Initial Longitudinal Emittance ($\pi\, cm\, mrad$)	Final Longitudinal Emittance ($\pi\, cm\, mrad$)	Emittance Growth Factor
0	Design	0.28	2.03	7.25
10	Design	0.28	2.09	7.46
25	Design	0.28	2.06	7.36

The accelerating fields used in the SCL can vary significantly from the designed values (see fig. 4.10). Simulations were performed with different RF field distributions along the SCL. Figure 4.19 shows the transverse and longitudinal emittance growth due to varying accelerating fields. We see that the accelerating fields have little effect on transverse emittance growth and a significant effect on longitudinal emittance growth.

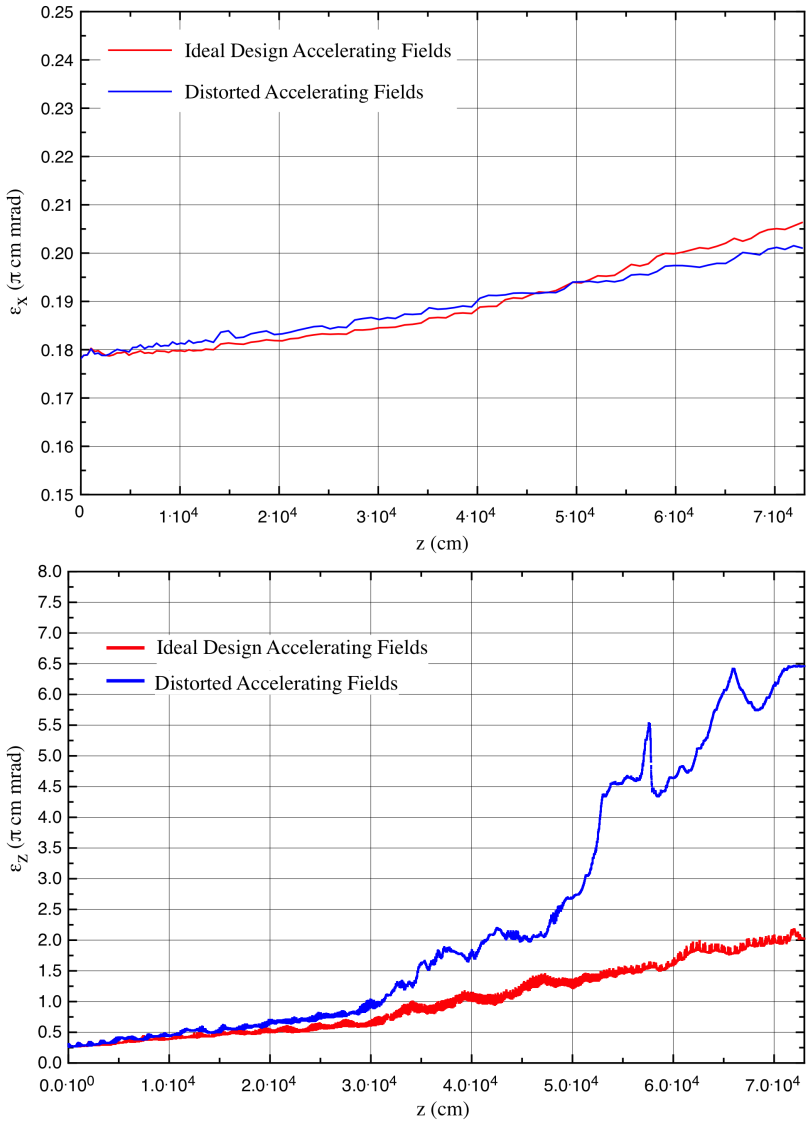

Figure 4.19: Transverse and longitudinal normalized 4 RMS emittance growth due to varying accelerating fields.

Table 4.6: Varying accelerating fields induced transverse normalized 4 RMS emittance growth simulation results.

Beam Current (mA)	Accelerating Fields	Initial Transverse Emittance ($\pi\, cm\, mrad$)	Final Transverse Emittance ($\pi\, cm\, mrad$)	Emittance Growth Factor
0	Design	0.18	0.206	1.14
0	Distorted	0.18	0.202	1.12

Table 4.7: Varying accelerating fields induced longitudinal normalized 4 RMS emittance growth simulation results.

Beam Current (mA)	Accelerating Fields	Initial Longitudinal Emittance ($\pi\, cm\, mrad$)	Final Longitudinal Emittance ($\pi\, cm\, mrad$)	Emittance Growth Factor
0	Design	0.28	2.03	7.25
0	Distorted	0.28	6.46	23.07

The accelerating fields of the system also greatly effect the final momentum spread of the beam. BEAMPATH tracks the energy spread of the beam $\left(\frac{dW}{W}\right)$. We can convert that to the momentum spread of the beam by using eq. 2.1. Figure 4.20 shows the evolution of the energy spread through the BEAMPATH simulations with ideal design fields and the distorted accelerating fields. The final values of momentum spread are shown in Table 4.8.

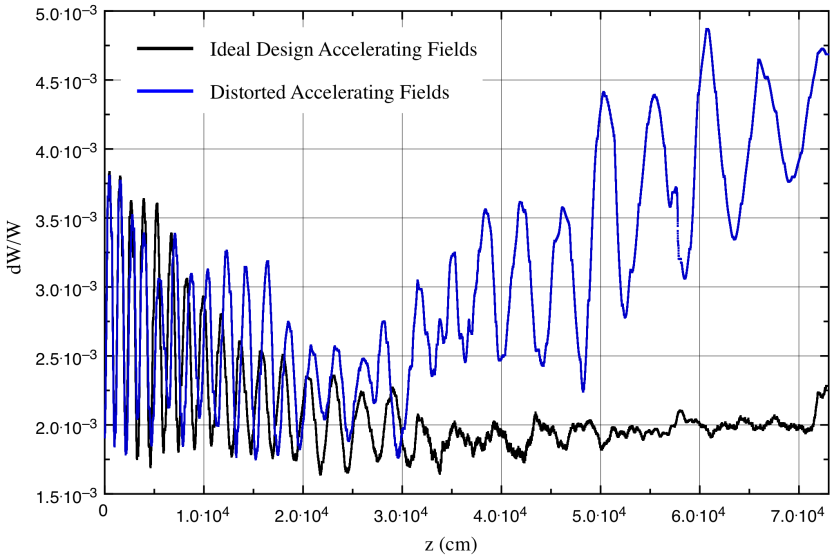

Figure 4.20: Energy spread due to varying accelerating fields.

Table 4.8: Varying accelerating fields induced momentum spread growth simulation results.

Beam Current (mA)	Accelerating Fields	Initial Momentum Spread	Final Momentum Spread	Momentum Spread Growth Factor
0	Design	$1.3 \cdot 10^{-3}$	$1.48 \cdot 10^{-3}$	1.13
0	Distorted	$1.3 \cdot 10^{-3}$	$3.05 \cdot 10^{-3}$	2.35

These three initial studies show the flexibility of BEAMPATH for studying different areas of the LANSCE accelerator. Performed simulations show that the most significant effect on emittance growth is due to RF field variations.

4.4 SCL Transverse Match

During each machine turn-on period beam is matched into the SCL using the design Twiss parameters. Matching of the beam provides the beam ellipses with Twiss parameters, which are supposed to be repeated after each focusing period of the structure. After injection into the SCL, the quadrupoles in the 4 tank modules 5 through 12 are ramped until they reach the constant quadrupole settings in modules 13-48.

Having the proper matching parameters into the SCL and the proper SCL quadrupole settings will ultimately lead to a more stable beam by minimizing beam losses. Experience has shown that without the proper quadrupole settings in the SCL the summed beam losses in the SCL section of the facility will be high. An example of the effect the SCL quadrupole settings have on beam losses is shown in Figure 4.21.

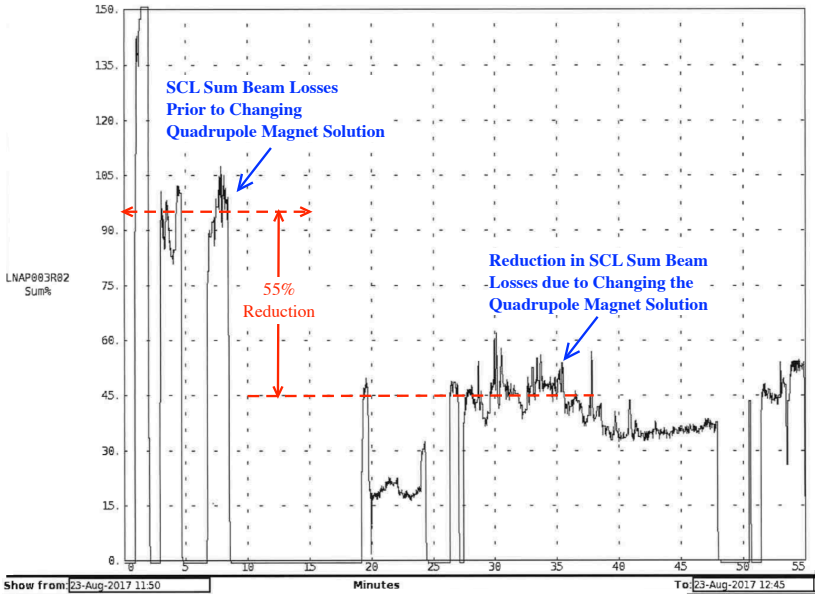

Figure 4.21: Reduction in beam losses due to the SCL quadrupole magnet settings.

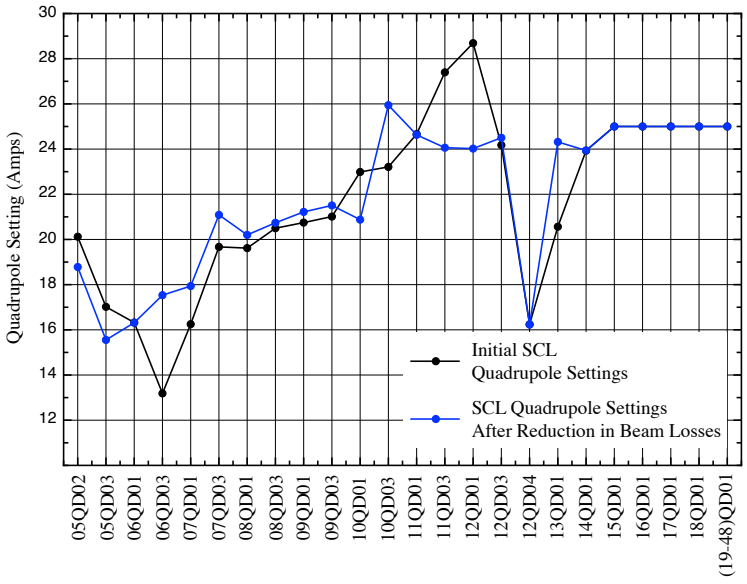

Figure 4.22: SCL Quadrupole magnet settings before and after the reduction in beam losses.

The lattice for the SCL is quasi-periodic. To determine the injection parameters for different initial quadrupole settings, simulations were performed with the Methodical Accelerator Design (MADx) code. Figure 4.23 illustrates the focusing period of the SCL structure of Modules 5-12, which includes accelerating tank and quadrupole doublet.

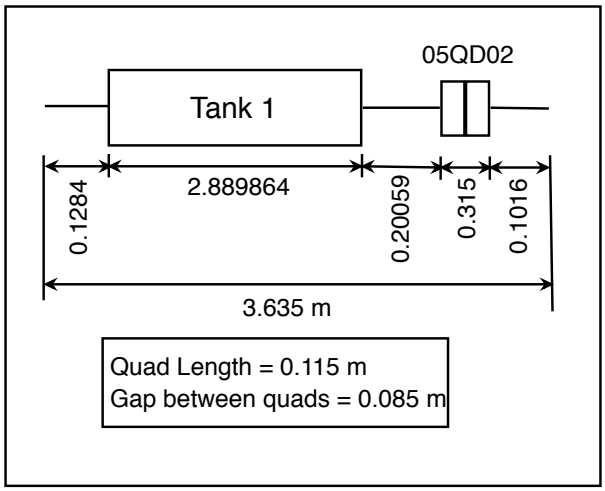

Figure 4.23: Simulation set-up for entry into the LANSCE SCL.

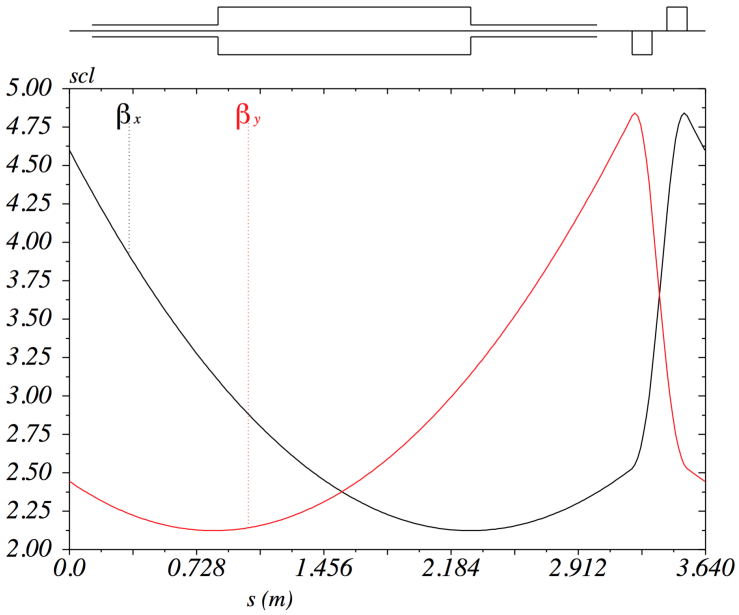

Figure 4.24: Example of MADx matching of the beam at the point of slit position of TREM02, providing periodic beam envelopes.

Simulations were performed with varying initial quadrupole strengths. The historical Twiss parameters used for matching into the SCL are shown in table 4.9. The simulation results are shown

in Table 4.10. The production quadrupole magnet (05QD02) set-point when these simulations were performed was 17.5 Amps. It is noted from the tables below that the production magnet value gives matching parameters that are near the historical matching parameters.

Table 4.9: Historical matching parameters for the LANSCE SCL entry.

β_x (cm/mrad)	α_x	β_y (cm/mrad)	α_y
0.556	1.239	0.329	0.337

Table 4.10: MADx simulation results for Twiss parameters at the entrance to the LANSCE SCL.

05QD02 (Amps)	Gradient (kG/cm)	β_x (cm/mrad)	α_x	β_y (cm/mrad)	α_y
16.7	2.0717	0.586	1.32	0.347	0.347
17.5	2.1674	0.554	1.33	0.318	0.373
24	2.7904	0.473	1.68	0.214	0.633
27	2.9590	0.480	1.88	0.201	0.749

To verify that the calculated values gave a periodic solution, the Twiss parameters found for the 16.7-Amp magnet setting were placed at the entry to Module 5 and transported through two modules with a constant quadrupole ramp utilizing the TRACE 2D code. The TRACE 2D code is the code used for establishing the production tune at LANSCE. The observed beam envelopes are shown in Figure 4.25.

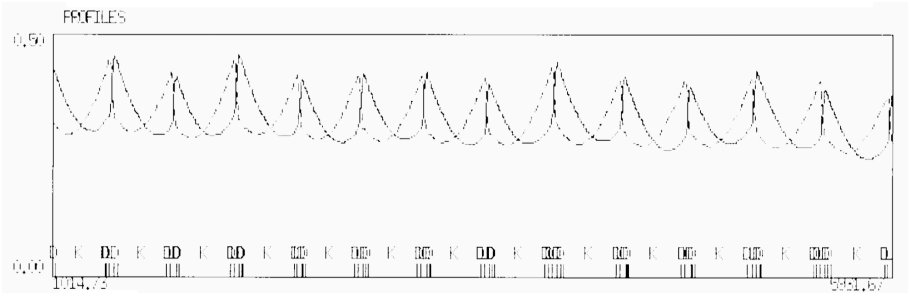

Figure 4.25: TRACE 2D Module 5-7 match results with the MADx calculated Twiss parameters for G=2.0717(kG/cm) and constant ramp.

Now that we have verified the matching parameters at the entrance to the SCL we need to find

the matching parameters at the entrance to Module 13 in the SCL section. Module 13 is where the accelerating structure changes from a four tank module to that of two tanks (see fig.1.9) . The quadrupole lattice is still FDO but the distance between quadrupoles is larger (see Figure 4.26). The matched beam parameters are shown in table 4.11. The calculated Twiss parameters were placed into the TRACE 2D code at the entrance and propagated forward with the quadrupoles set at their designed values of 25 Amps. The observed beam envelope for modules 13-23 and module 13 until the end of the SCL at module 48 are shown in fig. 4.27.

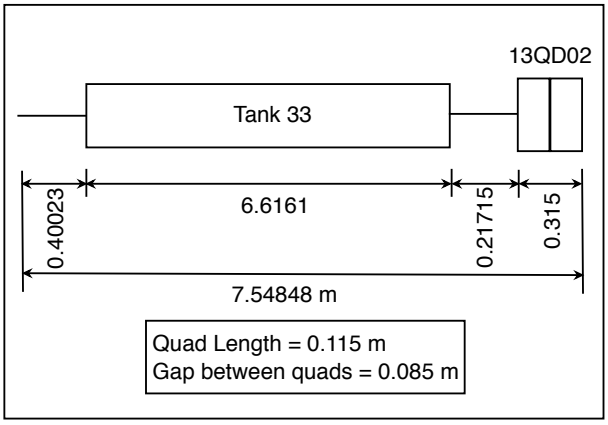

Figure 4.26: SCL Module 13 matching simulation set-up.

Table 4.11: MADx calculated matched beam parameters at the entrance of Module 13.

13QD02 (Amps)	Gradient (kG/cm)	β_x (cm/mrad)	α_x	β_y (cm/mrad)	α_y
25	2.7921	1.1064	1.7488	0.6369	0.943

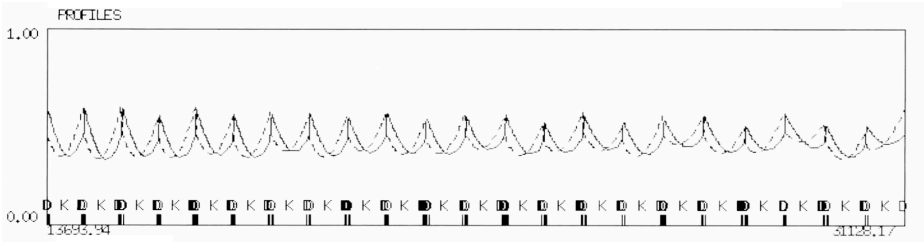

(a) Module 13-23 envelope

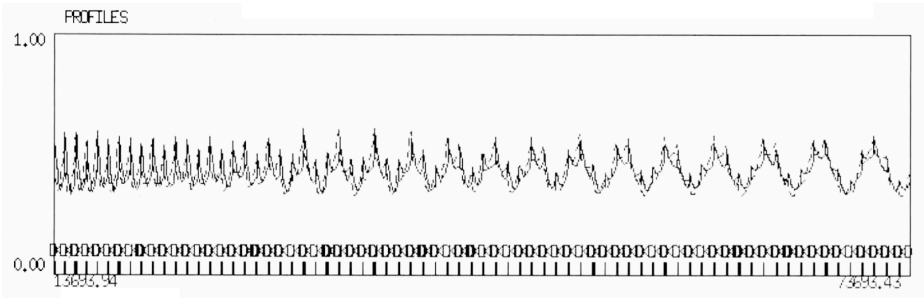

(b) Module 13-48 envelope

Figure 4.27: TRACE 2D simulation results from module 13 until module 48 with MADx calculated Twiss parameters at the entrance of module 13.

As can be seen from fig. 4.27b, the beam envelopes become mismatched at module 23. The matched Twiss parameters therefore have to be determines for the entry into module 23. Figure 4.28 shows the simulation geometrical set-up, table 4.12 shows the results, and fig. 4.29 shows the TRACE 2D results for beam envelopes with the simulated Twiss parameters.

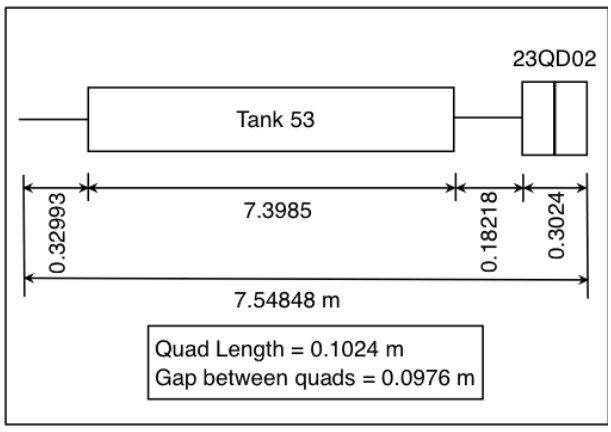

Figure 4.28: SCL Module 23 matching simulation set-up.

Table 4.12: MADx calculated matched beam parameters at the entrance of module 23.

23QD02 (Amps)	Gradient (kG/cm)	β_x (cm/mrad)	α_x	β_y (cm/mrad)	α_y
25	3.0018	1.2114	1.1161	0.817	0.5527

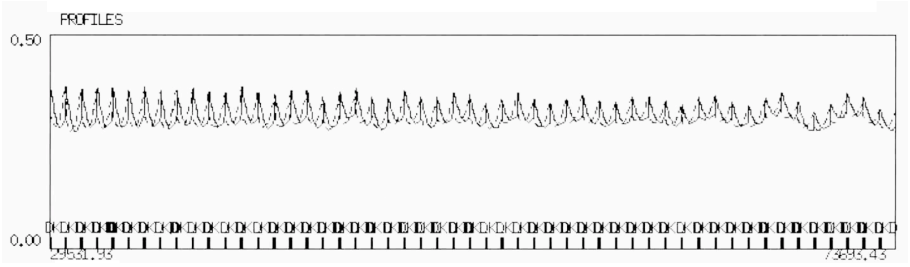

Figure 4.29: TRACE 2D simulation results from module 23 until module 48 with MADx calculated Twiss parameters at the entrance of module 23.

Now that we have all the matching parameters for the different sections of the SCL we can find a complete matched magnet solution. The Twiss parameters simulated for entry into the SCL at Module 5 were close to the historical parameters. The decision was made to use the historical parameters at module 5 in order to study the historical matched solution against other derived solutions. One issue in deriving new matched solutions is that the quadrupoles are not all individually controllable. The majority of the quadrupoles are controlled in pairs by one power supply. The one exception is 12QD03 and 12QD04 which can be controlled independently. The solutions derived are for what we could conceivable obtain within this operating condition. The two solutions derived, other than the historical match, were one using the historical magnet settings but performing a matching evolution using the Twiss parameters at the entry of Module 13 and 23 and the second was found by ramping the Twiss beta values linearly from the module 5 to module 13.

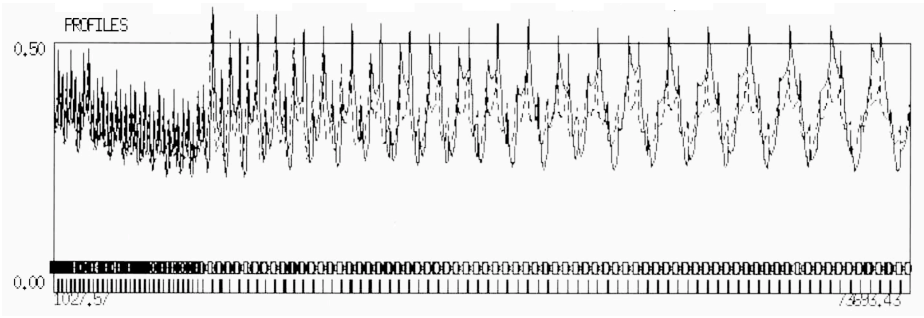

(a) Historical average solution

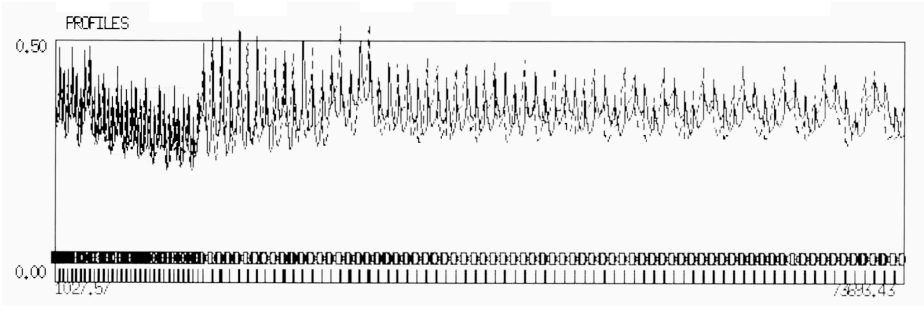

(b) Historical average with matching evolutions performed at module 13 and module 23.

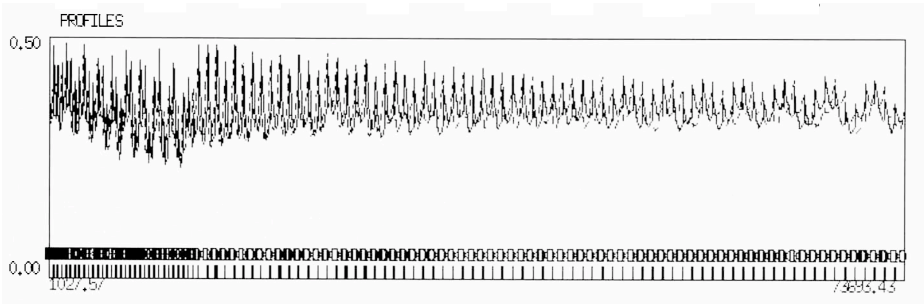

(c) Ramping solution with matching evolutions performed at Module 13 and Module 23.

Figure 4.30: Beam envelopes for different quadrupole solutions in the LANSCE SCL.

Figure 4.30 demonstrates that the historical average solution works for well matched beam from modules 5-12, but becomes mismatched after Module 13 resulting in large oscillations. We were able to reduce that mismatch by performing a matching evolution using the TRACE 2D code at the location of modules 13 and 23. The ramping solution provides slightly less matched beam from modules 5-13 but is better matched into module 13 and module 23 which results in smaller beam envelope oscillations overall.

Table 4.13: LANSCE SCL quadrupole solution currents.

Quadrupole	Historical Values (*Amps*)	Historical Values with Matching (*Amps*)	Ramping Match (*Amps*)
05QD02	16.65	16.65	16.56
05QD03	16.50	16.50	16.23
06QD01	16.94	16.94	16.37
06QD03	16.65	16.65	16.82
07QD01	17.55	17.55	17.85
07QD03	19.04	19.04	18.16
08QD01	19.49	19.49	18.16
08QD03	19.87	19.87	19.99
09QD01	20.98	20.98	19.38
09QD03	21.74	21.74	19.87
10QD01	22.20	22.20	20.29
10QD03	22.35	22.35	20.90
11QD01	24.41	24.41	21.29
11QD03	24.57	24.57	21.86
12QD01	25	25	23.73
12QD03	25	25.33	21.59
12QD04	25	21.74	18.65
13QD01	25	23.35	24.34
14QD01	25	25	25
15QD01	25	25	25
16QD01	25	25	25
17QD01	25	25	25
18QD01	25	25	25
19QD01	25	25	25
20QD01	25	22.24	23.12
21QD01	25	21.21	24.87
22QD01	25	22.05	26.09
23QD01	25	24.03	24.87
(24-48)QD01	25	25	25

The ramping match solution can now be compared to solutions that were obtained by empirically tuning the beam for low losses. The empirical solutions were taken from the magnet data at the end of each year run cycle. The end of the run cycle is the point where the beam losses have been

optimize for production with low losses. Figure 4.31 shows the result of the ramping match compared with the empirical solutions for the 2014-2017 run cycles.

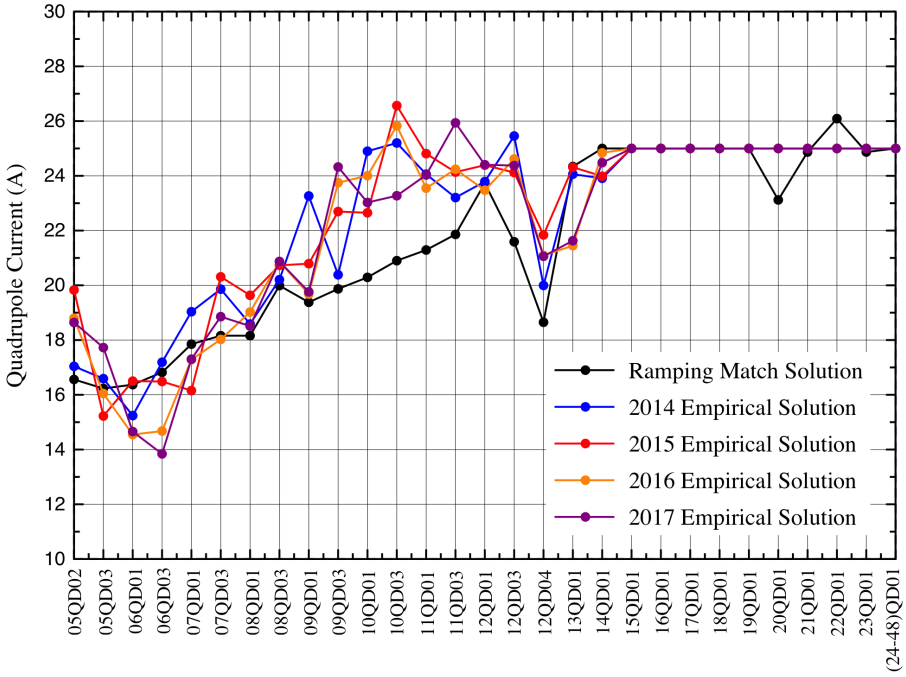

Figure 4.31: Comparison of the empirical SCL quadrupole tune with the theoretical ramping match.

As can be seen from Figure 4.31, the ramping match solution differs from the average empirical solutions from the past run cycles. This could be due to the fact that the TRACE program does not take into account the large quadrupole misalignments that exist in the LANSCE accelerator. Also, the TRACE program treats the beam centroid and does not account for the significant beam tail formation that LANSCE suffers from. Further higher order simulation and theoretical development is required to understand the quadrupole match in the LANSCE accelerator.

4.5 805 MHz Side Coupled Linear Accelerator RF Stability

The 805-MHz side coupled linear accelerator phase and amplitude set-points are established by the Δt turn-on procedure [21]. The name is derived from the relative time-of-flight measurements that are required [21]. Once the correct phase and amplitude set-points are determined for the SCL module, the machine fast protect system ensures that the cavity field error does not exceed $\pm 1\%$ amplitude and $\pm 1^{\circ}$ phase during the beam pulse. There is no automatic machine protection for the slow drift of the phase or amplitude set-point away from its nominal value.

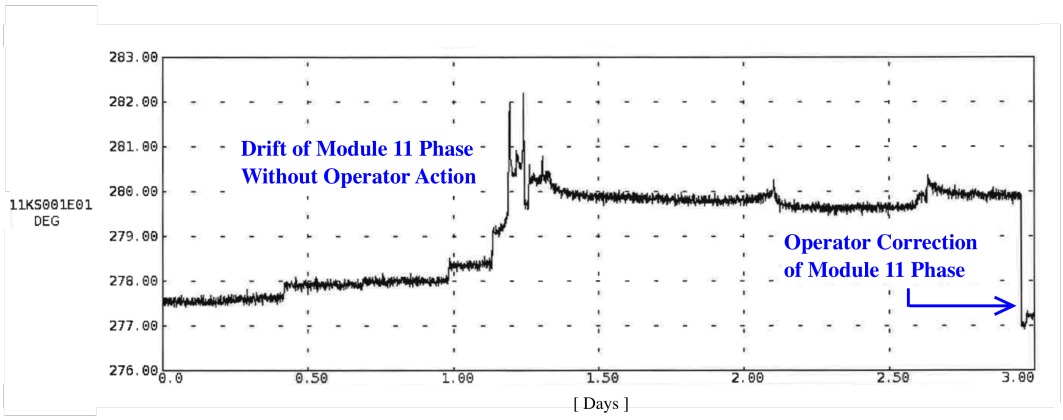

Figure 4.32: Drift of the SCL Module 11 phase set-point over several days of operation.

Correct phase and amplitude settings of the SCL are also important for maintaining the momentum spread of the beam as low as achievable. Low momentum spread beam aids operations personnel in maintaining beam spill in the high energy transport sections of the LANSCE accelerator complex as low as achievable. Figure 4.33 shows an example horizontal wirescan (LDWS03X) measurement performed at the high dispersion point of the Line D North 89°bend. LDWS03X is used as an indication of the relative momentum spread produced at the exit of the LANSCE accelerator.

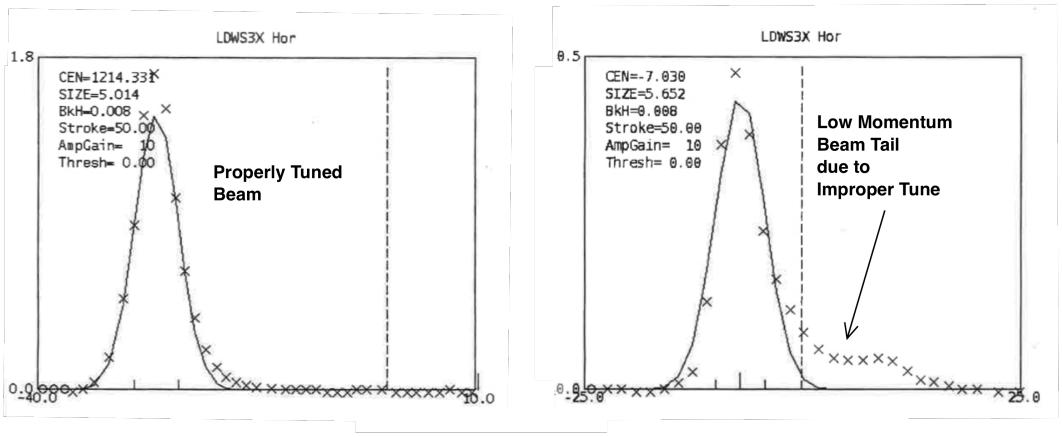

Figure 4.33: Example of effects of momentum spread at the output of the LANSCE accelerator from improper tuning.

Stability of the RF cavity field is critical to minimizing losses during operations. The study performed will show that to achieve low losses, the stability of amplitude and phases should be kept within 0.1% and 0.1°.

The beam with the largest contribution to the total facility spill is the H^- beam delivered to the PSR and Lujan experimental areas. The Lujan beam has a beam power of 80 kW and average

current of 100 μA. It is delivered at a repetition rate of 20 Hz and beam gate length of 625 μs. For the study of the contribution of beam spill due to SCL RF cavity field stability the beam power was reduced to an average current of 5 μA by changing the repetition rate to 4 Hz and the beam gate length to 150 μs.

Measurements were performed by adjusting the phase and amplitude set-points of SCL modules 6-14. The phase and amplitude of each module was adjusted until the beam spill in the switchyard high energy transport beam lines increased significantly. After the increase was observed, the set-point was returned to its previous operational value. This was procedure was performed for each module's phase and amplitude. All results were finally normalized by 1% of variation of RF amplitude, and 1°of variation of RF phase at maximum beam current of 100 μA [23]. Figure 4.34 and 4.35 show the normalized results of variation of beam spill generated by 1% variation in RF amplitude and 1°variation in RF phase at average beam current of 100 μA [23].

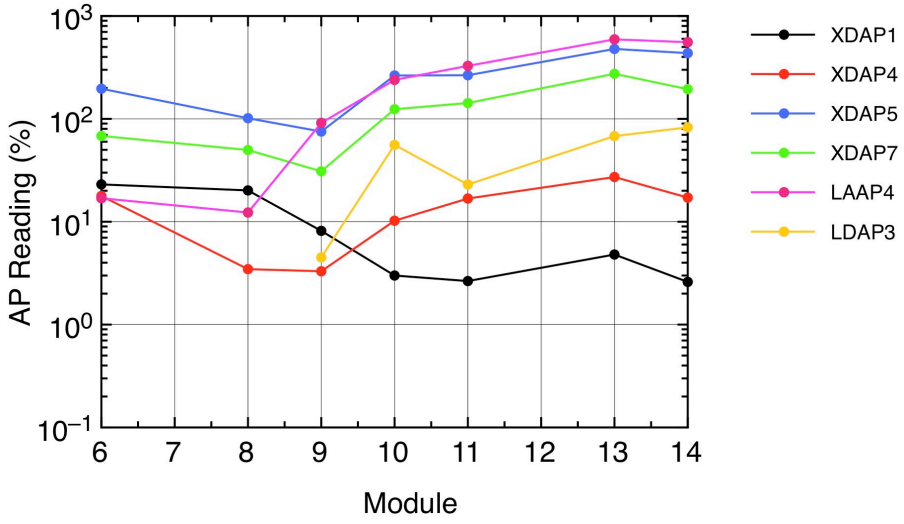

Figure 4.34: Beam spill normalized by 1% variation in RF amplitude [23].

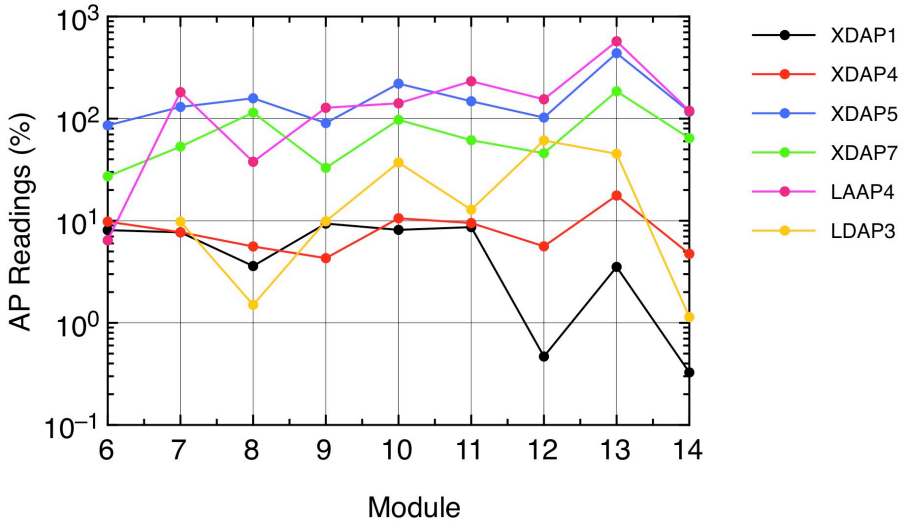

Figure 4.35: Beam spill normalized by 1°variation in RF phase [23].

From this study, the highest extra beam spill was found to be around 500 - 1000 nA. From section 1.3, we know that the LANSCE machine protection system limits beam losses to 100 nA. Therefore, this study confirms that the stability of the RF amplitudes and phases should be kept one order of magnitude smaller than ($\pm 1\%$, $\pm 1°$), or within 0.1% and 0.1°, in order to provide for safe operation of the LANSCE accelerator facility [23].

Chapter 5

Accelerator Magnet Interventions

5.1 Magnet Standardization

Accelerator magnets contain iron or other ferromagnetic material which have a strong dependance on their history. The desired field in an accelerator magnet will be different for a given current depending on its history.

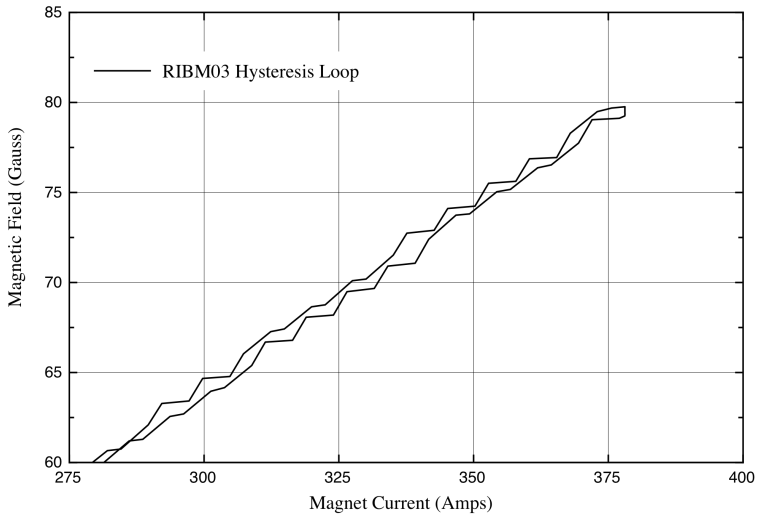

Figure 5.1: Example of magnetic hysteresis loop in Ring Injection bending magnet.

Several situations exist which could lead to a magnet loosing its standardization. The most common experienced at LANSCE are from individual magnet faults in the interlock system or from a loss of the water cooling for either the magnet power supply or the magnet itself. The loss of a water

cooling system can require several hours to recover and without an adequate magnet standardization procedure, the tune recovery also can take hours. These studies are part of the effort to develop a magnet standardization procedure that allows for efficient and stable tune recoveries in the event of equipment failure.

A way to achieve one value of the magnetic field for a given magnet current is by cycling the magnet current around a desired set-point as shown in fig. 5.2 [19].

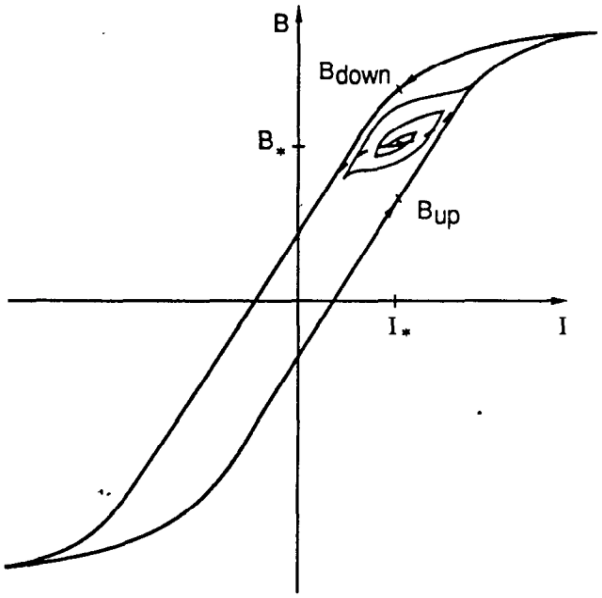

Figure 5.2: Magnet standardization by cycling the magnet current around a set-point [19].

A hysteresis recovery procedure requires a waiting period while the magnetic field stabilizes. Measurement were made to determine adequate hold times. The data shown is from the ring injection bending magnet #3 (RIBM03). The magnet current data was obtained from current read-back channel provided into the EPICS control system. The magnetic field measurements were made by a Hall probe. The data collection was synchronized with the EPICS control system clock. Figure 5.3 shows the results from the measurement. The magnetic field took approximately 20 seconds to stabilize after the magnet reached its current value. Therefore the 30 second wait period proposed in the standardization procedure is adequate.

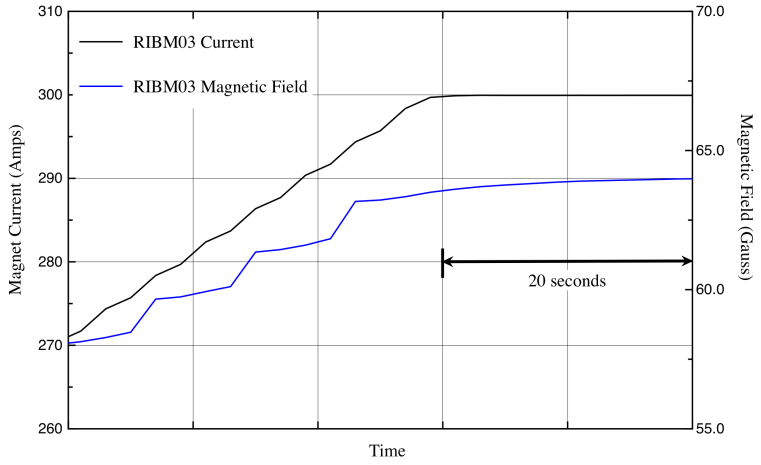

Figure 5.3: RIBM03 magnetic field stabilization measurement.

The procedure for cycling the magnet current around the set-point consisted of raising the magnet current 15% above the set-point and holding for 30 seconds, lowering 15% below set-point and holding for 30 seconds, raising 10% above and holding, lowering 10% below set-point and holding, raising 5% above set-point and holding, and finally lowering to the previous magnet set-point (see fig.5.4).

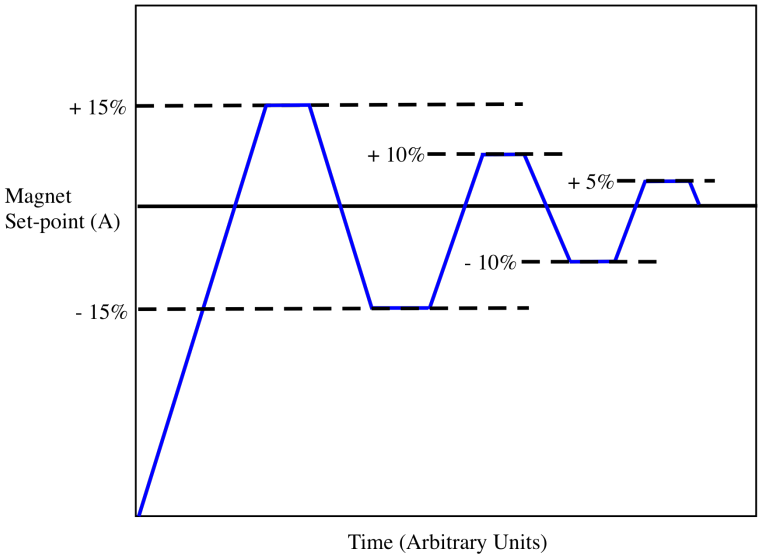

Figure 5.4: Magnet standardization procedure consisting of cycling the magnet current around the set-point.

The Switchyard, PSR and ring injection magnets were used for developing the magnet standardization procedure. To test the hysteresis recovery procedure, the magnet power supply for bending magnets (LDMP02) in the in the LANSCE switchyard was selected. Prior to the magnet being

turned off, beam position monitors and beam spill were recorded. The magnet power supply was turned off for 2 hours to simulate a fault that required significant time to recover. After the magnet power supply was recovered, the magnet was returned to set-point with no hysteresis procedure and beam spill levels verified the field was not the same for the magnet set-point. The hysteresis recovery procedure was then used. The results shown in fig. 5.5 show the BPM measurements performed after the hysteresis procedure compared with the original tune positions. The results show that the cycling around the set-point procedure returned the magnet near to the original field value. Beam losses were elevated after the hysteresis procedure but were not high enough to result in a machine protection fault (see fig. 5.6). Finally, the magnet set-point had to be raised 0.1% from its original set-point to return the tune to its previous values.

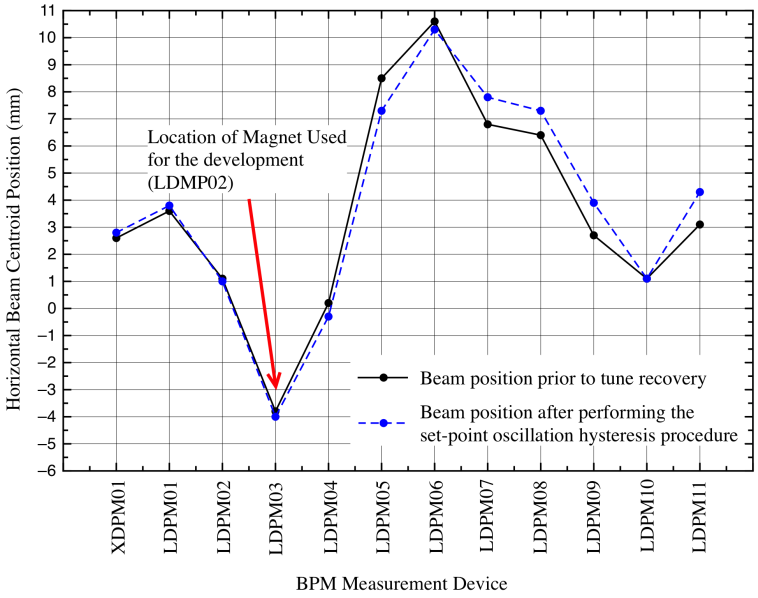

Figure 5.5: BPM measurement results from developing a magnet standardization procedure.

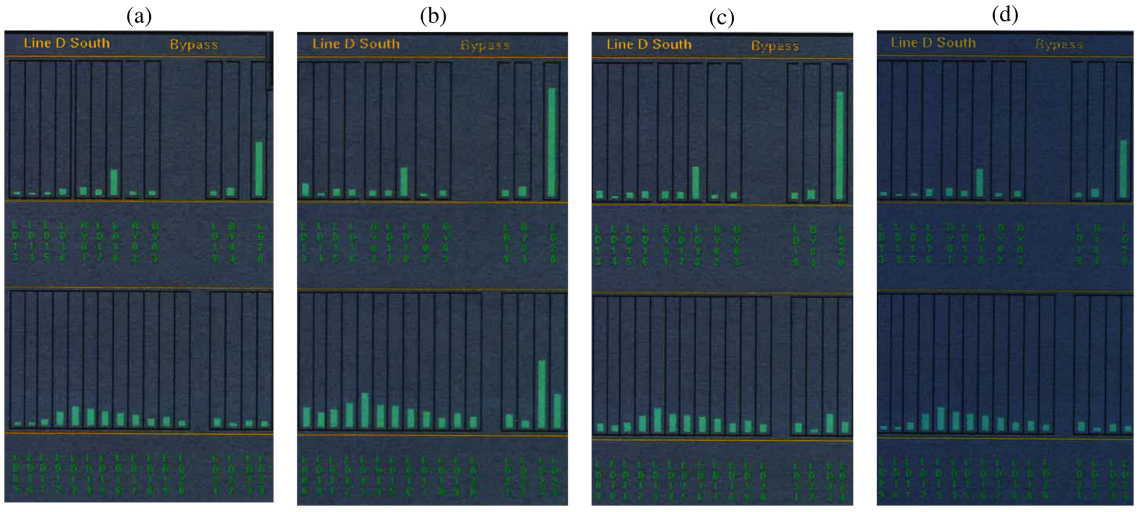

Figure 5.6: Beam losses during the hysteresis recovery of LDMP02. a) Losses prior to turning LDMP02 off. b) Losses with no hysteresis recovery c) Losses after the hysteresis recovery of LDMP02. d) Losses after raising LDMP02 set-point 0.1 %.

The cycling around the set-point standardization procedure was then performed for the PSR and Ring Injection bending magnets and quadrupoles. After each magnet was standardized, the PSR tune was checked. A tune check consisted of measuring changes in percentage beam losses in the ring, deviations from the fractional tune of the ring, and movements in the ring closed orbit. After recovery from the standardization procedure the magnets needed adjustments within the range of 0.1-0.26% of setting to return the tune to its previous values. Recovery of the PSR tune was accomplished with minimal downtime and adjustments when the cycling around the set-point magnet standardization procedure was used.

LANSCE requires manual tuning of the magnets in order to reduce beam losses. This means that one cannot verify that the magnets are on the same location of the hysteresis loop. After development, the cycling around the set-point to end in the middle of the hysteresis loop returns the magnetic fields to values near to the original values before the magnet system fault.

5.2 Residual Magnetic Field Effects on Adjacent WNR Beam Stability

The LANSCE accelerator is a multi-beam facility leading to situations where beam lines are in close proximity to each other. If not properly controlled, residual magnetic fields from one beam line

can have an effect on the adjacent beam line. This study focused on one such location where the combined H^- high energy beam transport line splits into the ring injection line and WNR beam line. At this location, residual magnetic fields from the ring injection bending magnet #1 can effect the adjacent WNR beam.

Figure 5.7: Location of residual magnetic field effect on adjacent beam lines study.

The first task of the study was to determine the impact of the residual fields from the ring injection line on production beam delivery to WNR. During production beam delivery with RIBM01 at its operating set-point, it is assumed that the residual magnetic field, if it was effecting the WNR beam, was being corrected for with steering magnets downstream. To determine if the residual field from RIBM01 was in fact effecting the WNR beam, RIBM01 was turned off while leaving the steering magnets in the WNR beam line constant. Ideally, turning the ring injection bending magnet off should have no impact on the separate WNR beam line. The spill was measured using the activation protection devices in the downstream WNR beam tunnel. The AP detectors provide an input into the LANSCE fast protect system and are designed to turn the beam off if they reach a spill level greater than 80%. Figure 5.8 shows the results from this test. From this we can conclude that the RIBM01 residual magnetic field does effect the beam in the adjacent WNR line and the effects are such that it can stop production beam delivery to the WNR target facility.

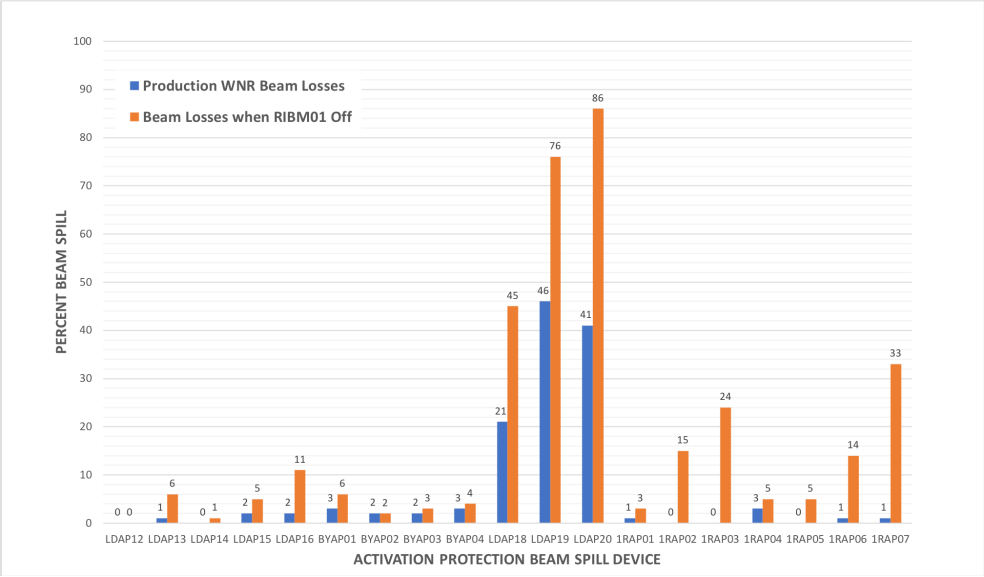

Figure 5.8: Beam spill in the WNR beam line due to RIBM01 residual magnetic field.

During this test, downstream beam position monitors were also recorded. From Figure 5.9 we see that the beam moves in both the horizontal and vertical directions. If we refer back to fig. 5.7, we see that RIBM01 is tilted at an angle of 22°. This skew is because the proton storage ring is at a lower elevation than the beam injection point therefore the injected beam is kicked both horizontally and vertically into a skewed injection line. The skew is eventually removed before injection into the PSR. Therefore, not only does the residual field cause beam spill that stops production beam delivery, but adds error and complexity to accurately modeling and tuning the WNR beam line.

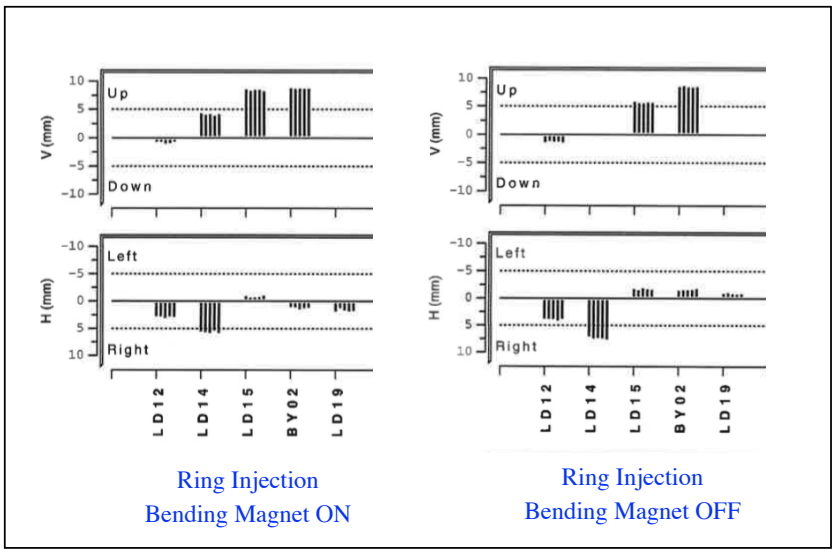

Figure 5.9: BPM data in the WNR beam line due to RIBM01 residual magnetic field.

To further understand the effects of the RIBM01 residual magnetic field on the WNR beam, Hall probe measurements were made in the beam tunnel while RIBM01 was on at its production field values. An attempt was made in the past to minimize the effects of the RIBM01 field on the WNR beam, with the installation of a small section of Mu-metal shielding. The Hall probe measurement points are shown in fig. 5.10 and the values are shown in table 5.1.

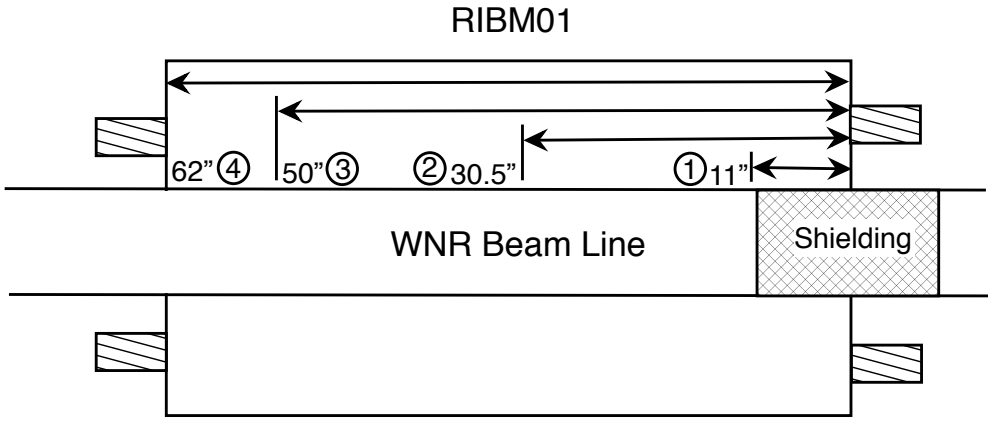

Figure 5.10: Measurement locations for the RIBM01 residual magnetic field

Table 5.1: RIBM01 residual magnetic field Hall probe measurements.

Measurement Location	Field Outside Pipe $(10^{-4}\,T)$	Field Inside Pipe $(10^{-4}\,T)$
1	7.0	8.5
2	6.0	8.8
3	4.8	6.7
4	3.8	5.3

From the Hall probe measurements, we can now calculate the average kick the WNR beam receives. From the Lorentz Force equation, we get:

$$\frac{d^2x}{dt^2} = \frac{q}{m\gamma} v_z B_y \tag{5.1}$$

To find the change in angle, we need to first convert to $\frac{d^2x}{dz^2}$ by multiplying both sides by $\frac{dz^2}{dz^2}$.

$$\frac{d^2x}{dz^2}\left(\frac{dz^2}{dt^2}\right) = \frac{q}{m\gamma} v_z B_y \tag{5.2}$$

We note that $\frac{d^2z}{dt^2} = v_z^2$, therefore:

$$\frac{d^2x}{dz^2} = \frac{q}{m\gamma v_z} B_y = \frac{qB_y}{mc\beta_z\gamma} \tag{5.3}$$

By integrating both sides and making the assumption that $\int B_y = \overline{B_y} L$, where L is the length of the RIBM01 and $\overline{B_y}$ is the average residual magnetic field from the Hall probe measurements, we find:

$$\Delta\frac{dx}{dz} = \frac{q\overline{B_y}L}{mc\beta_z\gamma} \tag{5.4}$$

Using $\overline{B_y} = 6 \cdot 10^{-4}\,T$ and $L = 1.575\,m$, we calculated a $\Delta\frac{dx}{dz} = 0.193\,mrad$. The closest BPM downstream of the RIBM01 residual field is LDPM12 at a $L_{drift} = 7.988\,m$. If we multiply the residual field kick by the drift length, we find a horizontal beam displacement of $1.54\,mm$ that should be measured on the BPM. The actual horizontal displacement measured at LDPM12 was $1\,mm$ (see fig. 5.9).

After characterizing the residual magnetic fields effects and strength, it became important to check if the beam could be corrected with existing downstream steering magnets. One horizontal

steering magnet (LDHM09) and one vertical steering magnet (LDVM09) were manually adjusted from the control room. The steering magnets are identical in construction and are located at approximately the same location in the downstream WNR beam line. After RIBM01 was turned off, both steering magnets required a change of $1.5\,A$ to correct the beam spill due to the residual magnetic field. The beam spill correction results are shown in fig. 5.11.

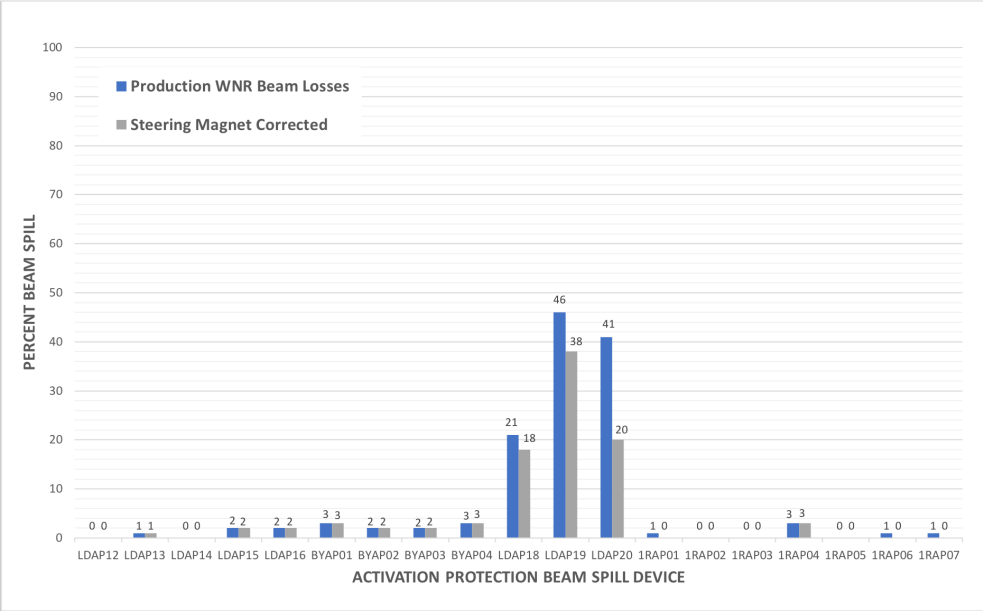

Figure 5.11: Beam losses after correcting for RIBM01 residual magnetic field with LDHM/VM09 steering magnets.

A Hall probe was then used to measure the amount of field change that corresponds to a $1.5\,A$ change in the magnet power supply. This value was found to be $6{\cdot}10^{-3}\,T$. Using the $L_{magnet} = 0.1\,m$ and equation 5.4, the calculated $\Delta\frac{dx}{dz} = 0.123\,mrad$. This value is close to the value calculated from the Hall probe measurements of the residual magnetic field while RIBM01 was at its production magnetic field.

After the empirical study was complete, an effort was made to model the situation and analyze for possible solutions. CST EM Studio was used to evaluate the residual magnetic field effects from RIBM01 on the adjacent WNR beam line [20]. The dimensions used for the model were measured manually and confirmed by the Magnet Team responsible for RIBM01. The CST model set-up is shown in Figure 5.12. The dark blue area on the WNR beam pipe is the location of the existing Mu-metal shielding. The dipole symmetry plane is tilted 22°with respect to the floor and the WNR beam pipe is located in this symmetry plane.

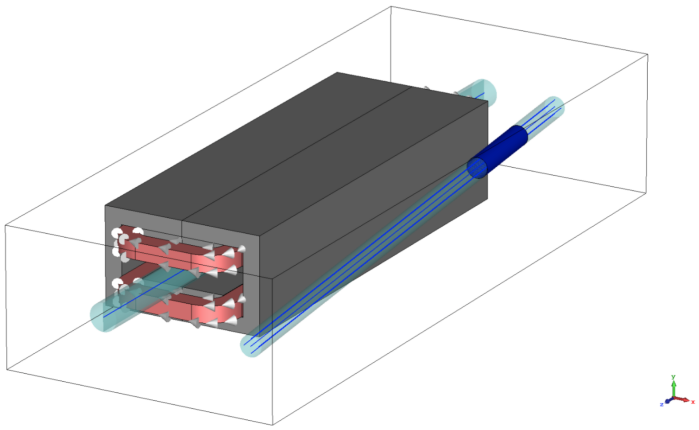

Figure 5.12: CST module of RIBM01 with adjacent WNR beam pipe [20].

The CST tetrahedral magneto-static solver with adaptive mesh iterations was used for field computations [20]. The field of the dipole was measured with a Hall probe on the ring injection line axis as $B_y = -3.8\,kG$. The dipole current in the model was adjusted to match this value. Figure 5.13 shows the calculated magnetic field at the RIBM01 axis after adjusting the model to match the measured values.

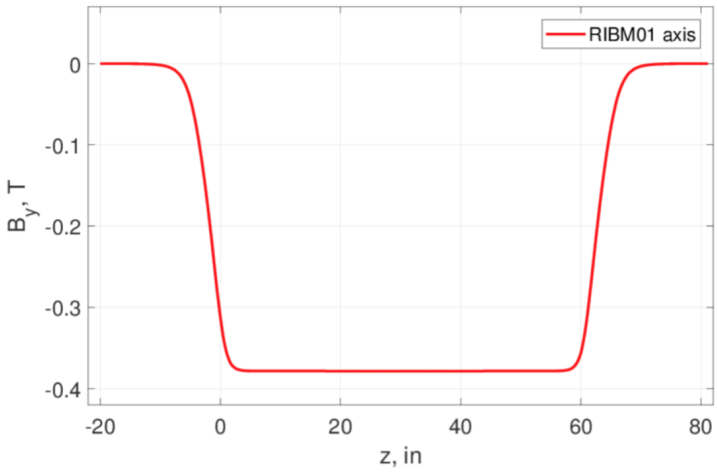

Figure 5.13: RIBM01 magnetic field along the beam line axis [20].

Now that the model is built we can look at the field created at the the adjacent WNR beam line. Figure 5.14 shows the vertical magnetic field produced by RIBM01. From this we see that the field actually cancels out some on either side of the Mu-metal shielding. The Mu-metal shielding is effective at lowering the residual magnetic field to zero in the WNR beam line. Figure 5.15 displays

the magnetic field lines in the area of the Mu-metal shielding.

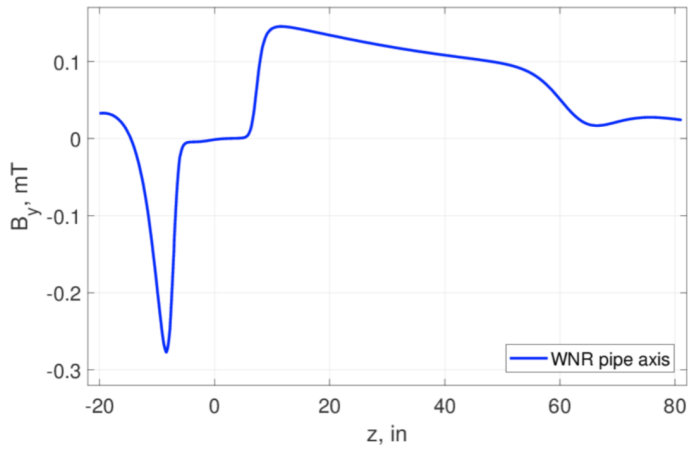

Figure 5.14: RIBM01 residual magnetic field strengths at the WNR beam line axis [20].

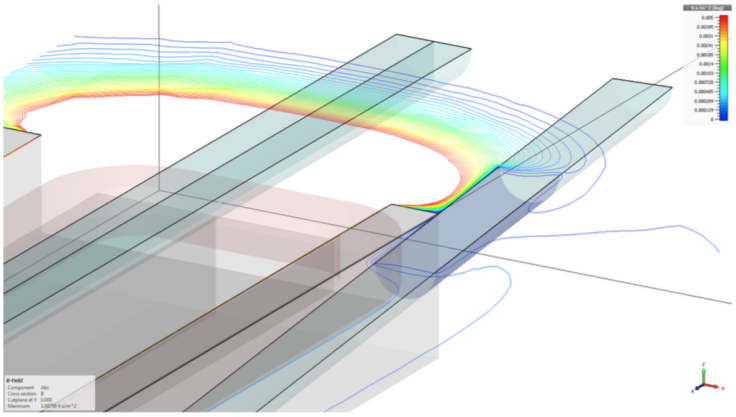

Figure 5.15: Magnetic field lines from the RIBM01 residual magnetic field near the WNR beam line Mu-metal shielding [20].

The fields predicted in the model are less than those measured empirically. But the model was useful in answering the question about the effectiveness of the Mu-metal shielding. We then used the model to extend the Mu-metal shielding along the entire WNR beam line adjacent to RIBM01 and extended it $\pm 19 inches$ on either side of RIBM01 (see fig. 5.16).

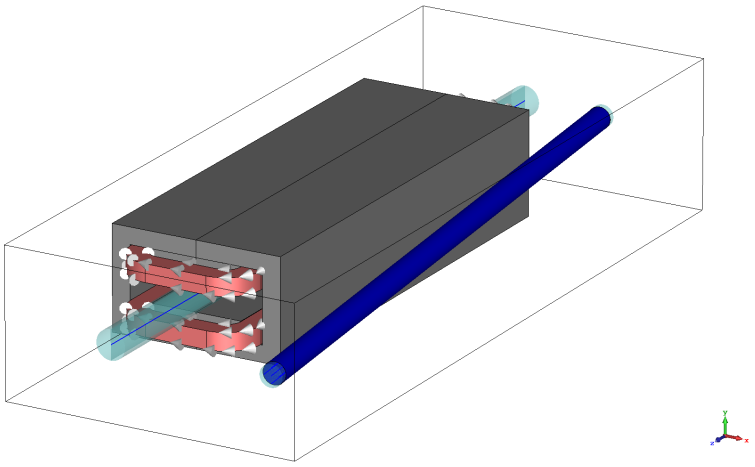

Figure 5.16: RIBM01 CST model with Mu metal shielding extended on the WNR beam line [20].

Extended the Mu-metal shielding was effective at removing all RIBM01 magnetic field effects from the adjacent WNR beam line (see fig. 5.17).

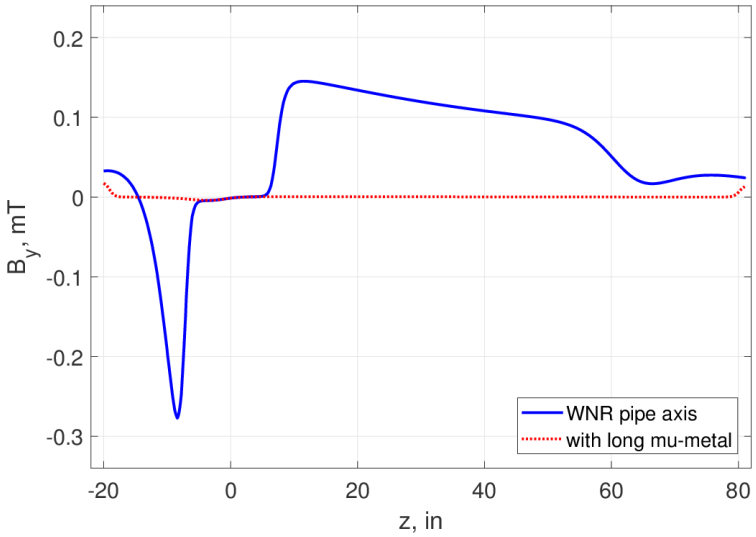

Figure 5.17: Magnetic field strength along the WNR beam line axis with full Mu-metal shiedling [20].

During the maintenance outage in the spring of 2018, the magnet team installed Mu-metal on the WNR beam line as shown in the simulation fig. 5.16. The installation of the Mu-metal shielding is shown in fig. 5.18.

Figure 5.18: Mu-metal shielding installed along the entire length of WNR beam pipe effecting by the RIBM01 residual magnetic field.

To verify the effectiveness of the Mu-metal shielding installation, the initial study was repeated with RIBM01 being cycled on and off while the downstream beam position monitors and beam losses were recorded. The BPM results are shown in Figure 5.19 and show that the Mu-metal installed on the WNR beam line successfully shields the beam from the residual magnetic field generated by RIBM01.

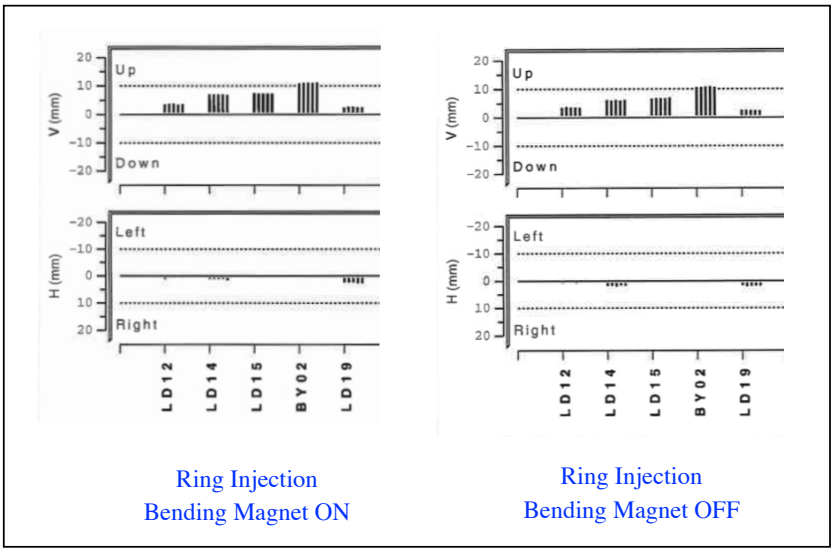

Figure 5.19: BPM results after Mu-metal shielding installed on the WNR beam line.

From this study we were able to successfully characterize the effects from the RIBM01 residual

magnetic field on the adjacent WNR beam line. The empirical study concluded that the effect was strong enough to stop production beam delivery to WNR. It also demonstrated that the effect could be corrected for with downstream steering magnets. The CST simulations provided insight into the nature of the magnetic field on WNR beam line and the effectiveness of Mu-metal shielding. We were able to utilize these results to install more Mu-metal shielding that now removes the effect of the residual magnetic field generated by RIBM01 on the adjacent WNR beam.

Conclusions

The LANSCE accelerator facility is a tool used to explore the scientific missions assigned to Los Alamos National Laboratory. However, it is also an aging facility that has gone through several upgrades to extend its life. In order for the facility to meets its production and scientific goals a thorough understanding of mechanisms that contribute to accelerator stability and tune recovery need to be explored.

An effort was made to regain past knowledge on the basic beam dynamics of the accelerator. This will help the accelerator operations physicists verify models in development and set-up the machine as designed. A proper tune also requires knowledge of the entire facility not only including the original physics design, but how all the components come together to achieve that design.

The accelerator stability studies successfully identified and produced solutions for major problems that contribute to extended tune recovery periods and beam stability. The DTL RF stability problem was empirically documented and investigated back to issues with the stability of the reference source. A study was performed that showed the error levels of RF fields in the side coupled linear accelerator that could be tolerated during production. A magnet standardization procedure was developed and tested. The study on residual magnetic field effects on adjacent beam lines lead to the installation of mu-metal shielding mitigating any unwanted beam deflections. The high voltage droop associated with the H^- injector was identified as unacceptable and a solution was found. Particle-in-cell simulations of the LANSCE SCL were performed. Mechanisms for emittance growth were explored. Transverse emittance growth is mostly effected by space charge. Variations in the RF field is a cause of momentum spread growth. Ongoing work will be done to verify and improve on the solutions as the accelerator facility moves into the future stages of its production life. The goal is to not only meet our reliability numbers but to safely deliver stable beam to the users when it is requested and these studies are but a part of the larger effort towards these goals.

Bibliography

[1] Batygin, Y.K. et al. *Beam Performance in H^- Injector of LANSCE* IPAC Proceedings. 2011. San Sebastian, Spain.

[2] McCrady, R. et al. *Mitigation of Magnet Hysteresis Effects at LANSCE* LINAC Proceedings. 2006. Knoxville, Tennessee.

[3] J. Lyles, et al. *A New 201.25 MHz High Power RF System for the LANSCE DTL.* EPAC Proceedings. 2002. Paris, France.

[4] J. Lyles, et al. *Design, Fabrication, Installation and Operation of New 201 MHz RF System at LANSCE.* LINAC Proceedings. 2016. East Lansing, MI, USA.

[5] Los Alamos National Laboratory, Los Alamos National Security, LLC, and U.S. Department of Energy. (n.d.). Retrieved from http://lansce.lanl.gov/facilities/ipf/index.php

[6] Pieck, Martin. et al. *Recent Enhancements to the Los Alamos Isotope Production Facility* ICALEPCS Proceedings. 2017. Barcelona, Spain.

[7] Saunders, A. *Proton Radiography at Los Alamos.* Seminar at Tennessee Technical University. 2017.

[8] Wangler, Thomas P. *RF Linear Accelerators.* Wiley-VCH. Weinheim. 2008.

[9] Batygin, Yuri K. *Proton and Ion Linear Accelerators.* USPAS Lecture Notes. January 2017.

[10] Macek, Robert, et al. *LANSCE Phase II Upgrade Technical Report.* PSR Technical Note 96-016.

[11] Lawrence, G.P. *The Performance of the Los Alamos Proton Storage Ring.* PAC Conference Proceedings. 1987. Washington, D.C.

[12] Accelerator Operations Manager. *LANSCE Reliability Report.* LANL Internal Document. 2018.

[13] Rybarcyk, L. et al. *H^- Beam Loss and Evidence of Intrabeam Stripping in the LANSCE Linac.* IPAC Proceedings. 2012.

[14] Rybarcyk, L. *High Power Operational Experience with the LANSCE Linac.* HB Proceedings. 2008.

[15] Kapchinskiy, I.M. *Theory of Resonance Linear Accelerators.* Harwood Academic Publishers. New York. 1985.

[16] Takeda, Harunori. *Parmila.* LANL Internal Document. 1998.

[17] Rybarcyk, L. et al. *The Effect of DTL Cavity Field Errors on Beam Spill at LANSCE.* LINAC Proceedings. 2016.

[18] Scheinker, A. *RF Lurch Report.* LANL Internal Document. 2018.

[19] Decker, Franz-Josef. *The Physical Way of Standardizing Magnets* SLAC-PUB-5483. May 1991.

[20] Kurennoy, Sergey. *Stray Magnetic Fields of RIBM Dipole in WNR Beam Pipe.* Technical Note. AOT-AE: 18-002. February 2018.

[21] Crandall, R.A. et al. *The ΔT Turn-On Procedure* Los Alamos Scientific Laboratory Internal Document.

[22] Batygin, Y. K. *Particle-in-cell code BEAMPATH for beam dynamics simulations in linear accelerators and beamlines.* Nuclear Instruments and Methods in Physics Research. 2005.

[23] Batygin, Y. K. *Effect of 805-MHz Linac RF Stability on Beam Losses in LANSCE High-Energy Beamlines.* IPAC Proceedings. 2018. Vancouver, B.C. Canada.

[24] Pillai, Chandra. *Drift Tube Linac Tuning Guide.* LANL Internal Document.

[25] Pillai, Chandra. Personal conversation.

Appendix A

Parametric Resonance in the DTL

In a linac, the transverse phase advances is typically much larger than the longitudinal phase advance. Because of this, the first region of parametric resonance is avoided. The potentially dangerous region is the second parametric resonance bandwidth where $n = 2$. The higher orders than $n = 2$ are usually not important. Parametric resonance occurs when:

$$\mu_s = \frac{n}{2}\mu_{0\ell} \quad \text{n=1,2,3} \tag{A.1}$$

The parameters for the first two regions of instability a_n and b_n can be determined by the following equations:

$$\begin{aligned} a_1 =& 1 + q - \frac{q^2}{8} - \frac{q^3}{64} \\ b_1 =& 1 - q - \frac{q^2}{8} + q^3 64 \\ a_2 =& 4 + \frac{5q^2}{12} - \frac{763q^4}{13824} \\ a_2 =& 4 - \frac{5q^2}{12} + \frac{763q^4}{13824} \end{aligned} \tag{A.2}$$

Where:

$$q \approx \frac{\varphi_s}{\tan\varphi_s} \tag{A.3}$$

Figure A.1 shows the results for the parametric resonance analysis of the LANSCE DTL and fig. A.2 shows a close view of the areas where tank 1 crosses into the instability region. Further simulations must be done to understand what the effects of these calculations have on the beam stability through the DTL.

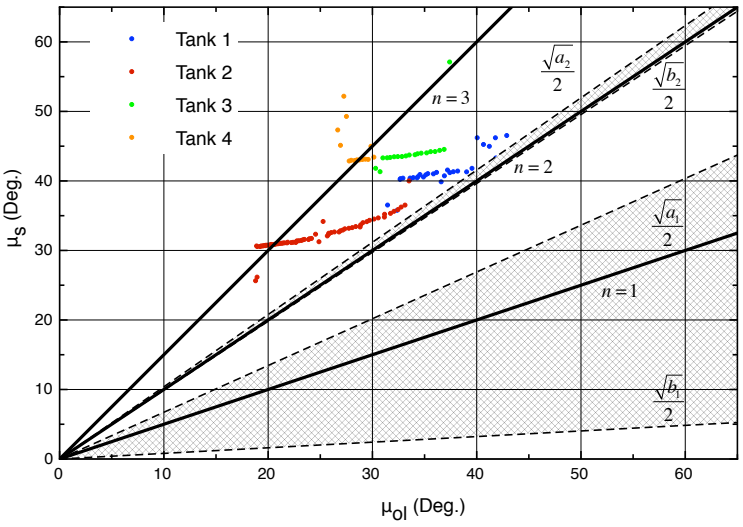

Figure A.1: Parametric resonance in an RF field study of the LANSCE DTL.

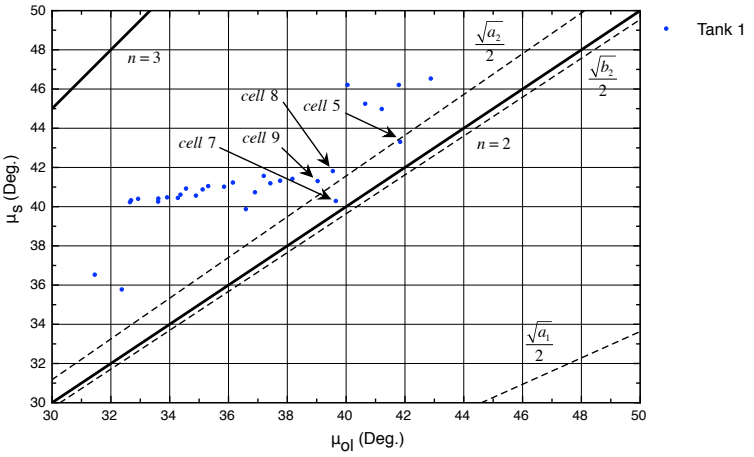

Figure A.2: Parametric resonance study of the LANSCE DTL tank 1 near the second region of instability.